WINDOWS INTO SAUROPSID AND SYNAPSID EVOLUTION
Essays in honor of Prof. Louis L. Jacobs, pp. 1–65, 2023

NOVEL ANATOMY AND PALEOBIOLOGICAL INSIGHTS ON *CISTECEPHALUS MICRORHINUS* (SYNAPSIDA: DICYNODONTIA)

Z. MACUNGO[1,2,*], R. ARAÚJO[1,3,*], C. BROWNING[4], R. M. H. SMITH[2,4], R. DAVID[5], K. D. ANGIELCZYK[6], A. MASSINGUE[1], S. FERREIRA-CARDOSO[7], and D. J. P. KORTJE[4]

[1]Museu Nacional de Geologia, Maputo, Mozambique
[2]Evolutionary Studies Institute, University of the Witwatersrand, Johannesburg, South Africa
[3]Instituto de Plasmas e Fusão Nuclear, Universidade de Lisboa, Portugal
[4]Iziko South African Museum, Cape Town, South Africa
[5]Natural History Museum, London, United Kingdom
[6]Negaunee Integrative Research Center, Field Museum of Natural History, 1400 South DuSable Lake Shore Drive, Chicago, Illinois, 60605, USA
[7]Institut des Sciences de l'Evolution de Montpellier (ISEM), CNRS, IRD, EPHE, Université de Montpellier, Montpellier, France

ABSTRACT Although *Cistecephalus microrhinus* is a well-researched dicynodont taxon, our study using bone-by-bone manual segmentation of micro-computed tomography scans has unveiled a plethora of new insights into its paleobiology, anatomy, and variation. We detail the neuroanatomy of two South African *Cistecephalus* specimens, SAM-PK-K6814 and SAM-PK-011474, and shed light on the internal three-dimensional structures of the *Cistecephalus* skull. Our findings also clarify previously ambiguous bone contacts in serial-sections and highlight external morphological features previously obscured by the species' small size, taphonomic deformation, overpreparation, or matrix obstructions. We specifically studied the evolution of the postfrontal in emydopoids and propose that it may have resulted from co-ossification with the postorbital, rather than element deletion. Our examination of the inner ear anatomy allowed the calculation of the thermo-motility index, which suggests that cistecephalids, including *Kawingasaurus*, and other dicynodonts, were likely ectotherms — a stance that challenges a recent hypothesis based on the angle between semicircular canals. Both *Cistecephalus* and its close relative *Kawingasaurus*, were found to have typical angles between these canals. This result emphasizes the significance of considering the utricular section of the canal when measuring angles and making paleobiological inferences. Additional evidence supporting the ectothermic nature of cistecephalids, despite their atypical brain morphology, comes from propagation phase-contrast synchrotron tomography scans. These scans did not reveal mammal-like complex turbinals; instead, these structures appear to be the result of sediment infilling. When the physiological inferences are contextualized within the Permian Karoo paleoclimate, it is plausible that *Cistecephalus* underwent brumation in winter, aligning with its fossorial traits.

KEYWORDS Dicynodonts, Cistecephalids, Thermo-motility index, Ectothermy, Semicircular canals, Postfrontal

INTRODUCTION

Cistecephalus, recognized as one of the most disparate dicynodont species, was promptly designated a new genus in Owen's (1876) catalogue. Remarkably, some features highlighted by Richard Owen remain pertinent today, such as the "singular proportions of the skull, which is broader than long" and the "box-like shape of the skull" (Owen, 1876, p. 63), the latter giving the genus its name (*Kiste* from the Ancient Greek for box). The genus' unique anatomy and abundant specimens led Broom (1906) to acknowledge its biostratigraphic value, which persists through to the present as the *Cistecephalus* Assemblage Zone (Kitching 1970, Smith and Keyser 1995, Smith 2020). Various paleobiological hypotheses have been proposed for *Cistecephalus*, including (semi)aquatic (Broom 1948, Brink 1950), scansorial (McRae 1999), and arboreal (Keyser 1973) lifestyles. However, due to its robust forelimbs, which are analogous to those of moles, its bone microstructure, and compact skull anatomy, *Cistecephalus* is currently viewed as an obligate fossorial dicynodont, embodying some of the most extreme fossorial adaptations among dicynodonts (Keyser 1973, Cluver 1978, Lungmus and Angielczyk 2021, Kammerer 2021, Macungo et al. 2022).

*Corresponding and co-first author

The prevalence of *Cistecephalus* is so notable that Keyser (1965, 1973) utilized serial-sectioning on one specimen to reveal more detailed anatomy than external morphology alone could provide. Since then, Keyser's (1973) work has served as a reference for the anatomy of cistecephalids and has been utilized in a comparative framework for other emydopoids and Permian dicynodonts in general (e.g., Kammerer et al. 2011, Angielczyk et al. 2019, 2023). Given its significance, *Cistecephalus* warrants further reanalysis utilizing contemporary technology, specifically micro-computed tomography. This technology enables a detailed examination of osteohistology and internal cranial anatomy, as well as meticulous bone contact analysis in multiple anatomical planes, and generates three-dimensional endocasts of volumes once occupied by soft tissue.

In this study, we conduct bone-by-bone segmentation of a *Cistecephalus* specimen (SAM-PK-6814), supplemented, when necessary, with segmentation of an additional specimen (SAM-PK-K011474). This work complements Keyser's (1973) description and provide new details on the neuroanatomy, as well as inner ear and maxillary antrum morphology in this species. We also reanalyze some characters in a phylogenetic context, propose an evolutionary hypothesis for loss of the postfrontals in emydopoids, calculate the thermomotility index for *Cistecephalus* — indicating it was most likely an ectotherm, refute previous suggestions that the angle between semicircular canals was unusual, confirm the absence of turbinals, and contextualize cistecephalids and other dicynodonts within their Permian Karoo paleoclimate. The latter work suggests that these animals likely engaged in brumation during the colder season, consistent with their fossorial adaptations.

MATERIALS AND METHODS

Specimen SAM-PK-K6814 is a well-preserved, complete *Cistecephalus microrhinus* skull with articulated lower jaw and partial postcranial skeleton (Fig. 1), and SAM-PK-K011474 is a well-preserved *Cistecephalus microrhinus* specimen with complete, but disarticulated lower jaw and partial postcranial skeleton (Fig. 2). Both specimens were mechanically prepared in the Karoo Palaeontology laboratory of Iziko South African Museum using a compressed-air driven air-scribe and consolidated using Paraloid B72 diluted with acetone. SAM-PK-K6814 was prepared by Annelise Crean Georgina Skinner and SAM-PK-K011474 was prepared by Jay Van den Berg. Based on their size (Nasterlack et al. 2012), the specimens represent adults, with basal skull lengths of 53,3 and 47 mm, and maximum skull widths of 61,6 and 62,4 mm for SAM-PK-K6814 and SAM-PK-K011474, respectively.

Institutional Abbreviations

BP, Evolutionary Studies Institute (Johannesburg, South Africa); BSP, Bayerische Staatssammlung für Paläontologie und Historische Geologie, Munich, Germany; GPIT, Institut und Museum für Geologie und Paläontologie der Eberhard-Karls-Universität Tübingen, Germany; NHCC, National Heritage Conservation Commission (Lusaka, Zambia); PK, Karoo Palaeontology Collection; PPM, Projecto PaleoMoz, Museu Nacional de Geologia (Maputo, Mozambique); SAM; Iziko South African Museum, Cape Town, South Africa.

Geological setting

Specimen SAM-PK-K6814 was found by Annelise Crean and collected by R.M.H. Smith in 1995 on the farm Good Luck (Matjesfontein 412) in the Namakwa District, Northern Cape Province, South Africa (Fig. 3). It was found in the late Permian (~259.9-254.17 Ma; Rubidge et al. 2013) Steenkampsvlakte Member of the Teekloof Formation (Beaufort Group, Adelaide Subgroup, Karoo Supergroup) in strata assigned to the uppermost *Cistecephalus* Assemblage Zone (Smith 2020, Fig. 3). Specimen SAM-PK-K011474 was collected by A.T. Bremner in 1978 from the farm Doornplaats (Rust 126) near Graaff-Reinet in the Eastern Cape Province, South Africa. It was also found in the upper *Cistecephalus* Assemblage Zone strata.

Micro-computed tomography scanning

The *Cistecephalus microrhinus* specimens were imaged at Stellenbosch University's Central Analytical Facility (CAF) using a walk-in microfocus X-ray μCT scanner (General ElectricPhoenixV|Tome|XL24 with NF180). A 0.2 mm Cu filter was used in both scans to reduce the potential effect of beam hardening artifacts. For SAM-PK-K6814, a total of 3500 slices were generated in coronal planes with the following metrics: resolution = 2024 pixels, isotropic voxel size = 0.04500001 mm, magnification ratio = 4.44444352, voltage = 180 kV, current = 120 μA. A total of 3500 slices were generated in coronal planes for SAM-PK-K011474, with the

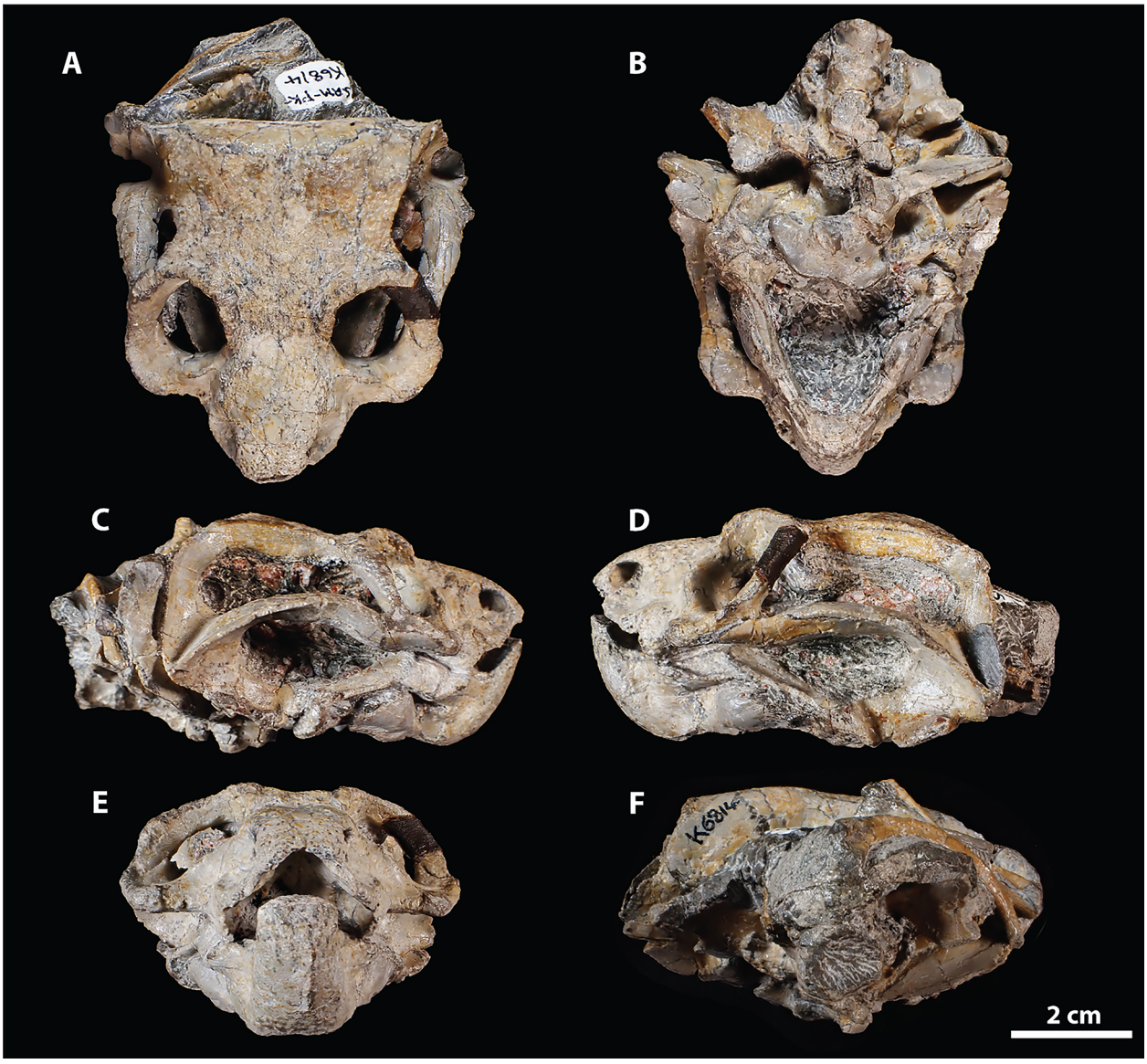

FIGURE 1. Photographs of *Cistecephalus microrhinus* specimen SAM-PK-K6814 in A, dorsal; B, ventral; C, right lateral; D, left lateral; E, anterior; and F, posterior view.

following metrics: resolution = 2024 pixels, isotropic voxel size = 0.03000001 mm, magnification ratio = 6.66666528, voltage = 245 kV, current = 120 lA. The acquired projection images were reconstructed using system-supplied Datos reconstruction software. Three-dimensional reconstructions and visualization of CT data of specimens were generated using Avizo 9.0 (FEI VSG, Hillsboro, OR, USA). Morphological structures (i.e., cranial bones and the endocasts of the brain, maxillary canal, and inner ear) were manually segmented using the same software to produce three-dimensional renderings that were measured virtually following a similar protocol used in Macungo et al. (2022). Raw CT data sets are stored at the Iziko South African Museum and are available upon request to the authors by email: cbrowning@iziko.org.za. Bone-by-bone segmentation of SAM-PK-K6814 and SAM-PK-K011474 resulted in full three-dimensional renderings of the entire skull (Fig. 4), including the skull roof (Fig. 5), palate (Fig. 6), internal cranial bones (Fig. 7), braincase (Fig. 8), stapes (Fig. 9), and various endocasts, such as the brain, endosseous labyrinth and maxillary antrum (Fig. 10). All 3D renderings are available in Morphobank project # 4895, and can be opened and visualized with 3D

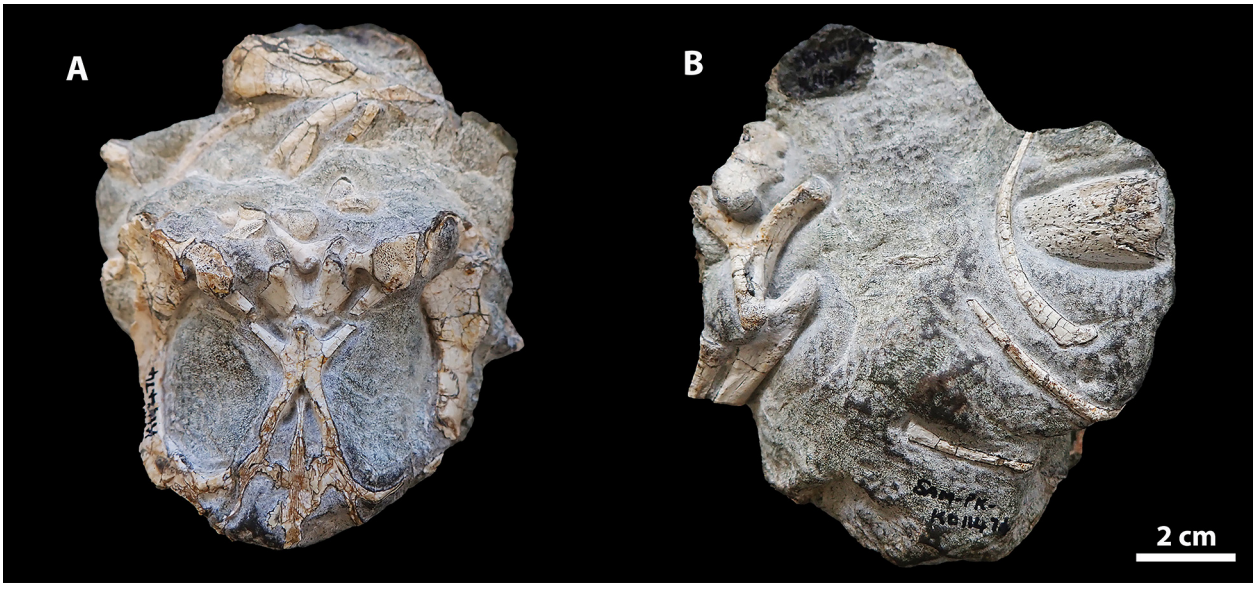

FIGURE 2. Photographs of *Cistecephalus microrhinus* specimen SAM-PK-K011474 in A, ventral and B, dorsal view.

object software (e.g., Meshlab).

In addition to the *Cistecephalus* specimens, µCT data for several other dicynodont specimens was used in our examination of postfrontal morphology. These specimens were all scanned a the University of Chicago's PaleoCT facility using a GE v|tome|x s 240 µCT scanner. The *Compsodon helmoedi* specimen NHCC LB14 was scanned with a 0.5mm Sn filter, using a voltage of 200 kV and 210 µA current, resulting in an isotropic voxel size of 64.90 µm. The *Kembawacela kitchingi* specimen NHCC LB18 was scanned with a 0.5 mm Sn filter, using a voltage of 120 kV and 380 µA current, resulting in an isotropic voxel size of 46.63 µm. NHCC LB37, a specimen representing a new lystrosaurid taxon, with a 0.5 mm Sn filter, using a voltage of 200 kV and 200 µA current, resulting in an isotropic voxel size of 107 µm. The *Dicynodontoides* sp. NHCC LB117 skull NHCC LB117 was scanned with a 0.5 mm Sn filter, using a voltage of 210 kV and 210 µA current, resulting in an isotropic voxel size of 68.87 µm. The *Abajudon kaayai* specimen NHCC LB314 was scanned with a 0.5 mm Sn filter, using a voltage of 120 kV and 660 µA current, resulting in an isotropic voxel size of 80.11 µm. The *Oudenodon bainii* specimen NHCC LB631 was scanned with a 0.5 mm Sn filter, using a voltage of 220 kV and 260 µA current, resulting in an isotropic voxel size of 87.04 µm.

Kawingasaurus fossilis GPIT-PV-117032 (formerly GPIT/RE/9272) was scanned at the propagation phase-contrast synchrotron tomography facilities at the European Synchrotron Radiation Facility in Grenoble, France, at the BM05 beamline. Voxel resolution was 27 µm. The *Kawingasaurus* was analyzed using propagation phase contrast X-ray synchrotron micro-Computed Tomography (PPC-SRµCT). The beam setup included: (1) a white beam filtered through 10 mm of aluminium and 3 mm of copper, (2) a resulting total detected energy of 107 keV. The imaging details were as follows: (1) an indirect detector with a 750 µm thick LuAG scintillator was used, (2) the detector had 2x magnification using Hasselblad lenses, (3) it utilized a sCMOS PCO.edge 5.5 camera (from PCO, Kelheim, Germany) with a USB3 camera link, (4) the detector was positioned 2250 mm beyond the sample in the X-ray path for PPC-SRµCT, (5) the X-ray beam dimensions on the sample were 29.72 mm horizontally and 4.25 mm vertically. Due to the sample's size exceeding the field of view: (1) he rotation axis of the sample stage was first shifted by about 8 mm, following the half acquisition protocol by Carlson et al (2011). This produced tomograms measuring 45.63 mm in diameter (or 3441 pixels). Next, 20 acquisitions were made, moving the specimen 2.12 mm vertically each time. This created a 50% overlap between consecutive datasets. Each acquisition had 8000 projections, each lasting 40 milliseconds. This high number of projections compensated for camera noise since frame averaging was not available then. For the white field image (beam image without a sample), 101 images were taken and a median image was produced. For the darkfield (capturing camera noise without

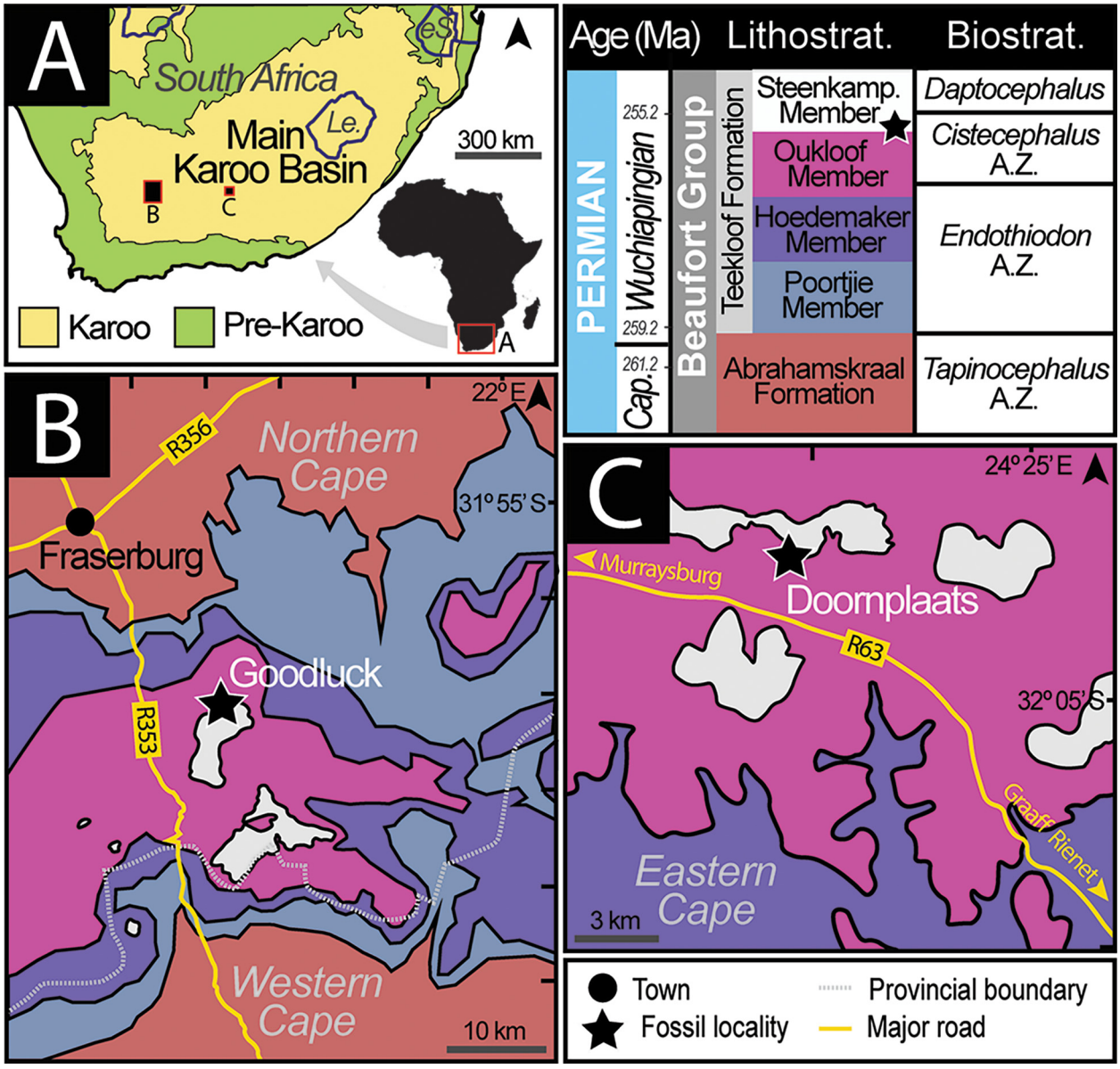

FIGURE 3. (A) Simplified stratigraphic context and geological map indicating the location of the study areas (insets B and C) within the Main Karoo Basin, South Africa. Detailed geological maps of the (B) Good Luck and (C) Doornplaats fossil localities indicating where *Cistecephalus microrhinus* specimens were collected. Specimen SAM-PK-K6814 was collected from Good Luck and specimen SAM-PK-K011474 was collected from Doornplaats. Both specimens were found in the lower Steenkampsvlakte Member (upper *Cistecephalus* Assemblage Zone). Abbreviations: Cap. = Capitanian, Steenkamp. = Steenkampsvlakte Member, A.Z. = Assemblage Zone. Lithostrat. = Lithostratigraphy. Biostrat. = Biostratigraphy.

the beam), 40 images were averaged. The tomographic reconstruction process involved: (1) using PyHST2 (as per Mirone et al. 2014) with the single distance phase retrieval method (Paganin et al. 2002), (2) setting the δ/β parameter to balance noise reduction and avoid blurring, (3) other steps included adjusting the bit depth from 32 to 16 bits based on the 3D histogram by PyHST2, applying ring correction as per Lyckegaard et al 2011, and cropping the volume, (4) lastly, a 2x2x2 binning was done to enhance the signal-to-noise ratio and minimize data size for segmentation.

Phylogenetic analysis

The phylogenetic analysis reflects the new additions and revisions of the most recent analyses of dicynodonts, namely

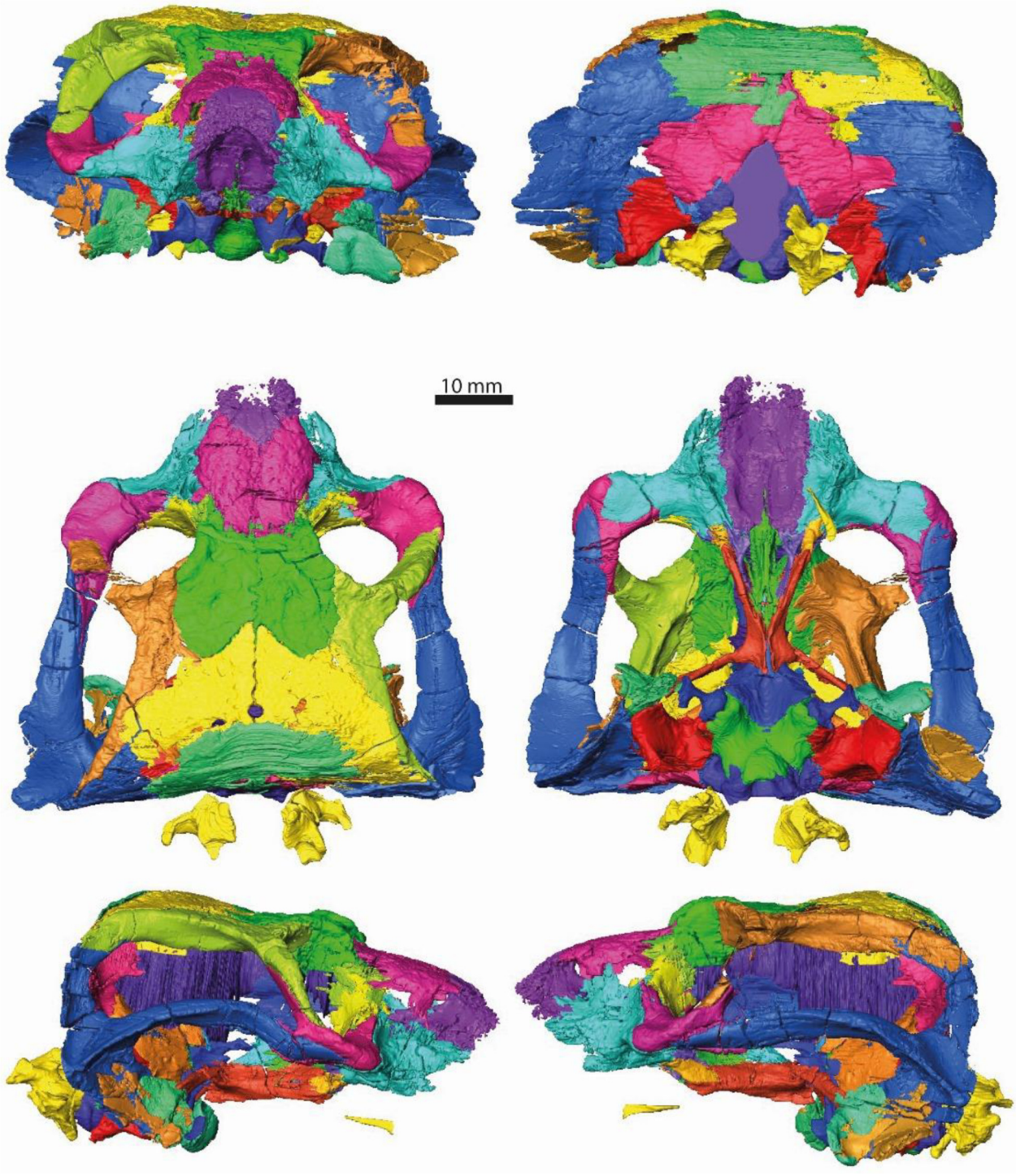

FIGURE 4. Segmentated three-dimensional rendering of *Cistecephalus microrhinus* (SAM-PK-K6814) in anterior, posterior, dorsal, ventral, right lateral and left lateral views.

from Kammerer & Ordoñez (2021), Angielczyk et al. (2021), Liu (2021, 2022), Araújo et al. (2022b), Macungo et al. (2022), Shi & Liu (2023), Szczygielski & Sulej (2023), Escobar et al. (2023) and Angielczyk et al. (2023). We also added some Mozambican specimens that will be described in detail elsewhere (PPM2019-38Z, PPM2019-106R, PPM2019-46R and PPM2019-96R).

We added 10 new discrete characters to the 190 characters

proposed by Macungo et al. (2022), resulting in 200 discrete characters and 23 continuous characters. Some of these characters cannot be visualized without micro-computed tomography (e.g., characters 193-195), but they represent an initial effort to incorporate observed interspecific variation.

Character 191: The mean position of the transverse axis of the frontal margin is far from the ascending process of the premaxilla (0), closely approaches the ascending process of the premaxilla (1). This character can be assessed, in most cases, by observing the external surface of the skull. Basal non-bidentalian and kannemeyeriform taxa have a small ascending process of the premaxilla (e.g., *Niassodon*), whereas - for instance - the geikiid *Bulbasaurus* has a long ascending process of the premaxilla such that it nearly touches the frontal (Kammerer & Smith 2017).

Character 192: Postorbital: The articular surface with the jugal located along the posterior aspect of the descending process of the postorbital (0), the articular surface with the jugal located medially (1). This character can be assessed by observing the postorbital bar. It may represent the structural importance of the jugal dorsal process in lieu of the postorbital descending process, and vice-versa. Whereas in some taxa the descending process of the postorbital completely obscures the postorbital (e.g., *Diictodon*, see Supplementary Information), in others the dorsal process of the jugal is well-exposed posteriorly (e.g., *Cistecephalus*).

Character 193: Mesethmoid: Horizontal plate present (0), horizontal plate absent (1). Macungo et al. (2022) observed a horizontal plate on the anterodorsal section of the orbito-sphenoid in their segmented specimens *Myosaurus* and *Pristerodon*, whereas this plate is absent in *Diictodon* (Supplementary Information). For more information, on the homologies of the ethmoid, or 'anterior plate' (Cluver 1971), please refer to the description of the ethmoid below.

Character 194: Mesethmoid: Dorsal fossa present (0), dorsal fossa absent (1). The horizontal plate dorsal fossa is clearly defined in *Myosaurus*, whereas *Pristerodon* does not have any depression on its dorsal surface (Macungo et al. 2022).

Character 195: Presphenoid: The vertical process is far from reaching the palate (0), the vertical process reaches the palate or nearly touches it (1). This condition can be assessed only by micro-computed tomography or serially-ground sections. The character states differentiate between morphologies observed in *Myosaurus* and *Diictodon* (Supplementary Information, Macungo et al. 2022), in which the orbitosphenoid does not contact any palatal element (Macungo et al. 2022), and *Cistecephalus* where the orbitosphenoid nearly contacts the parasphenoid.

Character 196: Quadrate: lateral condyle shorter medio-laterally or similar in size relative to the medial condyle (0), lateral condyle significantly longer than the medial condyle (1). This condition can be assessed by observing the ventral surface of the skull. Whereas *Eosimops* has the lateral condyle significantly longer than the medial condyle (Angielczyk et al. 2013), in *Cistecephaloides* the medial condyle is similar in size to the lateral condyle (Cluver 1974a).

Character 197: Quadrate: posterior quadrate crest absent (0), posterior quadrate crest present (1). This condition can be contrasted between *Niassodon*, which has a simple dorsal process of the quadrate, and *Ciscecephalus,* which has a small, anterolaterally-directed, infolding posteriorly (this paper).

Character 198: Quadrate: quadrate notch visible (i.e., at the intersection of the lateral condyle and dorsal plate there is a noticeable notch posteriorly) (1), quadrate notch not visible (0). Whereas in basal anomodonts (e.g., *Patranomodon*) this region of the quadrate is straight, in *Cistecephalus* (this paper), for instance, it has an obvious recess.

Character 199: Quadratojugal twisted (1), quadratojugal does not twist (0). These character states can be contrasted between *Niassodon*, in which the quadratojugal twists counterclockwise (Castanhinha et al. 2013), and *Cistecephalus* where the quadratojugal is flat (this paper).

Character 200: Supraoccipital transverse crest present (1), supraoccipital transverse crest absent (0). The supraoccipital transverse crest can be seen on the anterior surface of the bone, thus, it can only be seen using micro-computed tomography scanning. This condition can be contrasted between *Niassodon* and *Cistecephalus* (Castanhinha et al. 2013, this paper), which do not possess this crest, and *K. yajuwayeyi*, which has a horizontal crest arising from the median section of the supraoccipital (Araújo et al. 2022b).

We also revised some character codings to reflect our observations. Discrete Character 22 was rescored as polymorphic for *Dicynodontoides* because some specimens possess a tusk and others possess only an edentulous caniniform process (e.g., NHCC LB117). Similarly, *Prosictodon* (e.g. BP/1/7190), *Diictodon*, *Brachyprosopus*, *Pristerodon*, *Abajudon*, *Tropidostoma*, *Australobarbarus*, *Odontocyclops*, and *Emydops* spp. were coded as polymorphic for Discrete Character 22

because tusked and tuskless adult specimens are known for these taxa. The original codings for *Compsodon* and *Colobodectes* were kept because ontogeny should be avoided as a confounding factor when assessing the presence of tusks in the data matrix (Angielczyk and Rubidge 2009, Angielczyk et al. 2023). The situation for *Robertia* and *Digalodon* is uncertain because some specimens are badly preserved in this region (Angielczyk & Rubidge 2013, Kammerer et al. 2015), and the original codings was left unchanged.

We changed Discrete Character 51 to '?' for *Rastodon* because the holotype appears to be dorsoventrally compressed, making the original orientation of the postorbital uncertain. The morphology of the temporal portion of the postorbital in *Dicynodontoides* is difficult to accommodate in the current character-state scheme as the postorbital is sub-vertical medially and then curves towards a more horizontal position laterally, with some variation in the extent of this shape changing between specimens. Therefore, we coded this character as polymorphic (i.e., [0,1]) to accommodate this variability, but we note that is will be important to clearly tackle this issue at the specimen level in the future as part of on-going revisions to the species taxonomy of *Dicynodontoides*.

For Discrete Character 66, *Rastodon* was rescored as '?' as the area for the sutural contact of the maxilla and squamosal is badly damaged.

We changed Discrete Character 72 for *Rastodon* from '1' to '0' because the mid-ventral plate of vomers does not show a notable expanded area posterior to the junction with premaxilla, just as in *Dicynodontoides*. We also changed Discrete Character 73 for *Rastodon* from '1' to '0', because the mid-ventral plate of vomers is relatively wide in ventral view, as in *Dicynodontoides*. However, for Discrete Character 72 and 73 a segmentation of this part of the skull in *Rastodon* would help to be more confident in these character state codings.

We changed Discrete Character 91 for *Rastodon* to '?' as the surface of the anterior region of the pterygoids is poorly preserved.

We changed Discrete Character 112 for *Rastodon* and *Dicynodontoides* to '1' (i.e., presence of a lateral edge of paroccipital process drawn into sharp posteriorly-directed process that is distinctly offset from the surface of the occipital plate), because despite being damaged in some specimens (e.g., UNI-PAMPA 317, NHCC LB117) the base of the 'tympanic process' is still visible.

We recoded Discrete Character 114 for *Rastodon* as '?' because it is not clear whether the mandibular fenestra is present from available data (Boos et al. 2016, Simão-Oliveira et al. 2020).

We also changed Discrete Character 128 for *Rastodon* to '1' because a groove is visible on the anterodorsal edge of the lateral dentary shelf.

We recoded Discrete Character 183 for *Rastodon* to '?' because the posterior surface of the supraoccipital is poorly preserved.

We were able to observe in some micro-computed data and specimens of *Dicynodontoides* that the pilaantotica is narrow and rod-like, which led us to code Discrete Character 185 as '1'. Also, we recoded Discrete Character 190 for *Dicynodontoides* as '1' because the full extent of the exoccipital is visible in NHCC LB117, showing that it reached approximately half the height of the foramen magnum.

We analyzed two versions of the data matrix, one with *Kunpania* and another excluding it, using TNT 1.5 June 2021 version with no taxon limit for Windows (Goloboff & Catalano, 2016). Discrete-state characters 58, 61, 79, 140, 150, 151 and 166 were ordered. The analysis used the 'new technology search' algorithms to find the most parsimonious trees. Once the shortest tree length was hit 20 independent times using 'xmult' plus ten cycles of tree-drifting cycles (Goloboff, 1999), the strict consensus tree was drawn by collapsing the tree using tree bisection-reconnection and respective node supports. Synapomorphies common to the one most parsimonious tree are shown in the Supplementary Information. Absolute and relative Bremer supports were calculated for the nodes using tree bisection-reconnection by swapping the trees (Bremer, 1994; Goloboff & Farris, 2001). We also used resampling to assess node support, which was calculated by doing 10000 replications of symmetric resampling (Goloboff et al., 2003), analyzing each data set with a single random addition sequence plus tree bisection-reconnection and then collapsing the resulting tree (Goloboff & Farris, 2001). The phylogenetic matrix with named discrete characters which can be opened in Mesquite and the matrix with continuous and discrete characters which can be run in TNT, as well as the complete retrieved phylogenetic tree, with Bremer support and resampling values can be downloaded from the Morphobank project # 4895.

Node calibration and last appearance datum for *Cistecephalus*

Node calibration is necessary to attribute the appropriate branch lengths (in Ma) to the trees to calculate the thermo-motility indices for *Cistecephalus*. The oldest well-documented cistecephalid is *Cistecephalus microrhinus*, which first appears in the upper *Tropidostoma-Gorgonops* Subzone of the *Endothiodon* Assemblage Zone of the Karoo Basin (Day & Smith 2020). This assemblage zone is bracketed by radiometric dates of 259.26 Mya and 256.25 Mya (Day et al. 2015). The undescribed Mid-Zambezi Basin cistecephalid (see Angielczyk et al. 2019) may be older, but its age is very poorly constrained (Barbolini et al. 2016). Therefore, we calibrate this node at 259.26 Mya. The last appearance datum for *Cistecephalus microrhinus* is at the top of the *Cistecephalus* Assemblage Zone, which has been radiometrically dated at 255.2 Mya (Smith 2020 and references therein).

RESULTS

Thermo-motility indices

Following the methods described in Araújo et al. (2022a), we computed the thermo-motility index of *Cistecephalus* and obtained a value of 1.18, corresponding to an endothermy probability of 47%, which is interpreted as ambiguous. Additionally, we combined our *Cistecephalus* data with previously published data for *Kembawacela* (48%) and *Kawingasaurus* (27%, Araújo et al. 2022), and obtained endothermy probabilities of 23 and 40%, respectively, at the node (*Cistecephalus*, *Kawingasaurus*, *Kembawacela*) and for the average of these species. These values are lower than 47%, which has been shown to be the threshold below which ectothermy can be interpreted with more than 95% accuracy in extant species (Araújo et al. 2022a). Taken together, these values are lower than 47%, which has been shown to be the threshold below which ectothermy can be interpreted with more than 95% accuracy in extant species (Araújo et al. 2022a).

Semicircular canal orientations

Applying equations of semicircular duct biomechanics to landmark sets placed along each semicircular canal torus, including the utricular parts, we were able to measure functional semicircular canal plane orientations in *Kawingasaurus* and *Cistecephalus* (Fig. 11). Results are presented in Table 1, along with 95% confidence intervals for angular values observed across 57 amniote species.

Cistecephalus falls within 95% C.I. for extant amniote variation for all angles. *Kawingasaurus* falls within 95% C.I. for extant amniote variation for most angles, except for the angles between the anterior and posterior semicircular canals, and the angles the anterior and posterior semicircular canals form with the horizontal plane.

COMPARATIVE ANATOMICAL DESCRIPTION

Keyser's (1965, 1973) provided the most recent detailed description of *Cistecephalus*, including information from serially-sectioned specimens. However, these works focused on the contacts between bones and omitted various details, particularly when full three-dimensional views of the bone or anatomical structure were required. Our comparative description utilizes μCT data to update and expand on Keyer's important contribution.

Skull

Premaxilla

Despite being at a right angle in relation to the antero-posterior axis of the skull at its base (Keyser 1965), the ascending process of the premaxilla (appmx, median spine of the premaxilla; "median spine" of Keyser 1965) deflects abruptly posteriorly at its midheight. The ascending process

TABLE 1. Semicircular canal angular relationships

	A^P	A^L	L^P	A^S	A^C	A^H	P^S	P^C	P^H	L^S	L^C	L^H
Kawingasaurus	82	76	82	40	51	81	42	52	76	82	90	8
Cistecephalus	87	85	82	41	49	89	47	44	83	88	90	4
Amniote 95C.I.	86:105	73:94	82:99	32:50	41:58	85:106	34:54	37:56	80:97	78:99	90	-3:11

Angles in degrees. A: Anterior semicircular canal, P: Posterior semicircular canal, L: Lateral semicircular canal, S: Sagittal plane, C: Coronal plane, H: Horizontal plane, ^: Angle between.

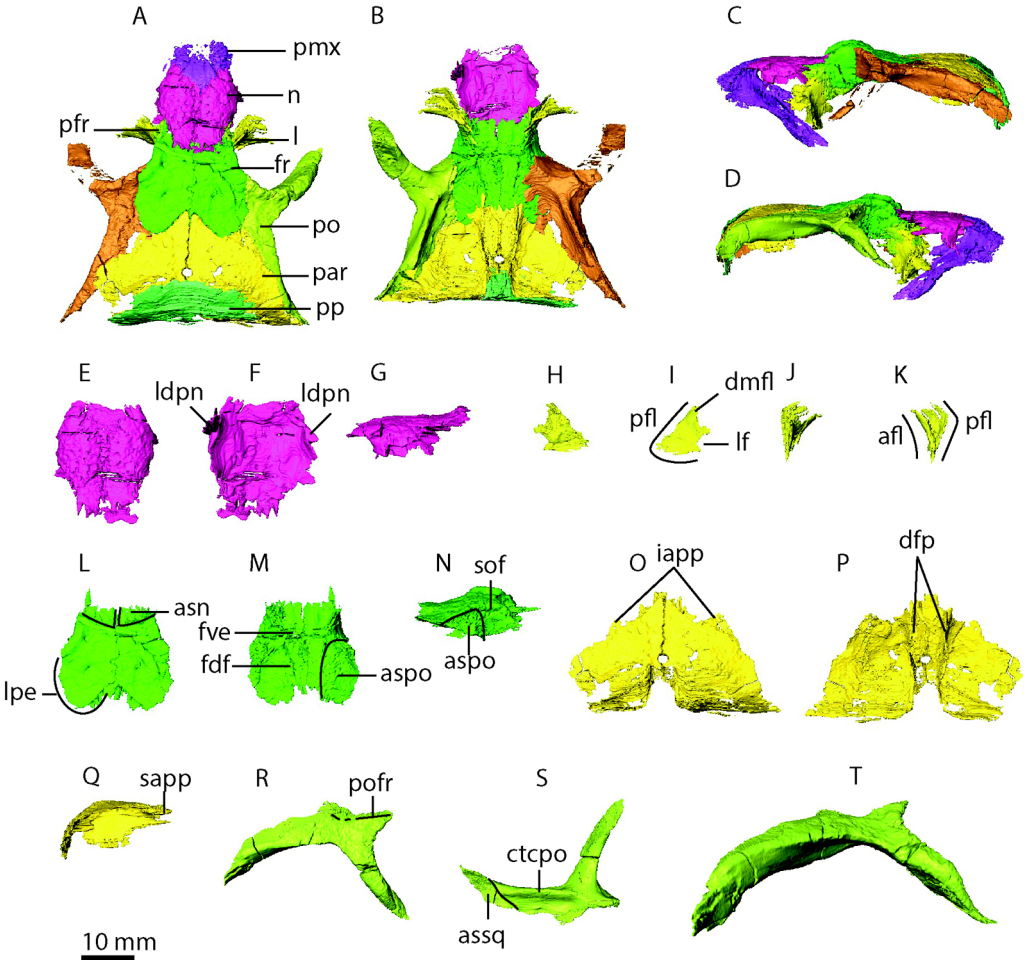

FIGURE 5. Skull roof of SAM-PK-K6814. A, dorsal view of the skull roof; B, ventral view of the skull roof; C, left lateral view of the skull roof; D, right lateral view of the skull roof; E, dorsal view of the nasals; F, ventral view of the nasals; G, lateral view of the nasals; H, anterior view of the left lacrimal; I, posterior view of the left lacrimal; J, dorsal view of the right lacrimal; K, ventral view of the right lacrimal. Abbreviations: afl, anterior flange of the lacrimal; asn, articular surface of the nasal; aspo, articular surface of the postorbitals; assq, articular surface of the squamosal; ctcpo, crest of the temporal component of the postorbital; dfp, descending flanges of the parietal; dmfl, dorsomedial foramen of the lacrimal; fdf, frontal descending flanges; fr, frontals; fve, frontal ventral excavations; iapp, internal anterior process of the parietal; n, nasals; l, lacrimal; ldpn, lateral descending process of the nasal; lf, lacrimal foramen; lpe, lobate posterior extension of the frontal; par, parietal; pfr, prefrontals; pfl, posterior flange of the lacrimal; pmx, premaxilla; po, postorbital; pofr, postorbital-frontal ridge; pp, postparietal; sapp, short anterior projections of the parietal; sof, supraorbital ridges of the frontal.

does not extend far between the nasals, and it tapers to a broad subtriangular apex, unlike the significantly more acute apex of *Compsodon* (Angielczyk and Kammerer 2017). The ascending process of the premaxilla clasps the anteriormost process of the nasal, becoming exposed dorsally. There are various nutritive foramina on the dorsal surface of the ascending process that continue posteriorly as furrows that are likely associated with the presence of a keratinous rhamphotheca (Benoit et al. 2018). As in *K. kitchingi* (Angielczyk et al. 2019), the frontal does not closely approach the ascending process of the premaxilla and there is no longitudinal ridge on its anterior surface.

The palatal surface of the maxilla is cupped and the premaxilla forms most of the secondary palate. As *Kembawacela kitchingi* (Angielczyk et al. 2019), the cutting edge of the premaxilla is badly preserved in SAM-PK-K6814, but it seems to have formed a thin, narrow anterior edge (not a downturned rim as most dicynodonts). In *K. kitchingi* the cutting edge of the premaxilla is arched in anterior view, with the palatal rim having a more anteriorly-facing edge, in

Cistecephalus it has a more ventrally-facing cutting edge. Although Keyser (1965, 1973) describes a squared ridge on the ventral surface of the premaxillaries, it is rather a bifurcating ridge that smoothly opens into a slit from about midlength in SAM-PK-K6814 (pmrpmx, posterior median ridge of the premaxilla, Fig. 6). However, it is important to note that this morphology for *Cistecephalus* is unusual, and could be either the true morphology or the result of slight taphonomic displacement. The two small foramina on the anterior part of the palate observed in SAM-PK-K150 by Keyser (1965, 1973) were not observed in SAM-PK-K011474 and SAM-PK-K6814. Unfortunately, it is not possible to confirm this character by physical inspection of the specimens because the anterior part of the palate is not visible in either specimen as it is covered in matrix. However, physical inspection of other specimens (e.g., SAM-PK-K11187) reveals the presence of these foramina. As mentioned by Keyser (1965), the premaxillae form the small medial portion of the anterior border of the choanae (cho, Fig. 6), and laterally is the articular surface for the palatine (aspal, Fig. 6). There is a posterior median palatal ridge (pmrpmx, Fig. 6), no anterior median palatal ridges but lateral palatal ridges are present (lpr, Fig. 6). The lateral palatal ridges border the premaxilla laterally and are significantly thicker than the posterior median palatal ridge. Between the lateral anterior palatal ridges, the surface of the secondary palate is deeply domed, similar to the morphology present in *Compsodon* (Angielczyk and Kammerer, 2017). As in other dicynodonts (e.g., *K. kitchingi*, *Compsodon*), the lateral palatal ridge marks the border with the maxilla. The posterior median palatal ridge can be regarded as the ventral thickening of the nasal septum. Specifically, the ridge is formed by the portion of the premaxilla that covers the vomerine septum in this region of the secondary palate. Unlike *Compsodon*, the height of the median palatal ridge is constant anteroposteriorly. As in *Kembawacela* (Angielczyk et al. 2019, Araújo et al. 2022b), there is an oval depression (odpmx, Fig. 6) between the lateral ridge and the posterior median palatal ridge. This depression is an elongated ellipse (groove-like depressions according to Angielczyk & Kammerer 2017) in *Compsodon*.

Unlike *K. kitchingi* in which the premaxilla forms the anterior and dorsal margin of the external nares (Angielczyk et al. 2019), in *Cistecephalus* the premaxilla only forms the anterior margin, whereas the dorsal margin is entirely formed by the nasal. The short nasal septum, “internasal septum” following Keyser’s (1965, 1973) nomenclature, is formed by a single crest anteriorly, that diverges into two posteriorly pointing processes (ppns, pointed processes of the nasal septum), which then slope ventrally to form two subparallel low crests for the remaining half of the premaxilla (lcns, low crests of the nasal septum).There are also two short crests, that terminate in short pointed processes unsupported by the palatal surface of the premaxilla, that run parallel to the nasal septum and are separated by a shallow concavity (pscns, parallel short crests of the nasal septum).

Septomaxilla

The septomaxilla is not observable in the segmented specimens (SAM-PK-K011474 and SAM-PK-K6814). Despite the excellent quality of the scan and contrast between rock matrix and bone, the septomaxilla does not seem to be preserved in the specimen, apparently due to erosion. However, if preserved, along the posterior border of the external nares, it is indistinguishable in the trabecular structure with the surrounding bone, hence, extremely co-ossified and remodeled. It is important to note that the broad, recurved base of the premaxilla ascending process visible near the anterior border of the external nares could be confounded with the septomaxilla.

Maxilla

The maxilla is formed by the posterolateral ramus (plrmx, Fig. 6), the palatal component (pcmx, Fig. 6) and the facial component (fcpmx, Fig. 6). The posterolateral ramus is broad anteroposteriorly, in contrast to *K. kitchingi* (Angielczyk et al. 2019). There is a double embayment on the ventral aspect of the palatal component of the maxilla (demx, Fig. 6). The anterior embayment is anterior to the caniniform process, as seen in many emydopoids, whereas the more incipient posterior embayment is aligned with and slightly posterior to the caniniform process. On the ventral side of the posterolateral ramus, there is a round fossa (rfmx, Fig. 6) pierced by a small foramen at the intersection with the facial component of the maxilla, an autapomorphy of *Cistecephalus*. The angle formed by the lateral border of the facial component of the maxilla and the anterior border of the posterolateral ramus is slightly obtuse. The postcaniniform keel is laterally convex. A secondary lateral crest forms forms a horizontal slot joint with the suture with the premaxilla (lcmx, Fig. 6), and represents the maxillary contribution to the palatal rim. On its dorsal surface the maxilla forms the median and ventral

walls of the maxillary antrum, as well as part of the anteromedial wall. The triradiate crest dividing the maxillary antrum and the nasal cavity on the dorsal side of the maxilla is here referred to as the dorsal vertical crest of the maxilla (dvcmx, Fig. 6). Keyser (1965, 1973) mentioned a groove near the dorsal vertical crest, but its exact location is not clear from his description. At the intersection between the secondary crest and dorsal vertical crest of the maxilla in SAM-PK-6814 there is a well-delimited groove on the dorsal floor of the maxilla lateral to the crest. This crest continues into a canal anteriorly, forming part of the cast of the infraorbital/maxillary canal [see Keyser (1965, 1973) description]. This canal exits on the facial side of the maxilla. It seems that Keyser (1965, 1973) misinterpreted the labial fossa as the posterior opening of the maxillary antrum. Indeed, the maxillary antrum is not exposed ventrally, being surrounded by the maxilla and lacrimal only. The labial fossa as described by Ewer (1961) and Cluver & King (1983), being surrounded by the palatine, jugal and maxilla is not present.

Nasal

Expanding on Keyser's (1965, 1973) description, we note that the anterior portion of the nasals is overlapped by the premaxilla (i.e., there is an internal continuation of the nasals that extends anteriorly beyond their anterior edge on the external surface of the skull roof). Likewise, there is a posterior extension of the nasals that overlaps the frontals. Indeed, both the nasal and the frontal have expanded sutural surfaces such that the two bones interlock. The frontal underplates the nasal medially, whereas the nasal is under the frontal more laterally. The ventral surface of the nasal is flat, except laterally where it forms a short descending irregularly-shaped descending process (ldpn, lateral descending process of the nasal, Fig. 5). As typical for other dicynodonts, the nasals are covered in minute foramina on their dorsal surface.

Prefrontal

The prefrontal-lacrimal-maxilla-jugal region of the skull is particularly complex as several bones intersect with inter-digitating sutures, making clear segmentation of the elements difficult. Nevertheless, segmentation in both specimens (SAM-PK-6814 and SAM-PK-K011474) resulted in similar morphology. In dorsal view, the prefrontal is a simple subtriangular, plate-like bone with a somewhat hyperbolic shape. The dorsal half is thicker than the ventral half and most of the prefrontal is covered by the lacrimal. Medial to the orbital exposure of the lacrimal, the prefrontal forms a small part of the orbital wall lateral to the frontal contribution. The dorsal exposure of the prefrontal is minimal, making it easy to confuse with surrounding bones in less well-preserved specimens.

Lacrimal

The lacrimal is composed of a short anterior flange (afl, Fig. 5) and the larger posterior flange (pfl, Fig. 5) that forms part of the anterior margin of the orbit. The anterior and posterior flanges are united dorsally. Our segmentation indicates that the lacrimal is contacted by the jugal laterally, but not ventrally (as mentioned by Keyser 1965, 1973). The maxilla forms the entire ventral floor of the lacrimal. As segmented, our assessment also differs from Keyser's on account of the lack of contact between the lacrimal and the nasal/frontal. The lacrimal nearly touches the frontal, but it is separated by the thin prefrontal. However, this contact is seen in other specimens (e.g., BSP 1932-I-502, BPS 1932-I-56). The lacrimal converges posteriorly with medial borders of the palatal component of the maxilla. In addition to the lacrimal foramen, there is a small foramen in the dorsomedial corner of the lacrimal (dmfl, Fig. 5). Keyser (1965, 1973) describes most important information about the lacrimal foramen (lf, Fig. 5). Our main new observations are that the lacrimal foramen connects to the maxillary antrum internally and is located on the ventromedial corner of the bone, forming a semicircular notch.

Jugal

The jugal is formed by three anatomical subunits: the 'anterior' process ('a'pj, Fig. 8), the posteroventral process (pvpj) and the ascending process (aspj). The ascending process is lanceolate, the posteroventral process is subtriangular, and the 'anterior' process is semilunate and is one of the most distinguishing features of *Cistecephalus*. Indeed, the 'anterior' process is a medial deflection from the conjunction of the posteroventral and ascending processes, such that it does not develop anteriorly, but rather medially. This condition is distinct from *Kembawacela* sp. (Angielczyk et al. 2019, Araújo et al. 2022b) because the foot-like anterior process develops anteriorly and smoothly turns medially. In *Cistecephalus*, the 'anterior' process sharply turns medially, and this inflection contributes to the frontation of the orbits

especially in larger specimens. It also differs from *Compsodon*, *Digalodon* or *Emydops* (Fröbisch & Reisz 2008, Kammerer et al. 2015, Angielczyk & Kammerer 2017) where there is little lateral exposure of the anterior process of the jugal, which instead mostly forms the floor of the mostly orbit. The 'anterior' process is thickened along its anteriormost border. Anteromedially, the jugal forms the lateral and most of the anterior wall of the maxillary antrum (medial jugal excavation; mje). The ascending process is oriented posteriorly when compared to other cistecephalid taxa, with the jugal notch (jn, Fig. 8) forming a rounded acute angle (~60º) between the ascending process and the posteroventral process. The articular surface with the squamosal (assq, Fig. 8) on the posteroventral process is lanceolate.

Frontal

The midfrontal suture is highly interdigitated with complex corrugations along its anteroposterior length. Similarly, the articular surface of the nasal (asn, Fig. 5) leaves a subtriangular imprint on the dorsal surface of the frontal, as segmented, but the contact between the two bones is highly interdigitated as described by Kammerer (2021). The orbital surface of the frontal is concave. The anterior third of the lateral surface of the frontal contributed to the orbit and is ornamented by the supraorbital ridges of the frontal dorsally (sof, Fig. 5), whereas the posterior two-thirds form the lateral contact with the postorbital. Keyser (1973) offered little insight on the nature of the frontal-postorbital suture, referring to an "uneven suture". At the midlength of the frontal part of the supraorbital ridge, the postorbital interdigitates with the frontal leaving a subtriangular articular surface when viewed from the lateral side (aspo, Fig. 5). However, the lobate posterior extension of the frontal (lpe, Fig. 5) overlaps a significant portion of the anteromedial portion of the postorbital in a tight interdigitating suture. More medially, the ventral surface of the frontals is marked by the posteriorly-converging descending flanges (fdf, frontal descending flanges, Fig. 5) that continue onto the parietal. Medial to the descending flanges the frontals are excavated ventrally to form the dorsal enclosure of the olfactory tract (fve, frontal ventral excavations, Fig. 5), which becomes shallower posteriorly. The sutural contact between the frontal and prefrontal is consistent in general shape, yet difficult to precisely delineate due to co-ossification, in both specimens (SAM-PK-K011474 and SAM-PK-K6814) resulting in some asymmetry. The anteroventral corner of the frontal interdigitates and co-ossifies in some places with the posterior and dorsal borders of the prefrontal.

Postfrontal

A distinct postfrontal could not be identified. Similar to the situation in *K. kitchingi* (see below), it is not clear whether a primordial postfrontal ossification center fuses with the postorbital early in ontogeny, or if the element is deleted completely.

Parietal

Keyser (1965, 1973) described the parietal as being shaped like a right-angled triangle. However, its shape is rather chevron-like with the anterior border having a short projection near the midline of the skull (sapp, short anterior projections of the parietal, Fig. 5). Lateral to the short anterior projections there is an internal anterior process (iapp, Fig. 5) near the junction between the frontal, postorbital and parietal. The contact with the frontals is interdigitating medially, but becomes a simple butt joint laterally. Posteriorly, the parietals are overlapped by the postparietal, such that the parietals develop a deep central invagination in their posterior margin that accepts an anterior process of the postparietal. In ventral view, the descending flanges of the parietals (dfp, Fig. 5) are convex laterally and extend the entire length of the elements. The descending flanges arise from the near-vertical section of the parietal near the dorsal portion of the foramen magnum. Moving anteriorly, the descending flanges diverge and then smoothly curve medially to become subparallel. The canal passing though the parietals to form the pineal foramen is hourglass-shaped.

Postorbital

The postorbital is significantly better preserved in SAM-PK-K6814 when compared to the specimen examined by Keyser (1965, 1973), providing additional anatomical information. The postorbital receives the frontal dorsally forming a biconcave suture (see frontal description), delimited by a thin ridge (pofr, postorbital-frontal ridge, Fig. 5). The transition between the dorsal and ventral surfaces of the temporal component of the postorbital forms an acute crest (ctcpo, crest of the temporal component of the postorbital, Fig. 5), resulting in the bi-planar appearance typical of most emydopoids. Posteriorly, this crest along the temporal component of the

postorbital is faceted to produce a lanceolate articular surface for the squamosal (assq, Fig. 5) with the acute angle pointing anteriorly. As in *K. kitchingi*, the articular surface for the jugal is located on the posterior aspect of the descending process of the postorbital, unlike *K. yajuwayeyi* where it is on the medial surface (Discrete Character 192). The postorbital bulge, visible in ventral view, is a flat subtriangular projection anteriorly that continues as a straight ventral crest along the temporal component of the postorbital, similar to that observed in *K. yajuwayeyi* (Araújo et al. 2022b), in that it is a flat subtriangular region anteriorly that continues as a straight ventral crest along the temporal component of the postorbital.

Squamosal

The four anatomical subunits of the squamosal are: the zygomatic process (zpsq, Fig. 8), the dorsal process (dpsq, Fig. 8), the ventral process (vpsq, Fig. 8) and the lateral process (lpsq, Fig. 8). The zygomatic process bows dorsally, and its anteriormost tip sharply pointed. There is a strong lateral crest along the lateral aspect of the zygomatic process of the squamosal. At its anterior end, the cross-section of the zygomatic process is crescentic with the concavity pointing dorsomedially; at midlength it becomes an isosceles triangle, with the obtuse angle located dorsomedially; and near the lateral process it becomes aerofoil shaped with the trailing edge pointing laterally. The connection of the zygomatic process of the squamosal with the posterior region of the bone is made by the lateral process, which is subtriangular in posterior view.

The termination of the zygomatic process of the squamosal continues posteriorly as a vertical buttress along the anterior aspect of the dorsal process of the squamosal (avbdpsq, anterior vertical buttress of the dorsal process of the squamosal), which bends medially at its dorsal end. Medial to the vertical buttress there is a broad recess, somewhat ovoid, and delimited medially by the medial border of the dorsal process of the squamosal (mardpsq, medioanterior recess of the dorsal process of the squamosal). Lateral to the anterior vertical buttress, there is a subrectangular flange (lfdpsq, lateral flange of the dorsal process of the squamosal), which is significantly mediolaterally narrower than the medioanterior recess of the dorsal process of the squamosal. The dorsal process of the squamosal is subrectangular but with the dorsal portion bent medially, in posterior view. In lateral view, there is a conspicuous anterior deflection of the dorsal process of the squamosal.

Keyser (1965, 1973) described the quadrate recess (qr, Fig. 8) and the crests delimiting it, but there are various anatomical details that were missing in his description. The quadrate recess is oval, being laterally and medially delimited by the lateral and medial crest of the squamosal's quadrate recess (lcsqr, mcsqr Fig. 8), respectively. The lateral crest is vertically-oriented, straight, and thinner but more pronounced than the medial crest. The medial crest is dorsomedially convex and extends more dorsally than the lateral crest. The ventralmost border of the squamosal in the quadrate recess area terminates abruptly and this region is posteriorly convex. The tympanic process (*sensu* Cox, 1959) is entirely formed by the opisthotic (*contra* Keyser 1965, 1973).

Vomer

Keyser (1965, 1973) claimed that the vomers are paired, but we do not find any sutural markings internally. Importantly, the images that allegedly show the separation between the vomers either point to a coronal section without the vomer (fig. 17, Keyser 1973), or show only a single median bone with no suture visible (fig. 20, Keyser 1973). In the specimens described here (SAM-PK-K6814 and SAM-PK-K011474), the median anterior projection of the vomer fits in between the premaxilla, and there is no anterior separation with the bone. The cultriform process of the vomer (cpv, Fig. 6) is subtrapezoidal in lateral view, with the ventral border substantially thinner than the dorsal region. The ventral exposure of the vomer has subparallel crests that open and curve slightly posteriorly. The subtriangular mid-ventral vomerine plate (mvvp, Fig. 6) terminates posteriorly as two processes that form the ventral crests of the vomer (vcv, Fig. 6). In between the ventral crests of the vomer is the interpterygoid vacuity (iptv, Fig. 6), which, despite the name of the structure, is closed entirely by the cultriform process except for a small ventroposterior portion. This differs from *K. yajuwayeyi* where the vacuity seems to be mostly covered by the parasphenoid (Araújo et al. 2022b). Thus, the vestigial interpterygoid vacuity remains as a narrow cleft. Irrespective of the bones involved, the closure of the interpterygoid vacuity is a prevalent cistecephalid feature (Broili & Schröder 1935; Cox 1972; Keyser 1973; Cluver 1974a). On the dorsal aspect of the cultriform process of the vomer there are two dorsal crests that taper into acute

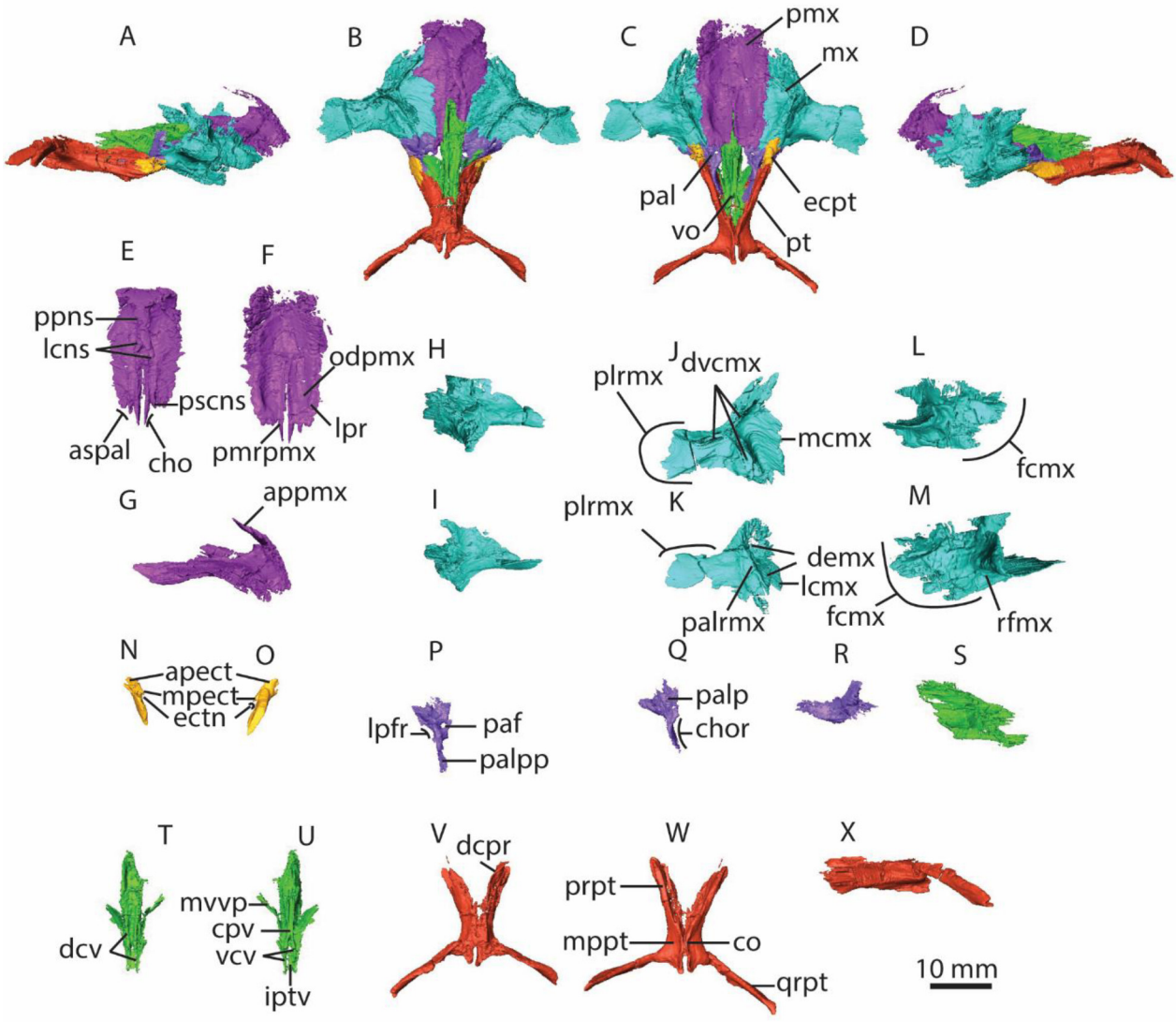

FIGURE 6. Palatal elements of SAM-PK-6814. A, right lateral view; B, dorsal view; C, ventral view; D, left lateral view; E, premaxilla in dorsal view; F, premaxilla in ventral view; G, premaxilla in lateral view; H, anterior view of the left maxilla; I, posterior view of the right maxilla; J, dorsal view of the right maxilla; K, ventral view of the right maxilla; L, lateral view of the left maxilla; M, lateral view of the left maxilla; N, left ectopterygoid in dorsal view; O, right ectopterygoid in dorsal view; P, left palatine in dorsal view; Q, right palatine in ventral view; R, right palatine in lateral view; S, vomer in lateral view; T, vomer in dorsal view; U, vomer in ventral view; V, pterygoid in dorsal view; W, pterygoid in ventral view; X, pterygoid in lateral view. Abbreviations: apect, anterior process of the ectopterygoid; appmx, median spine of the premaxilla; aspal, articular surface for the palatine; cho, choana; chor, choana recess; co, crista oesophagea; cpv, cultriform process of the vomer; dcpr, dorsal crest of the palatal ramus of the pterygoid; dcv, dorsal crests of the vomer; demx, double embayment of the palatal component of the maxilla; dvcmx, dorsal vertical crest of the maxilla; ecpt, ectopterygoid; ectn, ectopterygoid notch; fcmx, facial component of the maxilla;iptv, interpterygoid vacuity; lcmx, lateral crest of the maxilla; lcns, low crests of the nasal septum; lpr, lateral palatal ridges; lpfr, lateral palatal foramen recess; mcmx, medial crest of the maxilla; mpect, medial process of the ectopterygoid; mppt, median pterygoid plate; mvvp, mid-ventral vomerine plate; mx, maxilla; odpmx, oval depression of the premaxilla; paf, palatine foramen; pal, palatine; palp, palatine pad; palpp, palatine posterior process; palrmx, palatal rim of the maxilla; pmx, premaxilla; ppns, pointed processes of the nasal septum; plrmx, posterolateral ramus of the premaxilla; plrmx, posterolateral ramus of the maxilla; prpt, palatal ramus of the pterygoid; pscns, parallel short crests of the nasal septum; pt, pterygoid; qrpt, quadrate ramus of the pterygoid; rfmx, round fossa of the maxilla; vcv, ventral crests of the vomer; vo, vomer.

processes (dcv, Fig. 6), which resemble *K. yajuwayeyi* (Araújo et al. 2022b).

Palatine

The palatines do not extend beyond the choanae anteriorly (*contra* Keyser 1965), but terminate at the level of the choanae (chor, choanal recess of the palatine, Fig. 6). The ventral surface of the palatine pad (palp, Fig. 6) is smooth, lacking the rugosity seen in most bidentalians. The palatine foramen perforates the anterior portion of the palatine pad along an anteriorly-angled path. On the lateral aspect of the palatine between the pad-like anterior region and the posterior process there is a slight excavation to form the lateral palatal foramen (lpfr, lateral palatal foramen recess, Fig. 6), which is slit-like and easily distinguishable from the subcircular palatine foramen. The medial face of the palatine is concave and forms the walls of the choanae together with the vomer. The palatine posterior process forms a distinct crest (palpp, Fig. 6), unlike *Kembawacela* sp. (Angielczyk et al. 2019, Araújo et al. 2022b) where the palatine has a relatively flat posterior process.

Ectopterygoid

The ectopterygoid is rhomboidal in lateral view, and is mediolaterally as thick as the anteriormost portion of the palatal ramus of the pterygoid. There is a short anterior projection (apect, anterior process of the ectopterygoid; Fig. 6) overlapping the posteriormost portion of the palatal component of the maxilla. Along the anteroventral border of the ectopterygoid there is a short posteriorly-oriented medial process (mpect, medial process of the ectopterygoid) that has a notch posteriorly that forms the lateral wall of the palatal foramen (ectn, ectopterygoid notch).

Pterygoid

The pterygoid is formed by the palatal ramus anteriorly (prpt, Fig. 6), and the quadrate ramus posteriorly (qrpt, Fig. 6), which contact each other medially at the median pterygoid plate (mptp, Fig. 6). The palatal ramus is thinner ventrally than dorsally, and bows laterally in dorsal view, whereas in ventral view it is straight. The medial surfaces of the palatal rami suture dorsally with the mid-ventral vomerine plate along most of the latter's anteroposterior extension, and the dorsal half of the palatal ramus sutures with the palatine posterior process ventrally, approaching the median pterygoid plate. The mid-ventral vomerine plate is flush with the dorsal crest of the palatal ramus (dcpr, Fig. 6). There is no distinct ventral keel of the pterygoid as in *K. yajuwayeyi* (Araújo et al. 2022b).

The cristae oesophagea (co, Fig. 6) do not meet medially, forming a slit that closes more dorsally by the medial interdigitation of the pterygoids. The cristae slightly diverge anteriorly, nearly touch at midlength and then diverge slightly posteriorly again. The cristae are thicker posteriorly, and form blunt and short posterior processes, which are distinct from the acute posterior processes of *K. yajuwayeyi* (Araújo et al. 2022b). The cristae are also thicker ventrally forming a distinct rim from the lateral ala of the median pterygoid plate.

In posterior view, the ventral border between the quadrate ramus of the pterygoid and the median plate of the pterygoids is sigmoidal. In cross-section, the quadrate ramus is teardrop-shaped anteriorly with the apex pointed dorsally, and becomes reniform posteriorly, with the concavity oriented posteriorly throughout. Similar to *Myosaurus*, most of the parasphenoid rostrum forms an anteriorly projecting process that overhangs the pterygoids but it is not exposed ventrally as in *K. yajuwayeyi* (see Araújo et al. 2022b). The pterygoid suture with the basisphenoid slopes posteriorly and is co-ossified to some extent (Fig. 4), as in *K. kitchingi* (Angielczyk et al. 2019). Additionally, it is interesting to note that the anteriormost extension of the basisphenoid overhangs the dorsal surface of the pterygoids, without any contact.

Our observations differ from Keyser's (1965, 1973) description of the interpterygoid vacuity: "the two pterygoids approach one another closely, but are separated by a thin vertical plate extending ventrally from the basisphenoid, thus forming a rudimentary interpterygoid vacuity" (page 52, Keyser 1973). Furthermore, Keyser's Plate XVI does not pass through the interpterygoid vacuity. Our observations indicate that the interpterygoid vacuity is bordered posteriorly only by a small segment of the crista oesophagea. Predominantly, the vacuity is flanked by two gently diverging ventral crests of the vomer (see Vomer). Interestingly, there is a large canal passing through the pterygoids medially between the crista and dorsal contact between these bones.

Epipterygoid

In SAM-PK-6814 only a small sliver of the ascending ramus of the left epipterygoid is preserved. The right

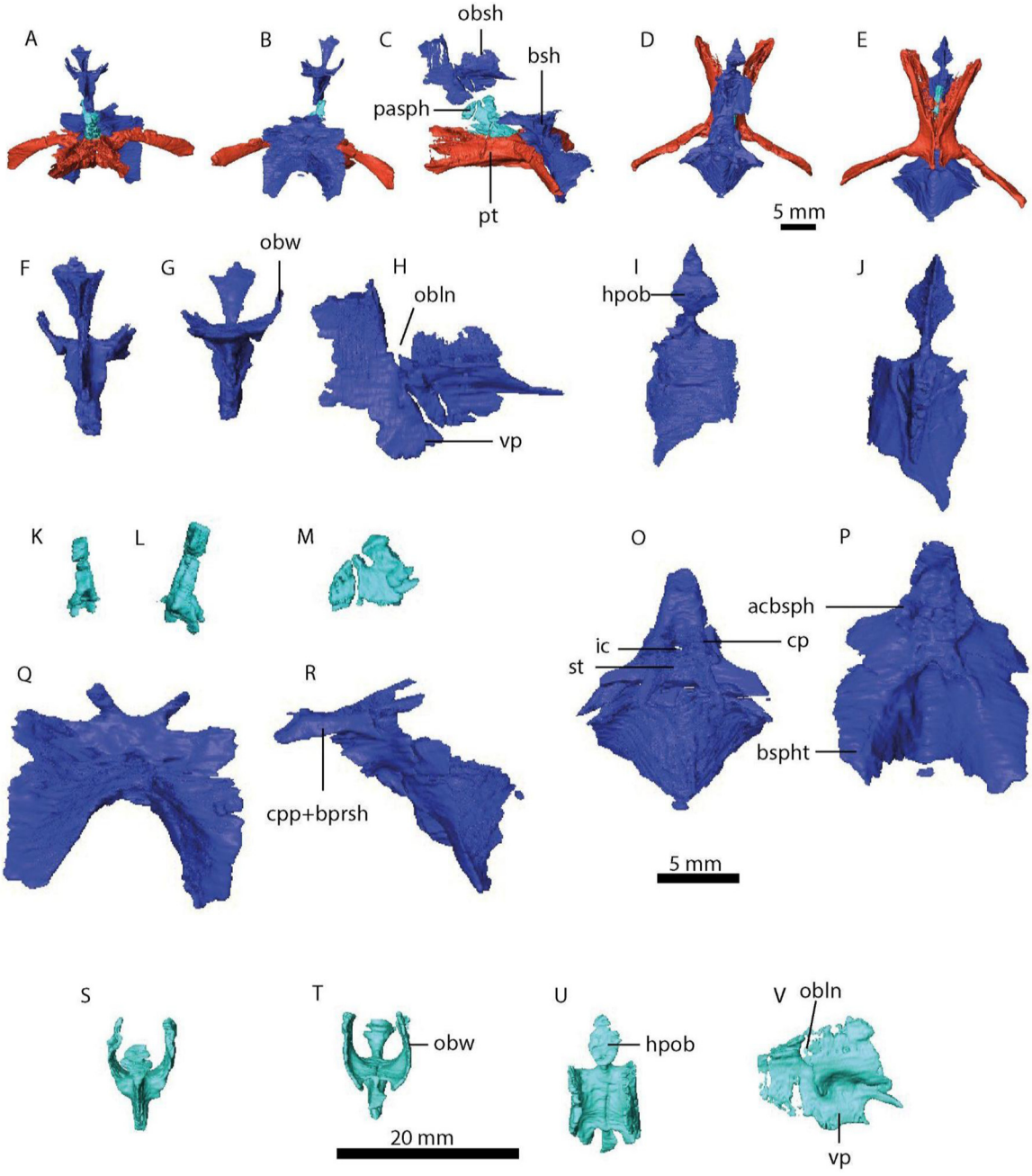

FIGURE 7. Internal cranial bones of SAM-PK-K6814 and SAM-PK-K011474. A, internal cranial bones of SAM-PK-K6814 in anterior view; B, internal cranial bones of SAM-PK-K6814 in posterior view; C, internal cranial bones of SAM-PK-K6814 in left lateral view; D, internal cranial bones of SAM-PK-K6814 in dorsal view; E, internal cranial bones of SAM-PK-K6814 in ventral view; F, SAM-PK-K6814 orbitosphenoid in anterior view; G, SAM-PK-K6814 orbitosphenoid in posterior view; H, SAM-PK-K6814 orbitosphenoid in lateral view; I, SAM-PK-K6814 orbitosphenoid in dorsal view; J, SAM-PK-K6814 orbitosphenoid in posterior view; K, SAM-PK-K6814 orbitosphenoid in ventral view; L, SAM-PK-K6814 orbitosphenoid in dorsal view; M, SAM-PK-K6814 orbitosphenoid in lateral view; O, SAM-PK-K6814 basisphenoid in dorsal view; P, SAM-PK-K6814 basisphenoid in ventral view; Q, SAM-PK-K6814 basisphenoid in posterior view; R, SAM-PK-K6814 basisphenoid in lateral view; S, SAM-PK-K011474 orbitosphenoid in anterior view; T, SAM-PK-K011474 orbitosphenoid in posterior view; U, SAM-PK-K011474 orbitosphenoid in dorsal view; V, SAM-PK-K011474 orbitosphenoid in lateral view. Abbreviations: acbsph, anterior crest of the basisphenoid; bsh, basisphenoid; bspht, basisphenoidal tubera; cp, clinoid process; cpp+bprsh, cultriform process of the parasphenoid and basipresphenoid; ic, internal carotid foramen; hpob, horizontal plate of the orbitosphenoid; obln, orbitosphenoid lateral notch; obsh, orbitosphenoid; obw, orbitosphenoid wings; pasph, parasphenoid; pt, pterygoid; st, sella turcica; vp, vertical process of the orbitosphenoid.

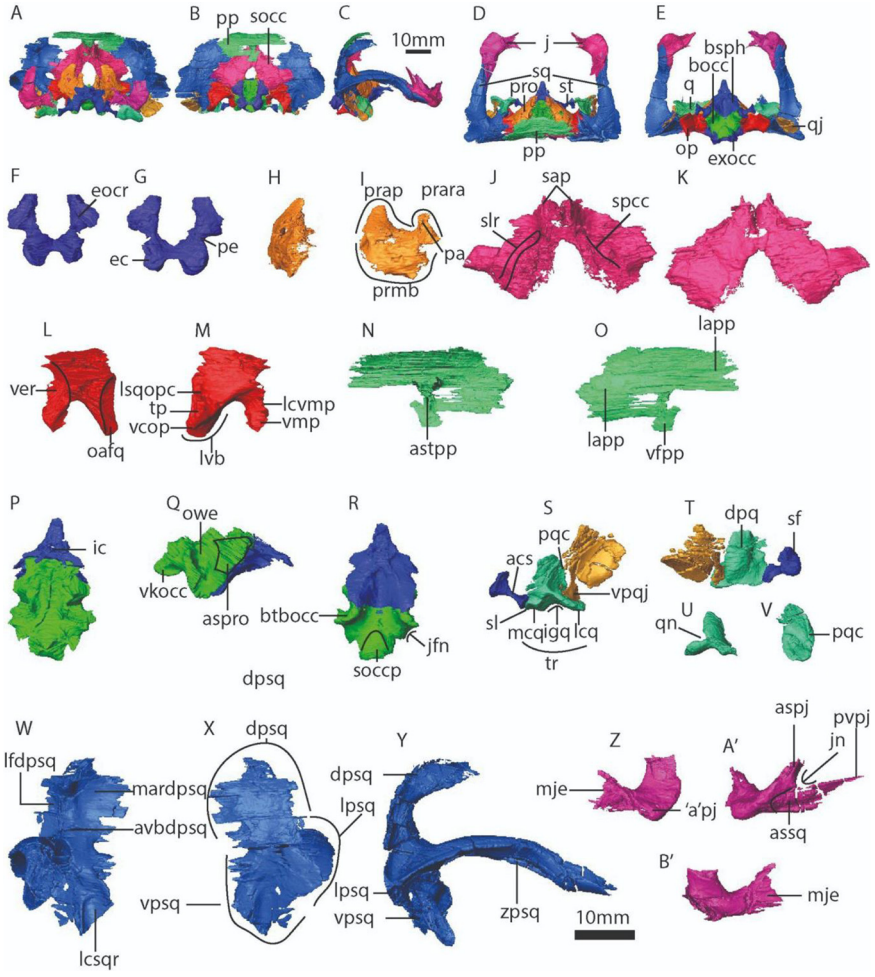

FIGURE 8. Braincase elements and jugal of SAM-PK-K6814. A, anterior view of the articulated braincase and jugal ; B, posterior view; C, lateral view, D, dorsal view, E, ventral view, F, exoccipital in anterior view, G, exoccipital in posterior view; H, prootic in anterior view; I, prootic in lateral view; J, supraoccipital in anterior view; K, supraoccipital in posterior view; L, opisthotic in anterior view; M, opisthotic in posterior view, N, postparietal in anterior view; O, postparietal in posterior view; P, basisphenoid and basioccipital in dorsal view; Q, basisphenoid and basioccipital in lateral view; R, basisphenoid and basioccipital in ventral view; S, quadrate, quadratojugal and stapes in anterior view; T, quadrate, quadratojugal and stapes in dorsal view; U, quadrate in posterior view; U, quadrate in lateral view; V, right squamosal in anterior view; X, right squamosal in posterior view; Y, right squamosal in lateral view; Z, left jugal in anterior view; A', left jugal in lateral view; B', left jugal in posterior view. Abbreviations: acs, anterior crus of the stapes; 'a'pj, 'anterior' process pof the jugal; aspj, ascending process of the jugal; assq, articular surface with the squamosal; aspro, basioccipital articular surface for the prootic; astpp, anterior subtriangular tuberosity of the postparietal; avbdpsq, anterior vertical buttress of the dorsal process of the squamosal; bocc, basioccipital; bsph, basisphenoid; btbocc,basal tuber of the basioccipital; dpq, dorsal process of the quadrate; dpsq, dorsal process of the squamosal; ec, exoccipital condyle; eocr, exoccipital descending crest; exocc, exoccipital; ic, internal carotid foramen; igq, intercondylar groove of the quadrate; j, jugal; jn, jugal notch; jnf, jugal foramen notch; lapp, lateral alae of the postparietal; lcsqr, lateral crest of the squamosal's quadrate recess; lcq, lateral condyle of the quadrate; lcvmp, lateral crest of the opisthotic ventromedial process; lfdpsq, lateral flange of the dorsal process of the squamosal; lpsq, lateral process of the squamosal; lsqopc, lateral squamosal-opisthotic crest; lvb, lateral vertical buttress; mardpsq, medioanterior recess of the dorsal process of the squamosal; mje, medial jugal excavation; mcq, medial condyle of the quadrate; mcsqr, medial crest of the squamosal's quadrate recess; oafq, opisthotic articular facet; op, opisthotic; owe, oval window excavation; pa, pila antotica; pe, pedicle; pp, postparietal; pqc, posterior quadrate crest; prap, prootic alar process; prmb, prootic main body; pro, prootic; pvpj, posteroventral process of the jugal; q, quadrate; qj, quadratojugal; qn, quadrate notch; sap, supraoccipital anterior processes; sf, stapedial footplate; sl, stapedial lip; slr, supraoccipital-opisthotic lateral recess; socc, supraoccipital; soccp, semioval occipital condyle prominence; spcc, supraoccipital-prootic coronal crest; sq, squamosal; st, stapes; ver, vestibular recess; vcop, ventral crest of the opisthotic; vfpp, ventral flange of the postparietal; vkocc, ventral knob of the occipital condyle; vmp,ventromedial process of the opsithotic; vpqj, ventral process of the quadratojugal; vpsq, ventral process of the squamosal; tr, trochlea; tp, tympanic process; zpsq, zygomatic process of the squamosal.

epipterygoid has a longer portion preserved but it is very damaged and fragmented (see Supplementary Information).

Parabasisphenoid

The thin plate of bone composing the parasphenoid, also described by Keyser (1965, 1973), is subtriangular and lies dorsal to the anteriormost portion of the parasphenoid rostrum. This thin plate is clearly distinguishable from the surrounding bones, but there is no separation between the cultriform process of the parasphenoid and the basipresphenoid (cpp + bprsh, Fig. 7, 8). Contrary to Keyser (1965, 1973), we can clearly observe the separation between the basipostsphenoid and the basioccipital in the tomographic slices, but we agree that there is no unossified zone between these bones. The basisphenoidal tubera are formed by a hyperbolic-shaped plate of bone and are subtriangular in lateral view. The anterior surface of the basisphenoidal tubera (bspht, Fig. 7, 8) develops two converging crests that form an X-pattern at the junction with the cultriform process (acbsph, anterior crest of the basisphenoid). These crests form the sutural contact with the pterygoid. The sutural contact with the prootic follows the lateral flanges of the basisphenoidal tubera, which deflect medially. However, the sutural contact with the prootic also continues farther medially as two posterior processes (the clinoid processes; cp, Fig. 7, 8). extending from the crests lateral to the sella turcica (st, Fig. 7, 8) A single carotid foramen is observed on the dorsal aspect of the basipostsphenoid, near the contact with the pterygoid. Internally the single branch bifurcates into two canals for the cerebral carotids, which then exit via paired carotid foramina on the ventral surface of basipostpshenoid as in other specimens such as SAM-PK-K10554 and as mentioned by Broili & Schröder (1936).

Ethmoid

The ethmoid, or 'anterior plate', anatomy is complex and its homologies with extant mammal are not trivial (Cluver 1971). Here, we follow the three-bone homology scheme provided by Crompton et al. (2017), which can be easily identified in *Cistecephalus*. The most anterior element is the mesethmoid, which coossifies to the fused orbitosphenoid (the wings) and presphenoid (the vertical process). Few additional anatomical observations are possible for this element in SAM-PK-6814 because the orbitosphenoid wings and mesethmoid posterior wall are damaged. However, the ethmoid of SAM-PK-K011474 is nearly complete. There is an orbitosphenoid lateral notch (obln, Fig. 7), but it is indented as in *Kawingasaurus* or *Myosaurus* and unlike *Pristerodon*, which possesses an anteroposteriorly-elongated notch (Macungo et al. 2022). There is a horizontal plate of the mesethmoid (hpmsth, Fig. 7) as in *Pristerodon* (Character 193), and no dorsal fossa as in *Myosaurus* (Character 194). The presphenoid vertical process or septum (cf. Keyser 1965, 1973) is anteroposteriorly short when compared to *Kawingasaurus*, but similar to *Pristerodon* (Macungo et al. 2022). The presphenoid vertical process reaches (psph, Fig. 7) the ventral aspect of the palate contacting the parasphenoid, unlike *Myosaurus* (Character 195).

Basioccipital

The ventral knob of the occipital condyle (vkocc, Fig. 8), the basioccipital condyle, is semilunate in shape in posterior view, and it is clearly demarcated from the rest of the bone by a semi-oval prominence ventrally (soccp, Fig. 8), as in *Compsodon* (Angielczyk & Kammerer 2017). The contact with the exoccipital is teardrop-shaped. Anterior to the basioccipital condyle is an excavation that forms the ventral floor of the jugular foramen (jfn, jugal foramen notch, Fig. 8). This structure is marked posteriorly by the posterior crest delimiting the oval window (btbocc, basal tuber of the basioccipital, Fig. 8), which is somewhat conical with the apex pointing ventrally. The prootic contact is subtrapezoidal (aspro, Fig. 8) and is located anteriorly relative to the oval window (owe, oval window excavation, Fig. 8), despite being oriented dorsolaterally. What Keyser (1965, 1973) considered the internal acoustic meatus is essentially the vestibule for the inner ear, which opens dorsal to the oval window excavation (see Endosseous Labyrinth).

Stapes

As segmented, both right and left stapes of SAM-PK-K6814 do not have a fully-enclosed stapedial foramen. Figure 10 in Keyser (1973) does show the stapedial foramen, but not the posterior crus as in SAM-PK-K6814 described here (as for most dicynodonts, see Angielczyk 2007). However, the posterior crus is preserved in SAM-PK-K011474, demonstrating the presence of a completely enclosed stapedial foramen in that specimen (sfor, Fig. 9). In both specimens the stapes has a dumbbell shape, although the right stapes in SAM-PK-K011474 is damaged, with the stapedial head being significantly

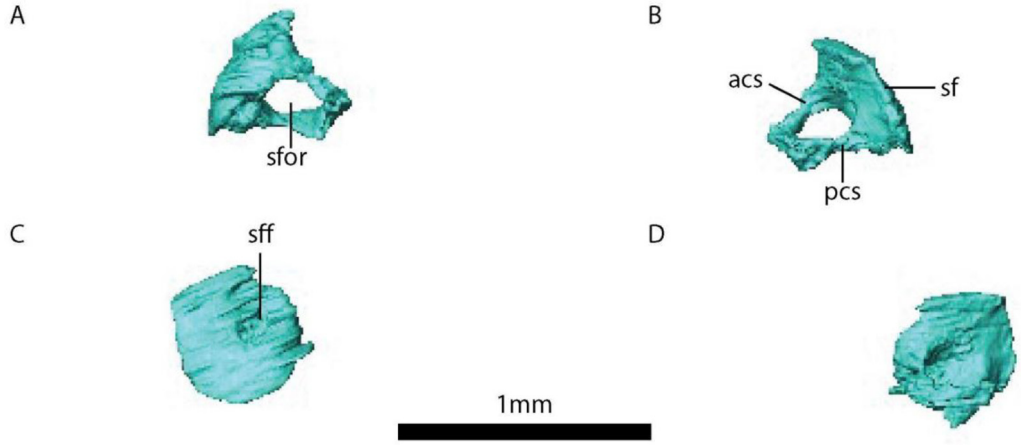

FIGURE 9. Stapes of SAM-PK-K011474. A, Dorsal view, B, ventral view, C, medial view, D, lateral view. Abbreviations: acs, anterior crus of the stapes; pcs, posterior crus of the stapes; sf, stapedial footplate, sff, stapedial footplate foramen; sfor, stapedial foramen.

smaller than the footplate (sf, Fig. 8, 9). As in *Kawingasaurus* and *K. kitchingi* (Laaß 2015, Angielczyk et al. 2019), there is a central concavity in the stapedial footplate, where a small foramen pierces through (stapedial footplate foramen, sff, Fig. 9). Similarly, the stapedial head is concave but is teardrop-shaped with the apex pointing posteriorly in SAM-PK-K6814. The anterior border of the anterior crus (acs, anterior crus of the stapes, Fig. 8, 9) is concave, and the posterior border is semicircular to accommodate the stapedial artery. The dorsal region of the stapedial footplate is thinner dorsally where it forms a distinct laterally-oriented rim. Additionally, there is no distinct dorsal process of the stapes, as in *Kombuisia* (Fröbisch 2007).

Quadrate

As typical for dicynodonts, the trochlea (tr, Fig. 8) is formed by two easily distinguishable condyles, but it differs from *Cistecephaloides* and *Kawingasaurus,* in which the condyles are reduced in size.

The trochlea is as robust as in *K. yajuwayeyi*, but less developed than in *Niassodon*. The lateral condyle (lcq, Fig. 8) is flat and angles ventrolaterally, whereas it is gently ventrally concave in *Niassodon* and *K. yajuwayeyi*, but convex in *Compsodon* (Angielczyk & Kammerer 2017). The lateral condyle is significantly longer anteroposteriorly than the medial condyle (mcq, Fig. 8) as in *Compsodon* (Angielczyk & Kammerer 2017), whereas this difference is smaller in *Niassodon* (Character 196). The lateral and medial condyle angle is approximately 100° (as *K. yajuwayeyi*), whereas *Niassodon* is ~93°. The medial condyle has the typical subrectangular shape, but its dorsal border forms a well-delimited crest that continues dorsally to form the dorsal plate anterior border (dpq, Fig. 8). There is an indistinct stapedial lip (sl, Fig. 8) on the medialmost aspect of the quadrate to accommodate the stapes. The dorsal plate is medially convex, and at the intersection with the lateral condyle there is a noticeable notch posteriorly (qn, quadrate notch), representing the medial and ventral margins of the quadrate foramen. The posterior border of the quadrate forms a distinct rim as the margin of the dorsal plate curls anterolaterally (pqc, posterior quadrate crest). The quadrate notch and posterior quadrate crest (Discrete Character 197 and 198, respectively) are also visible in *K. yajuwayeyi,* but not in *Kawingasaurus* (Laaß 2015).

Quadratojugal

The dorsal portion of the quadratojugal is subrectangular and expands dorsally to fit the anterior aspect of the squamosal, but it tapers ventrally into a crest-like ventral process (vpqj, Fig. 8). The quadratojugal is mostly posteriorly convex and is relatively flat as in *Kawingasaurus* (Laaß 2015), unlike the twisted morphology of *Niassodon* or *K. yajuwayeyi* (Castanhinha et al. 2013, Araújo et al. 2022b; Discrete Character 199). However, the exact shape and dimension of the quadratojugal are hard to appreciate in these specimens (SAM-PK-K6814 and SAM-PK-K011474) because they have several fractures, and the quadratojugal is significantly co-ossified with the squamosal.

Postparietal

Keyser (1965, 1973) had difficulties delineating the suture between the postparietal and the squamosal, but our segmentation elucidates this contact. The postparietal contacts the dorsal process of the squamosal along an interdigitating suture where the postparietal mostly overlaps the squamosal. More dorsally, despite some interdigitation the suture mostly becomes a scarf joint. The lateral alar regions (lapp, lateral alae of the postparietal) are difficult to delineate due to preservation, but seem to be subtrapezoidal. There is no evidence for the tabulars, which is important because there has been uncertainty about their presence in *Cistecephalus* (Angielczyk et al. 2019). Maybe due to preservation, SAM-PK-K6814 does not have a nuchal crest, although this structure was mentioned by Keyser (1965, 1973): "On the ventral border of the interparietals along the suture between them, a ridge overlapping the supraoccipital is formed". SAM-PK-K1187 does have a nuchal crest, but it is more strongly developed on the supraoccipital, with a low swelling continuing onto the ventral process of the postparietal; most of the postparietal is smooth, lacking a crest completely. Notably, in SAM-PK-K6814, the postparietal overlaps the supraoccipital posteriorly with a short ventral flange (vfpp, ventral flange of the postparietal). Unlike *Kembawacela* spp. (Angielczyk et al. 2019, Araújo et al. 2022b), there are no paired ellipsoidal foramina between the suture of the postparietal and the supraoccipital.

Given the overall excellent preservation of the specimen, it is possible to describe the anterior surface of the postparietal. This face presents a central subtriangular tuberosity (astpp, anterior subtriangular tuberosity of the postparietal) that is trapezoidal with flat lateral surfaces and a slightly concave dorsal surface. Ventrally, the tuberosity slots into a groove on the dorsal surface of the supraoccipital. Except for the tuberosity, the anterior surface of the postparietal is smooth and concave.

Supraoccipital

Given the complexity of this bone, especially its anterior aspect, various details were not described by Keyser (1965, 1973) that we expand on here. Each side of the dorsolateral borders of the supraoccipital are concave, forming two conspicuous lateral alae, which resembles the condition in *Kawingasaurus* (Macungo et al. 2022). However, these lateral alae are thin and do not possess the dorsal crests of the supraoccipital alae seen in *Kawingasaurus*. There is no evidence of a nuchal crest on the supraoccipital in SAM-PK-K6814, unlike for other specimens. The anterior surface of the supraoccipital is, as usual, where most of the anatomical information is contained. There are no supraoccipital transverse crests as in *K. yajuwayeyi* (Discrete Character 200), but the supraoccipitalprootic coronal crest is present (spcc, Fig. 8). Posterior to the latter structure is the prootic-supraoccipital recess, which forms a ventrally-descending excavation. However, the supraoccipital-opisthotic lateral recess (slr, Fig. 8) is shallow when compared to that of *K. yajuwayeyi* (Araújo et al. 2022b). The supraoccipital anterior processes (sap, Fig. 8) of the median lobe are somewhat triangular in lateral view, slightly converge dorsally, and become thinner anteriorly. The anteroventral corner of the anterior process is more prominent than the remaining anterior border, which is gently anteriorly convex. The floccular fossa is hemispherical but shallower when compared to other taxa, such as *Niassodon* or *K. yajuwayeyi* (Castanhinha et al. 2013, Araújo et al. 2022b). The posterior half of the floccular fossa is formed by the supraoccipital, whereas the anterior half is formed by the prootic, a common feature among emydopoids (Macungo et al. 2022).

Exoccipital

The exoccipital condyles (ec, Fig. 8), which form the dorsolateral portions of the occipital condyle, are reniform with the convexity oriented laterally. The thin pedicle (pe, Fig. 8) linking the occipital portion of the exoccipital and the exoccipital condyle is angled approximately 70° with the horizontal plane, and contrasts with the robust pedicle in *Myosaurus* and *Pristerodon* (Macungo et al. 2022). The exoccipital contribution to the occipital plate is subtriangular in posterior view, most similar to the condition in *K. yajuwayeyi* (Araújo et al. 2022b), and clearly different from the subrectangular morphology in *Myosaurus* (Macungo et al. 2022). The dorsal contact with the supraoccipital is oval. The exoccipital descending crest is most prominent ventrally (eocr, Fig. 8) and obliquely oriented at an angle of approximately 45° relative to the sagittal axis. A similar crest is also present in *Kawingasaurus* and *Myosaurus*, but absent in *Pristerodon*, whose exoccipital dorsal component is poorly developed (Macungo et al. 2022). This crest forms the dorsal border of the jugular foramen. The anterior contact with the basioccipital is subtriangular with rounded edges and with the apex

pointing ventrally.

Opisthotic

Although the opisthotic and prootic are co-ossified, we were able to separate them through segmentation. This was possible because the two distinct ossification centers produced different internal trabeculae orientations, enabling us to distinguish and separate the bones. The posterior surface of the opisthotic is flat and does not possess the opisthotic posterior crests and opisthotic posterior depression seen in *K. yajuwayeyi* (Macungo et al. 2022). The 'tympanic process' (tp, *sensu* Cox, 1959) points posteroventrally and it is marked by a lateral crest resulting from the squamosal contact (lsqopc, lateral squamosal-opisthotic crest) and a faint crest that follows the ventral border of the opisthotic (vcop, ventral crest of the opisthotic, Fig. 8). The anterolateral surface of the opisthotic is broadly concave forming the articular facet for the quadrate (oafq, opisthotic articular facet). The anteromedial region of the opisthotic hosts part of the vestibule. Keyser (1973) referred to this structure as the "sacculo-cochlear recess", but we avoid using this term because neither the saccule nor the cochlea are identifiable structures within the vestibule, and this region contains other structures such as the utriculus. Instead we refer to this region as the vestibular recess (ver, Fig. 8, for the concavity in the bone) or vestibule (for the void formed by the bony concavity). The ventromedial process of the opisthotic (vmp, Fig. 8) is excavated by the lagenar recess. The ventromedial process is subtriangular in cross-section and bears a prominent lateral crest (lcvmp, lateral crest of the opisthotic ventromedial process). The ventromedial process has variable morphology among kistecephalians: it may be absent in *Kawingasaurus* or subquadrangular in posterior view as in *Myosaurus* (Macungo et al. 2022). In *Cistecephalus*, the ventromedial process is semilunate in posterior view. Such variation seems to have taxonomic relevance.

Keyser (1965, 1973) referred to the small anteroventral process in the lateralmost region of the opisthotic as the quadrate process, which is poorly developed to absent in cistecephalids (Macungo et al. 2022). According to Keyser (1965, 1973), the 'mastoid process' is the region that contacts the squamosal. However, not only is the homology of this structure with the mastoid process of mammals is difficult to verify; the contact occurs mostly in the lateral region and it is unlikely that the process served for the attachment of the atlantoccipital musculature in *Cistecephalus*. Therefore, we prefer to designate the entire descending region of the opisthotic as the lateral vertical buttress (lvb, Fig. 8) following Macungo et al. (2022).

Prootic

The prootic is composed by the main body (prmb, prootic main body, Fig. 8), which includes the alar process (prap, prootic alar process, Fig. 8), and the anterior ascending ramus (praar, prootic anterior ascending ramus, Fig. 8), which includes the pila antotica (pa, Fig. 8). The anteroventral process of Keyser (1965, 1973) is the same as the anterior ascending ramus in Macungo et al. (2022), whereas the anterodorsal process (Olson 1944, Keyser 1965, 1973) corresponds to the dorsal process of the prootic alae in Macungo et al. (2022). There is no sign of the prootic sinus described by Laaß & Kaestner (2017), nor the pila antotica ellipsoidal depression, nor the prootic anterior bulge seen in *Kawingasaurus* (Macungo et al. 2022). The prootic main body is sickle-shaped, with the alar process being blunt dorsally, and the contact with the opisthotic-supraoccipital is formed by a smooth, well-delineated, posteriorly-convex border. The general shape of the prootic main body, surprisingly, more closely resembles the condition in *Pristerodon* and *Diictodon*, rather than the more quadrilateral shape of *Myosaurus* or *Kawingasaurus,* or the subtriangular shape of *Niassodon* and *K. yajuwayeyi* (Castanhinha et al. 2013, Macungo et al. 2022, Araújo et al. 2022b, Supplemental Information). The pila antotica is short and blunt, and devoid of the anterodorsally-directed ridges and corresponding median excavation present in *Kawingasaurus* (Macungo et al. 2022). An interesting anatomical region where there seems to be considerable variation is the supraoccipital lateral recess and the corresponding supraoocipital-prootic coronal crest (Macungo et al. 2022, Araújo et al. 2022b). The supraoocipital-prootic coronal crest is noticeably pronounced and smoothly posteriorly convex, with a uniformly wide supraoccipital lateral recess in *Niassodon* (Castanhinha et al. 2013). A uniformly wide supraoccipital lateral recess is also present in *Pristerodon*, but with a low supraoocipital-prootic coronal crest (Macungo et al. 2022). However, in *Cistecephalus* the supraoocipital-prootic coronal crest is low and fades ventrally onto the main body of the prootic, whereas the supraoccipital lateral recess is significantly wider ventrally than dorsally, as in *K. yajuwayeyi* and *Kawingasaurus* (Macungo et al. 2022,

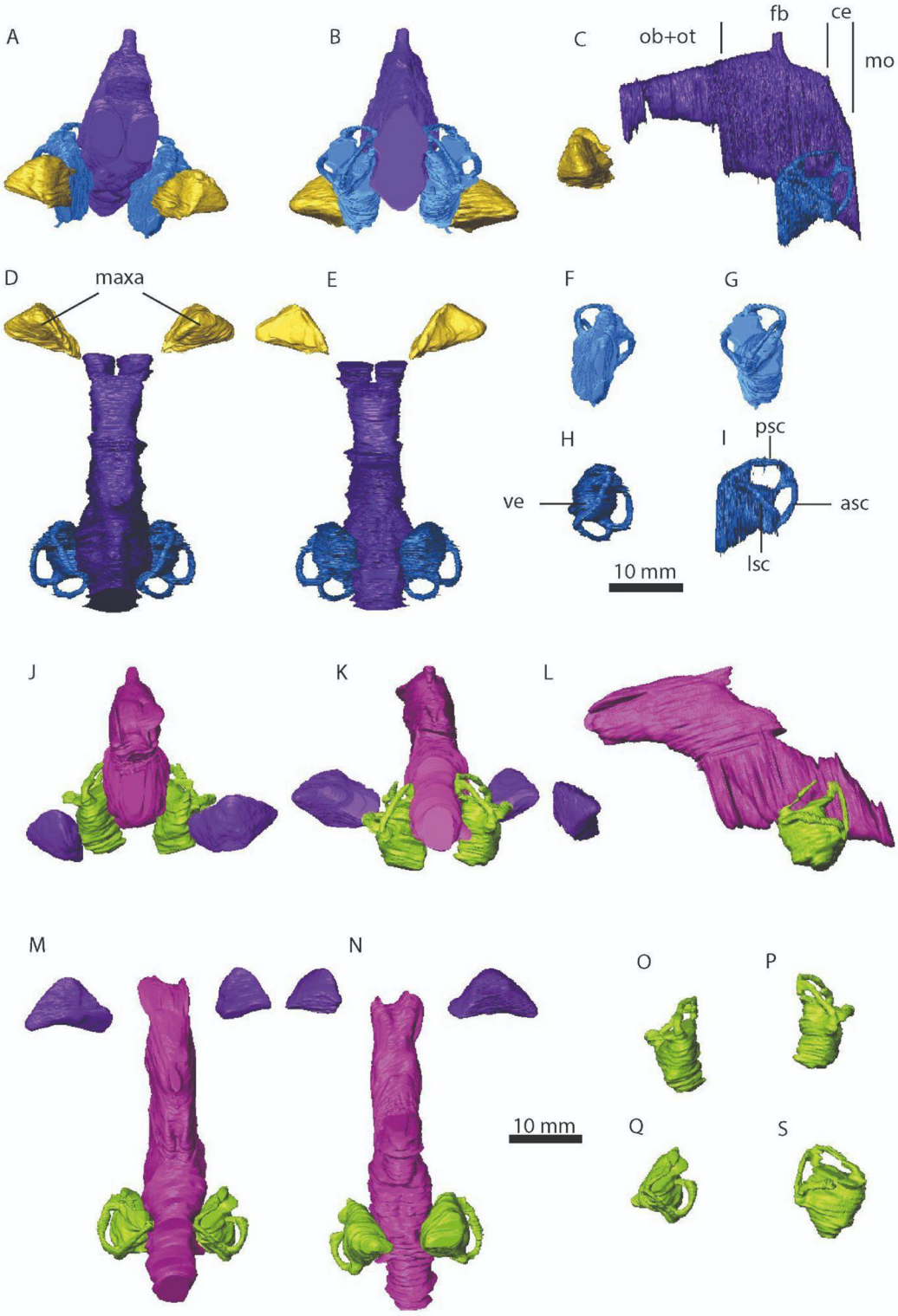

FIGURE 10. Endocasts of SAM-PK-K6814 and SAM-PK-K011474. A, anterior view, B, posterior view, C, lateral view, D, dorsal view, E, ventral of SAM-PK-K6814 endocasts. E, ventral view, G, posterior view, H, dorsal and, I, lateral view of SAM-PK-K6814 endosseous labyrinth endocasts. J, anterior view, K, posterior view, L, lateral view, M, dorsal view, N, ventral of SAM-PK-K011474 endocasts. O, ventral view, P, posterior view, Q, dorsal and, R, lateral view of SAM-PK-K011474 endosseous labyrinth endocasts. Abbreviations: ob+ot, olfactory bulbs and olfactory tracts; fb, forebrain; ce, cerebellum; mo, edulla oblongata; maxa, maxillary antrum; ve, vestibulum; psc, posterior semicircular canal; asc, anterior semicircular canal; lsc, lateral semicircular canal.

Araújo et al. 2022b).

Endosseous labyrinth

The prootic envelops the anterior halves of the anterior and lateral semicircular canals, the opisthotic envelops the posterior half of the lateral semicircular canal and the ventral half of the posterior semicircular canal, and the supraoccipital envelops the dorsal portion of the anterior and posterior semicircular canal. The dorsal component of the exoccipital also contributes to form the medial enclosure of the posterior semicircular canal. This arrangement is similar to what has been reported for the pylaecephalid *Diictodon* and the emydopoids *Myosaurus* and *Kawingasaurus*, but the exoccipital of *Pristerodon* is not pierced by the bony labyrinth (Macungo et al. 2022, see Supplementary Information). The bony enclosure for the endosseous labyrinth is also different in *Niassodon* (Castanhinha et al. 2013), in which the posterior semicircular canal is entirely enveloped by the supraoccipital, the opisthotic only envelops the posterior half of the semicircular canal, and the exoccipital does not contribute to the endosseous labyrinth. Whether this anatomical arrangement has phylogenetic significance needs to be confirmed in other endothiodontid and eumantelliid dicynodonts. However, given the high degree of fusion between the occipital and braincase bones in *Niassodon* and the lack of anatomical information about this region at the time *Niassodon* was described, uncertainty exist about the accuracy of some of those sutures presented in Castanhinha et al. (2013).

All three semicircular canals are ellipsoidal (Fig. 10), as is typical in non-mammaliaform synapsids (Araújo et al. 2022b). Among the three canals, the lateral is the thickest in cross section, followed by the posterior semicircular canal. The crus communis is short and opens dorsally in a triangular fashion as the vertical semicircular canals diverge, somewhat resembling the condition in *Endothiodon* cf. *bathystoma* (Araújo et al. 2018). There are no visible vertical semicircular canal ampullae, as in *Endothiodon* and *Niassodon* (Castanhinha et al. 2013, Araújo et al. 2018). The ampulla for the lateral semicircular canal is slightly developed, contrasting with that of *Kawingasaurus*, *Emydops* and *Eodicynodon* which are well-delimited (Araújo et al. 2022b).

In *Cistecephalus*, the lateral enclosure of the vestibule is formed by the ventromedial process of the opisthotic, whereas it is the prootic and the basioccipital that form the anterior and medial wall, respectively. In *Niassodon* and *Diictodon* the basisphenoid and the basipostsphenoid form the anterior and posterior walls of the lagena, respectively (Castanhinha et al. 2013, see Supplementary Information). The vestibule is subtriangular and not as inflated as those observed in *Kawingasaurus* and *K. yajuwayeyi* (Araújo et al. 2022b).

Brain endocast

The *Cistecephalus* brain endocast in both specimens (SAM-PK-K6814 Fig. 10 and SAM-PK-K011474 Fig. 10) is remarkably similar to other cistecephalid endocasts and distinct from other dicynodonts, following the pattern mentioned in Araújo et al. (2022b). Specifically, the forebrain and cerebellum are significantly shortened, and the post-olfactory tract brain section is dorsoventrally bulky. The extreme modifications of the brain endocast anatomy cannot be solely explained by verticalization of the occipital plate seen in cistecephalids because there are other dicynodonts in which the occiput does not slope forward very strongly, and yet do not have such brain endocast organization (e.g., *Lystrosaurus*). Cistecephalids seem to have undergone an additional, substantial posterior telescoping of the skull that is presumably related to broadening the back of the skull and more closely aligning the posterior part of the temporal fenestra with the occipital plate. Other dicynodonts (e.g., *Compsodon*, *Oudenodon*, *Geikia*) have more emarginated temporal fenestrae that extend posteriorly beyond the plane of the occipital plate. The location of the pineal foramen can be used as a landmark for recognizing this telescoping: typically it is located towards the middle of the intertemporal bar, whereas in cistecephalids it is very close to the posterior edge of the intertemporal bar (e.g., *Cistecephalus*) or right at the posterior edge of the intertemporal bar (e.g., *Kembawacela* spp., *Cistecephaloides*). Therefore, cistecephalids appear to have reorganized the portion of the skull roof that is typically posterior to the pineal foramen. There are other non-cistecephalid dicynodonts that have their pineal foramen located posteriorly on the skull roof (e.g., *Niassodon*), but in those cases it is never as far posteriorly as in cistecephalids, and the occipital plate often has some anterior angulation that helps to accommodate a more typical, elongated dicynodont brain endocast (Laaß et al. 2010, Castanhinha et al. 2013, Simão-Oliveira et al. 2020). In sum, cistecephalids were not only making their occipital plate more vertical, they also reorganized the entire post-pineal portion of the skull anteriorly,

requiring a compact brain to accommodate these changes.

The frontal covers the dorsal surface of the olfactory tract and bulbs, whereas the parietal covers the dorsal surface of the forebrain including the epiphyseal nerve endocast, and the supraoccipital covers the dorsal surface of the cerebellum and the inception of the medulla oblongata, similar to the the condition in *K. yajuwayeyi* (Araújo et al. 2022b). The ventral and lateral aspects of the olfactory tract and bulbs are bounded by the orbitosphenoid. The ventrolateral aspect is bounded by the prootic, whereas the ventral aspect by the basisphenoid anteriorly and the basicoccipital posteriorly.

The anterior region of the brain endocast is not especially expanded laterally compared to the posterior region, despite the latter being more enlarged in this dimension. The floccular process is reduced and barely perforates the anterior semicircular canal. The epiphyseal nerve is developed into a relatively long, straight, vertical cylinder that reaches the skull roof at nearly mid-length of the forebrain. The olfactory tracts and bulbs are separated by a median septum of the mesethmoid, which unlike other cistecephalid specimens (Laaß & Kaestner 2017, Araújo et al. 2022b), physically divides the two tracts. Interestingly, the olfactory tracts in cistecephalids (Laaß & Kaestner 2017, Araújo et al. 2022b) seem to be dorsoventrally taller than in other dicynodonts (Laaß 2010, Castanhinha et al. 2013, Simão-Oliveira et al. 2020). The brain endocast of SAM-PK-6814 brain has a volume of ~2340 mm^3 including the olfactory bulbs, and ~1030 mm^3 without the olfactory bulbs, measured using Amira software.

Maxillary antrum and lacrimal gland endocast

The maxillary antrum is enveloped by the maxilla anteriorly, the jugal laterally, and the lacrimal posteriorly. A small portion of the medialmost aspect of the maxillary antrum is enveloped by the palatine. The anatomy and variation of the maxillary antrum rarely has been described in dicynodonts. Therefore, we give further detail to begin building a database that could be useful for future taxonomic studies. Contrary to *K. yajuwayeyi* (Araújo et al. 2022b), there is no separation between the maxillary antrum and the lacrimal gland endocast, resulting in a single structure. The maxillary antrum can be described as an isosceles triangle pyramid (Fig. 10). The base of the triangle forming the ventral face of the pyramid is on the posterior side, which forms an angle with the lateral face of ~50°, and ~65° with the medial face in SAM-PK-1174 (in SAM-PK-K6814 ~47° and ~42°, respectively). The angle between the lateral and medial face is ~85°, despite being significantly more rounded in SAM-PK-1174 (in SAM-PK-K6814 is ~89)° . Whereas the lateral aspect of the maxillary antrum tapers into a point, the medial aspect forms an edge. The intraspecific variation of this structure is negligible, except for the angle between the lateral posterior and lateral edge of the ventral face of the maxillary antrum, despite there being taphonomic preservation differences between specimens (i.e., SAM-PK-1174 vs. SAM-PK-6814). This suggests that the maxillary antrum may have utility for taxonomic purposes.

DISCUSSION

Semicircular canal biomechanics and cistecephalid ectothermy

A recent paper hypothesized that endothermy could have evolved in cistecephalids, independently from its evolution along the mammalian lineage (Laaß & Kaestner 2023). These results are mainly based on data from *Kawingasaurus*, and seemingly contradict results obtained from the analysis of the semicircular canals of this species, which had a probability for endothermy of 27% (Araújo et al. 2022a). They also contradict results obtained in the present study, where we found an endothermy probability of 23-40% for cistecephalids, and interpret them as most likely ectotherms. Laaß & Kaestner (2023) asked "whether the approach of Araújo et al. (2022a) can be applied to *Kawingasaurus* and other burrowing dicynodonts to infer their metabolic status." They argued that *Kawingasaurus* was fossorial, and like other fossorial species, has semicircular canal planes deviating from an ideal configuration (i.e., orthogonal semicircular canals), illustrated by an angle of 53° they measured between the anterior and lateral canals (Laaß 2015). Furthermore, they explained that "the sense of balance is less important for burrowers, due to the restricted head rotations and the decreased requirements for motor coordination underground", and that "such behaviour requires less sensitivity of the semicircular canals (Berlin et al. 2013), which might be an indication of a degenerated sense of balance".

There are several issues with these claims. First, fossorial mammals do not have a diminished sense of balance. On the contrary, studies on the biomechanics of the membranous semicircular ducts of *Cryptomys*, *Spalax* and *Talpa* showed

that, when compared to *Rattus* and after body mass correction, the three fossorial species showed increased semicircular duct sensitivity (Lindenlaub et al. 1995, McVean 1999), not decreased semicircular duct sensitivity (*contra* Berlin et al. 2013). This is particularly true of the lateral semicircular ducts, and was interpreted as providing improved sensory cues for navigation, which depends on semicircular duct function (Fitzpatrick et al. 2006).

Second, classical anatomical measurements of semicircular canal planes are generally based on the slender portion of the canals and omit the utricular part of the streamline trajectory. This is likely what happened with the measurement of the angle between the anterior and posterior semicircular canals presented for *Kawingasaurus*. Taking the full streamline torus, and applying biomechanical equations for the maximal response plane (Rabbitt et al. 2004), we find an angle of 76° between these two canals, a value that fall within extant amniote variation and that is much closer to the ideal angle of 90° than the 53° reported in Laaß (2015). The same is true for *Cistecephalus*, a closely related cistecephalid, which also shows an angle between anterior and lateral semicircular canals that falls within extant amniote variation. Thus, it is important to note that when one aims to derive functional interpretations, maximal response planes are the only relevant planes to be compared to an "optimal" configuration (Rabbitt et al. 2004).

Third, it should be stressed that the thermo-motility index is based on two main terms derived from anterior semicircular canal biomechanics, only one of which, the sensitivity, is affected by the orientation of maximal response planes. In this context, the anterior semicircular canals of *Kawingasaurus* make an angle of 40° with the midsagittal plane, and of 51° with the coronal plane, the two major planes of head motion relevant for these canals. When compared with optimal angles of 45°, it appears that the spatial orientation of the anterior semicircular canals of *Kawingasaurus* are thus fairly normal and fall well within extant amniote variation. The same is true for *Cistecephalus*. Importantly though, even if these angles fell at the edge of extant amniote distribution, this fact would not prevent use of the thermo-motility index to predict the corresponding thermal regime. The reason for this is simple: although canal plane orientation was not taken into account by Araújo et al. (2022a) when developing models correlating the thermo-motility index to body temperature and endothermic regime, the extant vertebrate species used in their study show variation in the spatial orientation of their semicircular canals. Hence, if this variation was large enough to affect the thermo-motility index, it would contribute to its residual variation, which is taken into account when computing 95% confidence intervals on body temperature of fossil species.

Nevertheless, as indicated in Araújo et al. (2022a) and as mentioned in Laaß & Kaestner (2023), the use of the thermo-motility index is indeed less suited to predicting the metabolic status of a single species. Furthermore, while unlikely, unforeseen modifications of some functional parameters (e.g., endolymph viscosity) cannot be ruled out in clades branching off from the main lineage leading to mammals. In this context, the 95% C.I. for the body temperature of cistecephalids, predicted from the thermo-motility Index of three species and taking into account uncertainty linked to uncontrolled parameters, ranges between 24.0-35.4 °C, with 30.5% chance of being higher than 31°C, the lowest body temperature found in extant endotherms.

Fossoriality as a thermoregulatory strategy in *Cistecephalus* and other dicynodonts

Cistecephalus and other cistecephalids are at an extreme point on the spectrum of fossorial anatomical specialization among dicynodonts (Macungo et al. 2022). Features such as skull telescoping (this paper), verticalization of the occipital plate (Araújo et al. 2022b), high nasofrontal suture complexity (Kammerer 2021), development of the atlantoccipital musculature and basicranial co-ossification (this paper, Macungo et al. 2022), compact bone histology (Nasterlack et al. 2012), and robust limb morphology (Cox 1972, Cluver 1978, Lungmus & Angielczyk 2021) provide evidence for an obligate fossorial lifestyle for *Cistecephalus*, despite the lack of direct ichnological evidence (Smith et al. 2021). Living as an obligate fossorial animal is known to provide significant thermoregulatory benefits due to relatively constant temperatures and humidity in burrows, which led to a notable reversal to ectothermy among fossorial mammals such as naked mole-rats (e.g., Buffenstein et al. 1991, Martinez et al. 2023). However, it seems that fossoriality demonstrated by *Cistecephalus* and other cistecephalids has deeper origins among dicynodonts. Various lines of evidence from preserved burrow structures (Smith 1987, King & Cluver, 1991; Bordy et al., 2011; Botha-Brink, 2017; Smith et al., 2021) to postcranial adaptations (Smith, 1987; Sullivan et al., 2002; Ray &

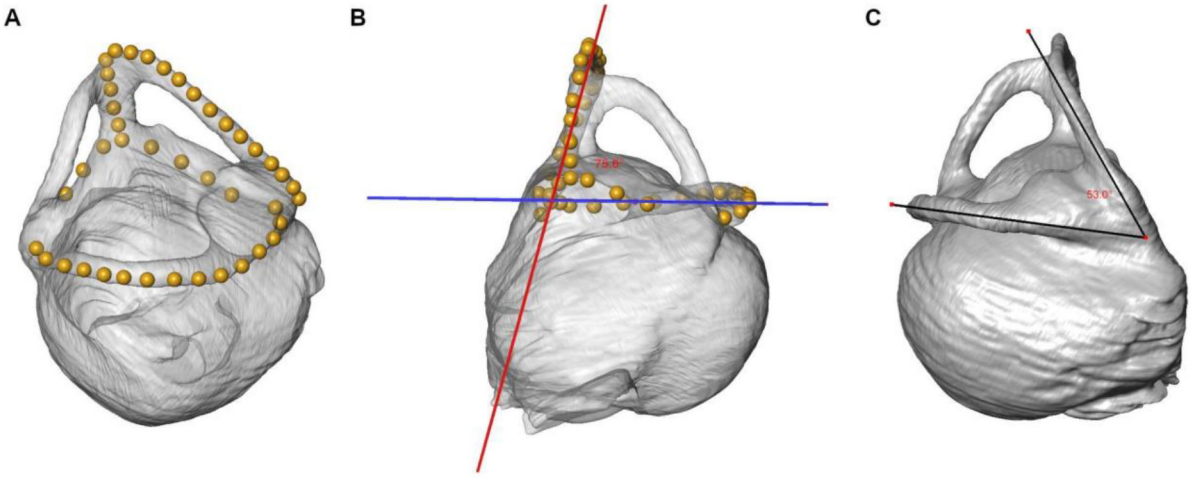

FIGURE 11. Semicircular canal planes of *Kawingasaurus*. A, Landmarks used to compute the functional planes of the anterior and posterior canals. Note that landmarks were placed in the vestibule where the anterior utriculus is supposed to be. B**,** Angle between functional planes of the anterior (red) and lateral (blue) semicircular canals. C, Angle between anatomical planes of the anterior and lateral semicircular canals when measured "classically". Note that the angle obtained using anatomical planes (53^{o}) differs greatly from the angle obtained using functional planes (75.6^{o}).

Chinsamy, 2003; Smith et al., 2022) indicate that non-cistecephalid dicynodonts burrowed to some extent, perhaps to shelter from harsh paleoenvironmental conditions and/or rear young.

To provide a broader context, it is important to consider the paleoecological scenario that cistecephalids and other Permian dicynodonts were experiencing. In particular, it is significant that unlike today, terrestrial tetrapod communities were dominated by ectotherms. Recent evidence indicates that synapsid endothermy likely originated in mammaliamorphs in the early Late Triassic (Araújo et al. 2022a). This finding is supported by other lines of evidence, such as brain enlargement (Benoit et al., 2023) or the evolution of vibrissae (Rowe et al. 2011, Benoit et al. 2016, 2023, Crompton et al. 2017), which seem to also occur at this time. The corollary of this result is that during the Permian all tetrapods were ectothermic, because other purported endothermic clades such as dinosaurs or pterosaurs had not yet originated (Benton et al. 2021). Visualizing a scenario wherein intricate trophic hierarchies exist, involving terrestrial megafauna that are physiologically restricted by ectothermy poses a significant challenge when viewed from the perspective of modern, largely endotherm-dominated ecosystems. Ectotherms have restricted annual and diurnal activity patterns and/or heightened reliance on behavioral thermoregulation for routine daily activities (e.g., Pianka 1986). Thus, ectothermic Permian and Early to Middle Triassic synapsids include top-predators such as gorgonopsians, and megaherbivores like large herbivorous dicynodonts. Following this line of thought, synapsids could not engage in long aerobic terrestrial migrations to escape the harsh Karoo winter in the Permian, similar to most modern terrestrial ectotherms (Southwood & Avens 2010). The cosmopolitan presence of some dicynodont species demonstrates long distance dispersal (e.g., Angielczyk & Sullivan 2008), yet presumably over timescales that were longer than seasonal/yearly. Nevertheless, the middle-late Permian Karoo, given its paleolatitude, is predicted to have been a warm temperate climate (Köppen equivalent: CSa, CSb) according to Boucout et al. (2013), to a boreal/subartic climate (Köppen equivalent: Dfc, Dwc, Dsc, Dfb, Dwb) according to Rees et al. (2002) and Rey et al. 2016), to a cold steppe/cold desert type (Köppen equivalent: BSk, Bwk) according to Roscher et al. (2011). Regardless of the exact Köppen climate type or specimen age range and associated paleolatitude range, the Permian Karoo region would have night and winter temperatures that would be difficult for modern ectotherms to tolerate (Araújo et al. 2022a). For instance, *Clemmys guttata*, *Alligator sinensis* or *Phrynosoma mcalli* start to brumate when environmental temperatures drop ~20^{o}C below their preferential temperature (Yagi & Litzgus 2013, Zhang et al. 2021, Mayhew 1965). Indeed, gorgonopsians and Permian dicynodonts show a probability of >0.7 of brumating during the winter

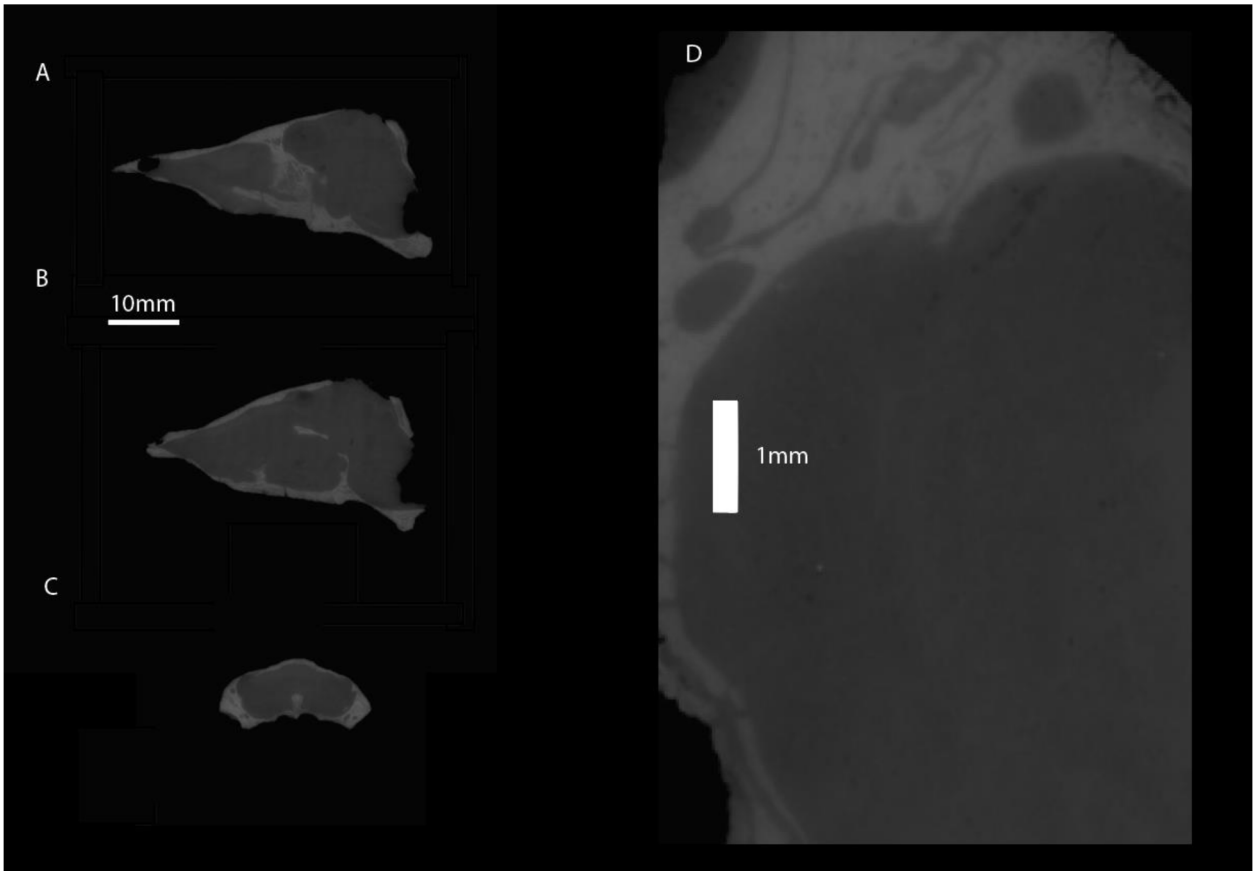

FIGURE 12. Propagation phase-contrast synchrotron micro-tomography sections equivalent to those depicted in Laaß & Kaestner (2023) showing no evidence for turbinals in *Kawingasaurus fossilis* (GPIT-PB-117032). A, midstagittal section, B, sagittal section section left from the midline, C, coronal section at the level of the nasal cavity, D, close-up on C.

and >0.76 of being diurnal (Araújo et al. 2022a). In other words, the hypothesis that gorgonopsians were obligatorily diurnal is derived from their estimated body temperature, taking into account the paleotemperature at their paleolatitude, which is in line with previous studies (Angielczyk & Schmitz 2014). Essentially, drawing upon knowledge from contemporary reptiles, the nights (and the winters) would have been too cold for gorgonopsians and dicynodonts to function effectively, considering their thermo-motility index. The profusion of burrow structures discovered within the Permian Karoo ecosystems (Smith et al. 2021), provides compelling evidence supporting the imperative requirement for shelter during the winter period while undergoing brumation. This would result in a stark winter landscape in the Karoo during the middle-late Permian. During the hot seasons, synapsids would be expected to resort to intermittent locomotion (Kramer & McLaughlin 2001) like modern lizards, and/or long periods of rest and behavioral thermoregulation punctuated by short periods of activity (Hertz et al. 1988). Consequently, diurnal gorgonopsians (P = 0.7, P refers to probability) and, potentially diurnal Permian therocephalians (P = 0.63), likely were ambush predators using cryptic camouflage, or would pursue prey for short anaerobic bursts, like terrestrial tetrapod ectotherms do today (Hertz et al. 1988). Middle-late Permian dicynodonts are predicted to brumate during the winter and to also be diurnal (P = 0.8, P = 0.79, respectively), and the sampled cistecephalids are no exception (*Kawingasaurus,* diurnal P = 0.79, winter brumation, P = 0.77; *Kembawacela kitchingi*, diurnal P = 0.92, winter brumation P = 0.84), irrespective of their fossorial status.

Turbinates and thermoregulation

Despite the exceptional preservation of the *Cistecephalus* specimens studied here, none presented structures resembling turbinals or evidence of ridges where they could attach if cartilaginous. Recent developments in understanding the

function, anatomy and physiology of turbinates seem to be progressively dismantling their relationship with the origin and evolution of endothermy. Martinez et al. (2023) found no relationship between the relative surface area of the maxilloturbinal and the corrected basal metabolic rate, body temperature, or the different forms of torpor (short- or long-term torpor) for >300 mammalian species. Furthermore, for >100 species from Martinez et al. (2020, 2023), they demonstrated an absence of trade-off between the size-corrected surface area of the maxillo- and the nasoturbinal, suggesting that their results on the maxilloturbinal may be correctly extended to the mammalian respiratory turbinals. These results are particularly relevant in the context of synapsid evolution because complex turbinals have been proposed as a hallmark for endothermy (e.g., Hillenius 1992, 1994, Ruben et al. 2012, Owerkowicz et al. 2015) and subsequently claimed as evidence of endothermy in some non-mammaliamorph synapsid species (Hillenius 1994, Laaß et al. 2010, Laaß & Kaestner 2023). However, Martinez et al. (2023) seriously questions the role of turbinals for body temperature regulation because regardless of the complexity of maxilloturbinals, there is no effect on thermal biology. For instance, the rodents *Psammomys obesus* and *Massoutiera mzabi* have some of the lowest maxilloturbinal relative surface areas, whereas other rodents such as *Blarinomys breviceps* have high relative surface areas. Perhaps surprisingly, the platypus, which is among the mammals with lowest body temperatures, has some of the highest maxilloturbinal surface areas. Indeed, the simplicity of the turbinals in multiple endothermic mammals parallels that of ectothermic diapsids (Bourke & Witmer 2023). Furthermore, it was found that airflow patterns are very similar irrespective of turbinal complexity and thermal regime (Bourke & Witmer 2023). Importantly, the authors found that soft-tissue reconstruction of the nasal cavity is crucial for assessing airflow patterns, because simple cartilaginous turbinals have similar overall effects when compared to more complex and ossified turbinals (Bourke & Witmer 2023). It is thus reasonable to hypothesize that the known thermoregulatory and moisture conservation effects of turbinals (e.g., Schmidt-Nielsen et al. 1970) are by-products of the turbinal anatomy, a structure primarily serving for olfaction. Indeed, it has been proposed that turbinals can be modeled after a gas chromatograph (Mozell 1970, Schoenfeld & Cleland 2005), in which odorants are heterogeneously distributed through the turbinals olfactory epithelia during respiration. To conclude, reported structures such as those observed in *Kawingasarus* (Laaß & Kaestner 2023) likely are not be indicative of endothermy in cistecephalids and probably represent lines left by sediment infilling of the skull cavity (Fig. 12, Fernandez et al. 2013). We could not replicate the observations of the presence of turbinals based on a 27µm-voxel propagation phase-contrast scan of the same specimen of *Kawingasaurus fossilis*.

Evolution of the postorbital-postfrontal complex in dicynodonts

Postfrontal bones are ancestrally present in anomodonts, as evidenced by their ubiquity among non-dicynodont anomodonts for which the relevant region of the skull is preserved (e.g., Brinkman 1981; Ivakhnenko 1996; Rubidge and Hopson 1996; Rybczynski 2000; Liu et al. 2010; Cisneros et al. 2015). Among dicynodonts, the postfrontal (when present) usually is a relatively small, wedge-shaped element that is sandwiched between the frontal and postorbital and contributes to the posterior margin of the orbit. The postfrontal has been lost in a number of dicynodont taxa, and the presence or absence of postfrontals has been used frequently as a character in phylogenetic analyses of dicynodonts (e.g., Maisch 2001, 2002; Maisch and Gebauer 2005; Angielczyk 2007; Fröbisch 2007; Kammerer et al. 2011 and the many subsequent derivatives of that dataset). However, patterns of variation in the presence or absence of this element are more complex than they might first appear, and there are inconsistencies in the literature concerning which taxa lack the postfrontal. For example, Broili and Schröder (1936) and Angielczyk (2007) tentatively reported the presence of postfrontals in *Endothiodon*, whereas Cox (1964), Ray (2000), and Cox and Angielczyk (2015) stated that they were absent; Macungo et al. (2020) did not note their presence in the specimens from Mozambique that they studied. Similarly, Cluver and King (1983) reported that postfrontals were absent in *Rhachiocephalus*, but Keyser (1975), Maisch, (2000), and Angielczyk (2002) stated that they were present in that taxon. There is also evidence of ontogenetic variation in the presence of the element (Kammerer and Smith 2017; Olroyd et al. 2018, Kammerer et al., 2022), and some taxa, especially some Permian basal dicynodontoids, reduce the exposure of the element on the skull roof to a thin strip but retain it as a distinct element seemingly throughout ontogeny (e.g., Kammerer et al. 2011). Of particular relevance to the current paper is the fact that

loss of the postfrontal is widespread among emydopoids. Stemward taxa such as *Emydops* and *Compsodon* retain a postfrontal (Fröbisch and Reisz 2007; Angielczyk and Kammerer 2017), but it is absent in kistecephalians, including all kingoriids (Cox 1959; Fröbisch 2007; Fröbisch et al. 2010; Kammerer 2019) and cistecephalids described to date (Broili and Schröder 1935; Brink 1950; Cox 1972; Keyser 1973; Cluver 1974a; Kammerer et al. 2016; Angielczyk et al. 2019; Araújo et al. 2022b) (also see Cluver 1974b; Kammerer et al. 2015).

Despite being a widespread phenomenon in dicynodonts, the mechanism by which the loss of the postfrontal occurs has received little attention. Passing comments in the literature regarding ontogenetic variation in the presence of the element suggest that at least in some cases its loss stems from fusion of the postfrontal with the postorbital during ontogeny, as opposed to the complete loss of a postfrontal ossification center (Kammerer and Smith 2017; Olroyd et al. 2018). Olroyd et al. (2018) hypothesized that this fusion begins near the dorsal surface of the skull and proceeds ventrally. We examined micro-computed tomography data for a selection of dicynodont taxa to provide a preliminary test of the hypotheses that loss of the postfrontal in dicynodonts typically occurs via fusion of the element with the postorbital, and whether this process begins near the dorsal surface of the skull.

Although it falls in a somewhat nested phylogenetic position, within the dicynodont clade Bidentalia, a specimen of the Permian cryptodont *Oudenodon bainii* from the Luangwa Basin, Zambia (NHCC LB631) provides a useful starting point for comparison as it retains a relatively broad exposure of the postfrontal on the dorsal surface of the skull roof (Fig. 13A). Near its anterior edge, at the posterior margin of the orbit, the postfrontal of *Oudenodon* is relatively wide on the skull roof, and a transverse section through the skull at this level shows that the bone is of a fairly uniform mediolateral width throughout its thickness. Moving posteriorly, the exposure of the postfrontal on the skull roof narrows, but a transverse section near the mid-width of the postorbital bar reveals that the rate of narrowing is not uniform throughout the thickness of the bone. Instead, the dorsal edge of the element narrows more rapidly than the more ventral portions of the bone, giving the postfrontal a greater width within the thickness of the skull roof than on its dorsal surface. Posterior to the level of the postorbital bar, the postfrontal returns to having a more consistent width throughout the thickness of the skull roof, but it takes on a complex sigmoid shape in transverse section to interdigitate with the frontal and the temporal portion of the postorbital. Sutures between the postfrontal, the frontal, and the postorbital are generally consistent in their visibility from the dorsal surface to the ventral surface of the skull roof, suggesting that no fusion of the elements was taking place.

Two other bidentalians that have reduced the exposure of the postfrontal on the skull roof to a narrow strip appear to have done so in a manner resembling the anterior-posterior trend observed in *Oudenodon*. NHCC LB736 consists of the anterior portion of a skull of the geikiid *Aulacephalodon* sp. from the Luangwa Basin that was naturally broken near the level of the postorbital bar, exposing a transverse section of the skull roof in this region (Fig. 13B). The dorsal exposure of the postfrontal in this specimen is extremely narrow. At the posterior margin of the orbit, the postfrontal makes a small, triangular contribution of the orbital rim, but moving posteriorly very little of the postfrontal is visible. Near the mid-width of the postorbital bar, parts of the postfrontal are visible within the thickness of the postorbital–frontal suture, but near the posterior edge of the postorbital bar there is no exposure of the postfrontal visible. However, the broken surface shows that the internal extent of the postfrontal is quite large. Its dorsal surface curves laterally and is extensively overlapped by the frontal, such that only a narrow bit of the bone actually reaches the dorsal surface of the skull roof. As with the *Oudenodon* specimen, the internal sutures bounding the postfrontal are well-marked throughout the thickness of the skull roof, suggesting that fusion was not actively occurring despite the highly reduced exposure of the element on the skull roof.

NHCC LB37 represents a new, undescribed Permian lystrosaurid from the Luangwa Basin whose dorsal exposure of the postfrontal also consists of a narrow strip between the postorbital and frontal (Fig. 13C). Anteriorly, the postfrontal is visible on the anterior surface of the postorbital bar, but it has an extremely narrow exposure on the dorsal surface of the skull roof. A transverse section at this level shows that the postfrontal is broad ventrally, but is extensively overlapped by the postorbital laterally and the frontal medially. A thin triangular process extends dorsally from the approximate midpoint of the postfrontal, but only the narrow apex of this process reaches the skull roof. Closer to the mid-width of the

postorbital bar, the postfrontal is narrower and of a more consistent width across its height. However, its medial surface angles laterally and is overlapped by the frontal, resulting in a narrow exposure on the skull roof. Posterior to the level of the postorbital bar, the postfrontal takes on a more triangular shape in transverse section, with its widest portion dorsally. Its lateral and medial margins in this area are relatively straight, and it does not extend through the whole thickness of the skull roof. The sutures between the postfrontal, the frontal, and the postorbital are well marked throughout the thickness of skull roof. Therefore, areas on the skull roof where the postfrontal is difficult to discern stem more from overgrowth of the bone by the frontal and/or postorbital instead of the obliteration of the sutures separating the elements. The margins of the bone also are straight posteriorly, indicating that it did not interdigitate with the postorbital and the frontal to the degree seen in *Oudenodon.*

As noted above, Olroyd et al. (2018) stated that a distinct postfrontal was visible in some specimens of the Permian basal endothiodont *Abajudon kaayai*, and μCT data are available for one of the specimens that possesses the element (NHCC LB314) from the Mid-Zambezi Basin of Zambia (Fig. 13D). These data facilitate a test of Olroyd et al.'s (2018) hypothesis that the postfrontal began to fuse with the postorbital near the dorsal surface of the skull, and with the bidentalian data described above they provide a useful phylogenetic bracket for members of Emydopoidea that lack a postfrontal. The morphology of the postfrontal on the skull roof of *Abajudon* generally resembles that of *Oudenodon*, consisting of a wider section near the posterior margin of the orbit that then narrows posteriorly. A transverse section through the skull roof at this level also reveals a generally similar internal anatomy, although the postfrontal of *Abajudon* extends farther medially and underplates the frontal more extensively than in *Oudenodon*. Moving posteriorly, to near the mid-width of the postorbital bar, the exposure of the postfrontal on the skull roof is narrower, and its dorsal margin takes on a stepped appearance internally. Medially, a vertical process of the postfrontal extends between the frontal and postorbital to reach the external surface of the skull roof, but laterally the dorsal surface of the postfrontal is horizontal and extensively overlapped by the postorbital. The ventral exposure of the element remains quite wide at this level. Farther posteriorly, near the posterior margin of the postorbital bar, the postfrontal becomes very narrow and takes on a triangular shape (apex oriented ventrally) in transverse section. As a result, the dorsal exposure of the element is its widest portion at this level, and its lateral and medial margins are straight, indicating that it did not interdigitate with the frontal and postorbital. The sutures bounding the postfrontal generally are well-marked throughout the skull roof. Near the dorsal margin of the skull, the sutures are sometimes slightly fainter than is the case farther ventrally, but it is somewhat uncertain if this is a real feature because the effect is subtle and inconsistent from slice to slice in the μCT image stack.

Taken together, the specimens that we examined that phylogenetically bracket Emydopoidea suggest that the reduction of the size of this element on the skull roof in these taxa is largely achieved by increasing the degree to which the postorbital and/or the frontal overlap the postfrontal dorsally, such that the dorsal exposure is narrow but the internal size of the element remains large, especially in the vicinity of the orbit and the postorbital bar. There is limited evidence that fusion of the the postorbital proceeds from dorsal to ventral in *Abajudon*, as suggested by Olroyd et al. (2018), but more investigation is needed to confirm that this is the case.

The situation is quite different in the emydopoids we considered that lack external evidence of a postfrontal. For example, in a specimen of *Dicynodontoides* sp. (NHCC LB117; Fig. 13E) and the holotype of *Kembawacela kitchingi* (NHCC LB18; Fig. 13F), both from the Luangwa Basin, there is no evidence internally of a discrete postfrontal. Instead, the suture between the postorbital and the frontal is well-marked, but no sutures delimiting a postfrontal are visible, and there are also no obvious discontinuities in the internal structure of the postorbital that would suggest the location of a postfrontal early in ontogeny. The *Dicynodontoides* specimen is especially interesting because the portion of the postorbital near the posteromedial margin of the orbit (i.e., the area that would be occupied ancestrally by the postfrontal) has an external appearance that strongly resembles the shape of the postfrontal of taxa in which the element is present. Based on this appearance, it is very easy to imagine a distinct postfrontal ossification being present initially in ontogeny that later fused with the postorbital while retaining its basic shape. However, if this did occur in NHCC LB117, it happened at a sufficiently early stage in ontogeny that all evidence of the sutures bounding the postfrontal were obliterated, and the internal structure of the resulting single

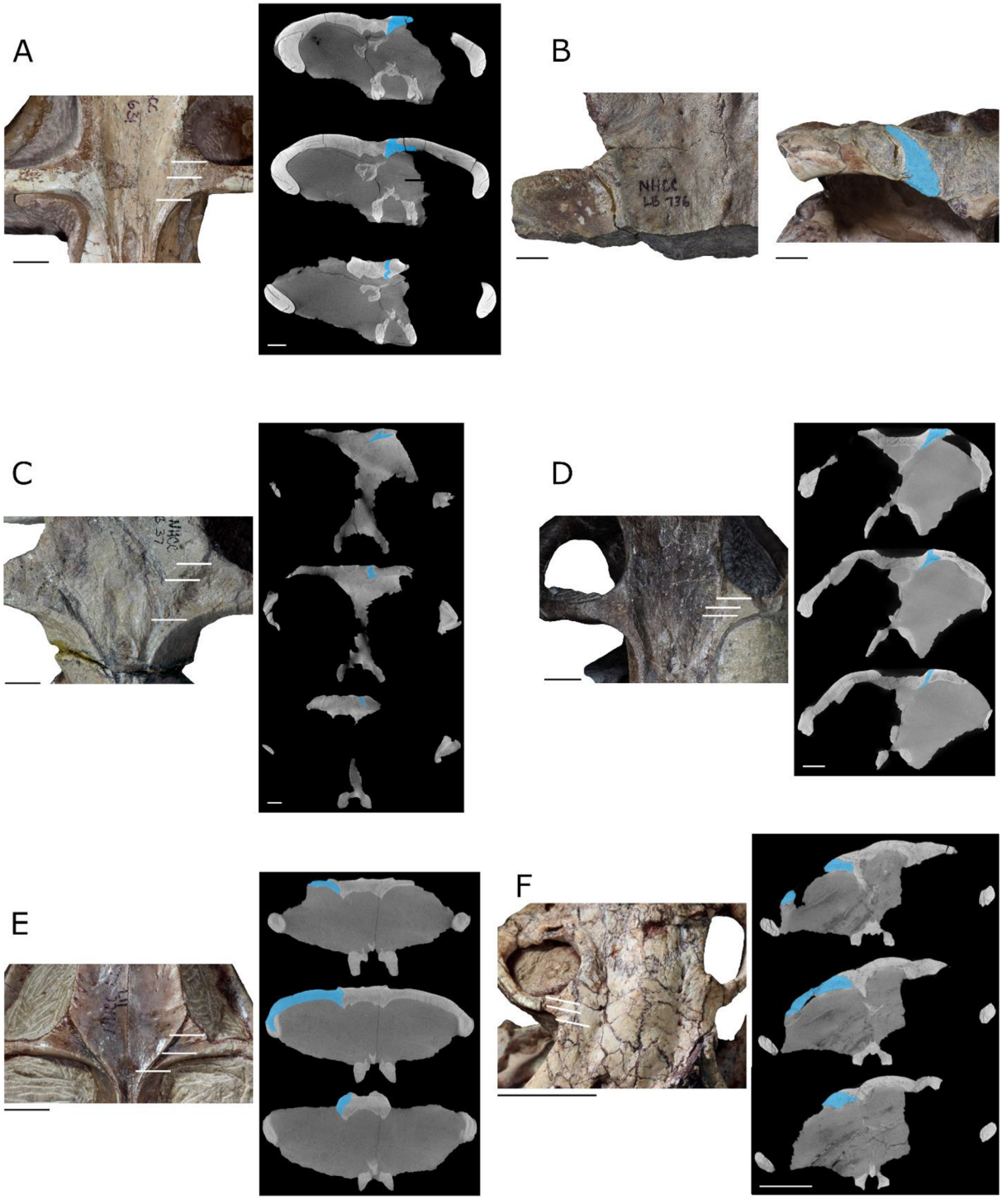

FIGURE 13. Comparisons of the postfrontal in dicynodonts. A, Photograph of the interorbital skull roof (left) and example micro-computed tomography slices (right) of *Oudenodon bainii* (NHCC LB631). B, Photographs of the left side of the interorbital skull roof (left) and the broken posterior surface of the skull roof (right) of *Aulacephalodon* sp. (NHCC LB736). C, Photograph of the interorbital skull roof (left) and example μCT slices (right) of an undescribed lystrosaurid (NHCC LB37). D, Photograph of the interorbital skull roof (left) and example μCT slices (right) of *Abajudon kaayai* (NHCC LB314). E, Photograph of the interorbital skull roof (left) and example μCT slices (right) of *Dicynodontoides* sp. (NHCC LB117). E, Photograph of the interorbital skull roof (left) and example μCT slices (right) of *Kembawacela kitchingi*. White lines in the photographs indicate the approximate planes shown in the μCT slices. The most anterior slice is at the top of each stack. The postfrontal is highlighted in blue in the μCT slices and on the broken surface of NHCC LNB736. Scale bars are 1 cm.

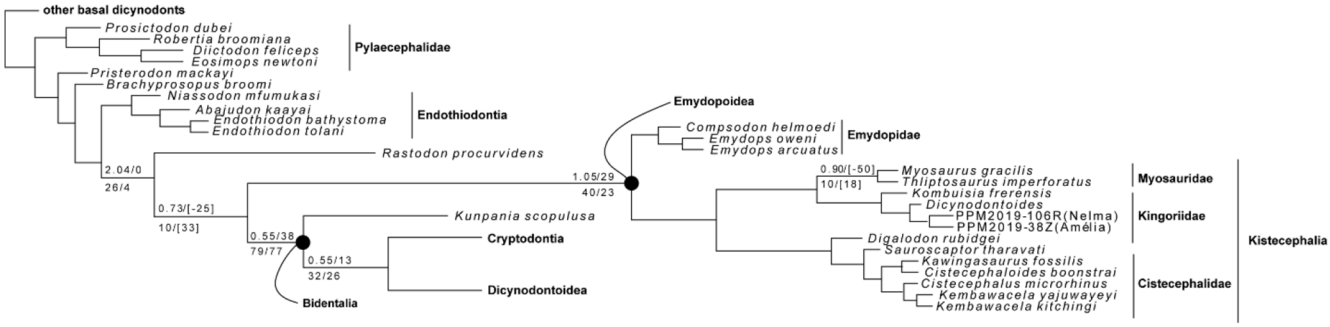

FIGURE 14. Phylogenetic analysis topology and branch support for a section of the tree. Bremer support and relative Bremer support above the tree branches, and symmetric resampling and GC values below the branches, based on 10k replications. Note the relatively strong support for the position of *Kunpania* as a basal bidentalian, whereas the position of *Rastodon* is particularly poorly supported. *Rastodon* can be retrieved as an emydopoid closely related to *Dicynodontoides* in some test analysis with different coding for some characters or outside Emydopoidea as shown above.

element was sufficiently remodeled to remove any discontinuities in its internal structure. A small piece of bone on the left side of the *Kembawacela* specimen, just behind the posterior margin of the orbit, is somewhat suggestive of perhaps representing the remains of a postfrontal element, but based on comparisons with the better-preserved right side, we think this more likely represents a broken fragment of bone that is delimited by cracks in the skull roof.

In summary, the emydopoids that lack a postfrontal appear to reduce this element in a notably different way compared to the endothiodont and bidentalians. Instead of reducing the exposure of the postfrontal on the skull roof by increasing the degree to which the postorbital and frontal overlap the postfrontal and maintaining a relatively large internal extent of the bone, the emydopoids show no evidence of a postfrontal ossification internally or externally. Our current dataset is too limited to determine whether the morphology in emydopoids reflects a fusion of the postorbital and postfrontal very early in ontogeny, or the actual loss of a postfrontal ossification center altogether, but further investigation of this previously unappreciated aspect of variation clearly is warranted.

Phylogenetic analysis

The results from the phylogenetic analysis shown in Fig. 14 largely align with earlier versions of the dataset (Kammerer et al. 2011, Macungo et al. 2022, Araújo et al. 2022b, Angielczyk et al. 2021, 2023). However, there are some significant changes in the topology that deserve attention: (1) *Rastodon* is now positioned as the basalmost member of Therocelonia; (2) *Kunpania* is identified as the basalmost member of Bidentalia; (3) *Thliptosaurus* is a sister-taxon to *Myosaurus*.

Regarding *Rastodon*'s position, its detailed character recoding and its similarities to *Dicynodontoides* suggest a more basal position, placing it outside of Emydopoidea. This result is in contrast to what Macungo et al. (2022) proposed, but we acknowledge that a better understanding of the palate and basicranial anatomy may produce different results. Hence, micro-computed tomography and bone-by-bone segmentation may elucidate many characters for this important taxon. Interestingly, when we adjusted the analysis by coding Discrete Character 41 (related to the presence of the postfrontal, as discussed earlier) as present for both *Dicynodontoides* and *Rastodon* (based on Boos et al. 2016) and removed the less complete taxon *Kunpania* (referenced in Angielvzyk et al. 2021), *Rastodon* emerged as a sister-taxon to *Dicynodontoides*. This finding underscores the significance of the postfrontal's evolution in emydopoids. It also hints at potential broader implications for understanding the evolutionary relationships among therochelonians. Following the most parsimonious tree, *Rastodon* is excluded from the bidentalian because: the relatively wide median pterygoid plate compared to basal skull length (Continuous Character 8), and we consider that the mid-ventral plate of the vomer has an overall shape comparable to other emydopoids despite considerable taphonomic deformation (Discrete Character 72, 73 and 74).

Kunpania is identified as the basalmost bidentalian, which represents a notably more basal position than what Angielczyk et al. (2021) suggested. They recovered it as a basal dicynodontoid and a sister-taxon to *Sintocephalus*. The structure of our tree

aligns more closely with the topology presented by Kammerer et al. (2011) than with the dicynodontoid arrangements of Liu (2021) and Angielczyk et al. (2023). In our tree, there is a sequence of stem-dicynodontoids, such as *Taoheodon* (as the basalmost dicynodontoid), *Repelinosaurus*, and *Dicynodon* spp. (Supplementary Information in Morphobank). These taxa provide the foundation for lystrosaurids and a clade that includes species like *Daptocephalus* spp. and *Turfanodon* spp. Importantly, several characteristics solidify *Kunpania*'s position as a bidentalian, specifically the height of anterior pterygoid keel in lateral view relative height of non-keel ramus (Continuous Char. 7); the length of the deltopectoral crest relative to the total humerus length (Continuous Char. 18); the presence of a distinct lateral caniniform buttress (Discrete Character 29); the absence of a keel-like extension of the palatal rim posterior to the caniniform process (Char. 30); the strong lateral bend of the jaw ramus (Discrete Character 115); the presence of an up-turned beak and scooped-out depression on the lower jaw as in most bidentalians (Discrete Character 121); the presence of a curved ridge that follows the profile of the symphysis present on the edge between the anterior and lateral surfaces of the dentary as in most bidentalians and unlike emydopoids and endothiodonts (Discrete Character 122); presence of a long, narrow and deep post-dentary sulcus, unlike emydopoids (Discrete Character 125); and the insertion of the latissimus dorsi is extended into a dorsoventrally flattened pinna-like process, unlike non-bidentalian dicynodonts (Discrete Character 152). The more basal position of *Kunpania* in the current analysis would also fit well with its potential middle Permian age (Angielczyk et al., 2021).

In contrast to the findings of Macungo et al. (2022), which placed Kingoriidae near the base of Emydopoidea, we obtained a more conventional arrangement as in Kammerer et al. (2011) and Angielczyk et al. (2023). In their work, Emydopidae was positioned at the base of Emyopoidea, followed by Kistecephalia. In our analysis, *Thliptosaurus* is identified as closely related to *Myosaurus*, with their relationship unified by a single synapomorphy: the development of the ventromedial process of the opisthotic into a robust, tuber-like knob (Discrete Character 181). However, it is important to note that the current topology should be considered tentative until a comprehensive bone-by-bone segmentation of *Myosaurus* and *Thliptosaurus* is conducted.

ACKNOWLEDGMENTS

We thank the PaleoMoz Project, FCT and AGA KHAN grant (333206718), National Geographic Society (CP-109R-17). We also thank Christian Kammerer and Julien Benoit for their insightful reviews.

REFERENCES

Angielczyk, K. D. (2002). Redescription, phylogenetic position, and stratigraphic significance of the dicynodont genus *Odontocyclops* (Synapsida: Anomodontia). *Journal of Paleontology*, 76, 1047–1059.

Angielczyk, K. D. (2007). New specimens of the Tanzanian dicynodont *"Cryptocynodon" parringtoni* von Huene, 1942 (Therapsida, Anomodontia), with an expanded analysis of Permian dicynodont phylogeny. *Journal of Vertebrate Paleontology*, 27, 116–131.

Angielczyk, K. D. & Sullivan, C. (2008). *Diictodon feliceps* (Owen, 1876), a dicynodont (Therapsida, Anomodontia) species with a Pangaean distribution. *Journal of Vertebrate Paleontology*, 28(3), 788-802.

Angielczyk, K. D. & Rubidge, B. S. (2013). Skeletal morphology, phylogenetic relationships and stratigraphic range of *Eosimops newtoni* Broom, 1921, a pylaecephalid dicynodont (Therapsida, Anomodontia) from the Middle Permian of South Africa. *Journal of Systematic Palaeontology*, 11(2), 191-231.

Angielczyk, K. D. & Schmitz, L. (2014). Nocturnality in synapsids predates the origin of mammals by over 100 million years. *Proceedings of the Royal Society B: Biological Sciences*, 281(1793), 20141642.

Angielczyk, K. D. & Kammerer, C. F. (2017). The cranial morphology, phylogenetic position and biogeography of the upper Permian dicynodont *Compsodon helmoedi* van Hoepen (Therapsida, Anomodontia). *Papers in Palaeontology*, 3(4), 513-545.

Angielczyk, K. D., Benoit, J., & Rubidge, B. S. (2021). A new tusked cistecephalid dicynodont (Therapsida, Anomodontia) from the upper Permian upper Madumabisa Mudstone formation, Luangwa Basin, Zambia. *Papers in Palaeontology*, 7(1), 405-446.

Angielczyk, K. D., Liu, J., & Yang, W. (2021). A redescription of *Kunpania scopulusa*, a bidentalian dicynodont (Therapsida, Anomodontia) from the ?Guadalupian of northwestern China. *Journal of Vertebrate Paleontology*, 41(1), e1922428.

Angielczyk, K. D., Brandon R. Peecook, & Roger M. H. Smith (2023). The mandible of *Compsodon helmoedi* (Therapsida: Anomodontia), with new records from the Ruhuhu Basin, Tanzania. *Palaeontologia Africana*, 56, 88–102.

Araújo, R., Fernandez, V., Rabbitt, R. D., Ekdale, E. G., Antunes, M. T., Castanhinha, R., Fröbisch, J., & Martins, R. M. (2018). *Endothiodon* cf. *bathystoma* (Synapsida: Dicynodontia) bony labyrinth anatomy, variation and body mass estimates. *PLoS one*, 13(3), e0189883.

Araújo, R., David, R., Benoit, J., Lungmus, J. K., Stoessel, A., Barrett, P. M., Maisano, J. A., Ekdale, E., Orliac, M., Luo, Z. X., & Martinelli, A. G. (2022a). Inner ear biomechanics reveals a Late Triassic origin for mammalian endothermy. *Nature*, 607(7920), 726-731.

Araújo, R., Macungo, Z., Fernandez, V., Chindebvu, E. G., & Jacobs, L.

L. (2022b). *Kembawacela yajuwayeyi* n. sp., a new cistecephalid species (Dicynodontia: Emydopoidea) from the Upper Permian of Malawi. *Journal of African Earth Sciences*, 196, 104726.

Barbolini, N., Smith, R. M. H., Tabor, N. J., Sidor, C. A., & Angielczyk, K. D. (2016). Resolving the age of Madumabisa fossil vertebrates. Palynological evidence from the Mid-Zambezi Basin of Zambia. *Palaeogeography, Palaeoclimatology, Palaeoecology*, 457, 117-128.

Benoit, J., Manger, P. R., & Rubidge, B. S. (2016). Palaeoneurological clues to the evolution of defining mammalian soft tissue traits. *Scientific Reports*, 6, 25604.

Benoit, J., Angielczyk, K. D., Miyamae, J. A., Manger, P., Fernandez, V., & Rubidge, B. (2018). Evolution of facial innervation in anomodont therapsids (Synapsida): Insights from X-ray computerized microtomography. *Journal of Morphology*, 279(5), 673-701.

Benoit, J., Dollman, K. N., Smith, R. M. H., & Manger, P. R. (2023). At the root of the mammalian mind: the sensory organs, brain, and behavior of pre-mammalian synapsids. In T. Calvey, A. A. de Sousa, & A. A. Baudet (Eds.), *Fossils to Mind* (pp. 25-72). *Progress in Brain Research*, 275.

Benton, M. J. (2021). The origin of endothermy in synapsids and archosaurs and arms races in the Triassic. *Gondwana Research*, 100, 261-289.

Berlin, J. C., Kirk, E. C., & Rowe, T. B. (2013). Functional implications of ubiquitous semicircular canal non-orthogonality in mammals. *PLoS One*, 8(11), e79585.

Boos, A. D., Kammerer, C. F., Schultz, C. L., Soares, M. B., & Ilha, A. L. (2016). A new dicynodont (Therapsida: Anomodontia) from the Permian of southern Brazil and its implications for bidentalian origins. *PLoS One*, 11(5), e0155000.

Boucot, A. J., Chen, X., Scotese, C. R., & Morley, R. J. (2013). *SEPM Concepts in Sedimentology and Paleontology*, Vol. 11, SEPM.

Bourke, J. M. & Witmer, L. M. (2023). Soft tissues influence nasal airflow in diapsids: Implications for dinosaurs. *Journal of Morphology*, 284(9), e21619.

Brink, A. S. (1950). On a new species of *Cistecephalus* Owen. *Annals & Magazine of Natural History*, Series 12, 985–997.

Brinkman, D. (1981). The structure and relationships of the dromasaurs (Reptilia; Therapsida). *Breviora*, 465, 1–34.

Broili, F. & Schröder, J. (1935). Beobachtungen an Wirbeltieren der Karrooformation. VI. Über den Schädel von *Cistecephalus* Owen. *Sitzungsberichte der Bayerischen Akademie der Wissenschaften Mathematisch-Naturwissenschaftliche Abteilung*, 1935, 1–20.

Broili, F. & J. Schröder. (1936). Beobachtunger an Wirberltieren der Karrooformation. XVI. Beobachtungen am Schädel von *Emydochampsa* Broom. *Sitzungberichte der Bayerischen Akademie der Wissenschaften Mathematisch-naturwissenschaftliche Abteilung*, 1936, 21–44.

Broom, R. (1906). On the Permian and Triassic faunas of South Africa. *Geological Magazine New Series*, 5, 29-30.

Bremer, K. (1994). Branch support and tree stability. *Cladistics*, 10, 295–304.

Buffenstein, R. & Yahav, S. (1991). Is the naked mole-rat *Hererocephalus glaber* an endothermic yet poikilothermic mammal? *Journal of Thermal Biology*, 16, 227–232.

Carlson, K. J., Stout, D., Jashashvili, T., De Ruiter, D. J., Tafforeau, P., & Berger, L. R. (2011). The endocast of MH1, *Australopithecus sediba*. *Science*, 333, 1402-1407.

Castanhinha, R., Araújo, R., Junior, L. C., Angielczyk, K. D., Martins, G. G., Martins, R. M., Chaouiya, C., Beckmann, F., & Wilde, F. (2013). Bringing dicynodonts back to life: paleobiology and anatomy of a new emydopoid genus from the Upper Permian of Mozambique. *PLoS One*, 8(12), e80974.

Cisneros, J. C., Abdala, F., Jashashvili, T., de Oliveira Bueno, A., & Dentzien-Dias, P. *Tiarajudens eccentricus* and *Anomocephalus africanus*, two bizarre anomodonts (Synapsida, Therapsida) with dental occlusion from the Permian of Gondwana. *Royal Society Open Science*, 2(7), 150090.

Cluver, M. A. (1971). The cranial morphology of the dicynodont genus *Lystrosaurus*. *Annals of the South African Museum*, 56, 155–274.

Cluver, M. A. (1974a). The skull and mandible of a new cistecephalid dicynodont. *Annals of the South African Museum*, 67, 7–23.

Cluver, M. A. (1974b). The cranial morphology of the Lower Triassic dicynodont *Myosaurus gracilis*. *Annals of the South African Museum*, 66, 35–54.

Cluver, M. A. (1978). The skeleton of the mammal-like reptile *Cistecephalus* with evidence for a fossorial mode of life. *Annals of the South African Museum*, 76, 213–246.

Cluver, M. A. & King, G. M. (1983). A reassessment of the relationships of Permian Dicynodontia (Reptilia, Therapsida) and a new classification of dicynodonts. *Annals of the South African Museum*, 91, 195–273.

Cox, C. B. (1959). On the anatomy of a new dicynodont genus with evidence of the position of the tympanum. *Procedings of the Zoological Society of London*, 132, 321–367.

Cox, C. B. (1964). On the palate, dentition, and classification of the fossil reptile *Endothiodon* and related genera. *American Museum Novitates*, 2171, 1–25.

Cox, C. B. (1972). A new digging dicynodont from the Upper Permian of Tanzania. In T. S. Kemp (Ed.), *Studies in vertebrate evolution* (pp. 73–189). Edinburgh: Oliver and Boyd.

Cox, C. B. & Angielczyk, K. D. (2015). A new endothiodont dicynodont (Therapsida, Anomodontia) from the Permian Ruhuhu Formation (Songea Group) of Tanzania and its feeding system. *Journal of Vertebrate Paleontology*, 35, e935388.

Crompton, A. W., Owerkowicz, T., Bhullar, B. A., & Musinsky, C. (2017). Structure of the nasal region of non-mammalian cynodonts and mammaliaforms: speculations on the evolution of mammalian endothermy. *Journal of Vertebrate Paleontology*, 37(1), e1269116.

Day, M. O. & Smith, R. M. H. (2020). Biostratigraphy of the *Endothiodon* Assemblage Zone (Beaufort Group, Karoo Supergroup), South Africa. *South African Journal of Geology*, 123(2), 165–180.

Escobar, J. A., Martinelli, A. G., Ezcurra, M. D., Fiorelli, L. E., Von Baczko, M. B., Novas, F. E., & Desojo, J. B. (2023). A Reassessment of the Mandibular Anatomy of *Dinodontosaurus brevirostris* (Synapsida, Dicynodontia) from the Ladinian–Early Carnian Chañares Formation (Northwestern Argentina), and Its Taxonomic and Phylogenetic Significance. *Ameghiniana*, 60(2), 178–201.

Ewer, R. F. (1961). The anatomy of the anomodont *Daptocephalus leoniceps* (Owen). *Proceedings of the Zoological Society of London*, 136(3), 375-402.

Fitzpatrick, R. C., Butler, J. E., & Day, B. L. (2006). Resolving head rotation for human bipedalism. *Current Biology*, 16, 1509–1514.

Fröbisch J. (2007). The cranial anatomy of *Kombuisia frerensis* Hotton (Synapsida, Dicynodontia) and a new phylogeny of anomodont therapsids. *Zoological Journal of the Linnean Society*, 150, 117–144.

Fröbisch, J. & Reisz, R. R. (2008). A new species of *Emydops*

(Synapsida, Anomodontia) and a discussion of dental variability and pathology in dicynodonts. *Journal of Vertebrate Paleontology*, 28(3), 770-787.

Fröbisch, J., Angielczyk, K. D., & Sidor, C. A. (2010). The Triassic dicynodont *Kombuisia* (Synapsida, Anomodontia) from Antarctica, a refuge from the terrestrial Permian-Triassic mass extinction. *Naturwissenschaften*, 97, 187–196.

Goloboff, P. A. (1999). Analyzing large data sets in reasonable times: solutions for composite optima. *Cladistics*, 15, 415–428.

Goloboff, P. A. & Farris, J. S. (2001). Methods for quick consensus estimation. *Cladistics*, 17, S26–S34.

Goloboff, P. A., Farris, J. S., Källersjö, M., Oxelman, B., Ramírez, M. J., & Szumik, C. A. (2003). Improvements to resampling measures of group support. *Cladistics*, 19, 324–332.

Goloboff, P. A. & Catalano, S. A. (2016). TNT version 1.5, including a full implementation of phylogenetic morphometrics. *Cladistics*, 32, 221–238.

Hertz, P. E., Huey, R. B., & Garland Jr, T. (1988). Time budgets, thermoregulation, and maximal locomotor performance: are reptiles olympians or boy scouts? *American Zoologist*, 28(3), 927-938.

Hillenius, W. J. (1992). The evolution of nasal turbinates and mammalian endothermy. *Paleobiology*, 18(1), 17–29.

Hillenius, W. J. (1994). Turbinates in therapsids: evidence for Late Permian origins of mammalian endothermy. *Evolution*, 48(2), 207-229.

Ivakhnenko, M. F. (1996). Primitive anomodonts, venyukoviids, from the Late Permian of Eastern Europe. *Paleontological Journal*, 30, 575–582.

Kammerer, C. F. (2019). A new dicynodont (Anomodontia: Emydopoidea) from the terminal Permian of KwaZulu-Natal, South Africa. *Palaeontologia africana*, 53, 179–191.

Kammerer, C. F. & Smith, R. M. S. (2017). An early geikiid dicynodont from the *Tropidostoma* Assemblage Zone (late Permian) of South Africa. *PeerJ*, 5, e2913.

Kammerer, C. F., Angielczyk, K. D., & Fröbisch, J. (2011). A comprehensive taxonomic revision of *Dicynodon* (Therapsida, Anomodontia) and its implications for dicynodont phylogeny, biogeography, and biostratigraphy. *Society of Vertebrate Paleontology Memoir*, 11, 1–158.

Kammerer, C. F. (2015). Redescription of *Digalodon rubidgei*, an emydopoid dicynodont (Therapsida, Anomodontia) from the Late Permian of South Africa. *Fossil Record*, 18(1), 43-55.

Kammerer, C. F., S. Bandyopadhyay, & S. Ray. (2016). A new taxon of cistecephalid dicynodont from the Upper Permian Kundaram Formation of India. *Papers in Palaeontology*, 2, 589–594.

Kammerer, C. F., R. Araújo, K. Cumbane, Z. Macungo, R. M. H. Smith, & K. D. Angielczyk. (2021). New material of *Dicynodon angielczyki* (Synapsida: Anomodontia) from Mozambique and Zambia with biostratigraphic implications for African Permo-Triassic basins. *Journal of Vertebrate Paleontology*, 41(6). DOI: 10.1080.02724634.2021.2041652.

Kammerer, C. F. (2021). Elevated cranial sutural complexity in burrowing dicynodonts. *Frontiers in Ecology and Evolution*, 9, 674151.

Keyser, A. W. (1965). The morphology of the anomodont genus *Cistecephalus* Owen (1876). (M.Sc. thesis, University of Pretoria.)

Keyser, A. W. (1973). A preliminary study of the type area of the *Cistecephalus* Zone of the Beaufort Series, and a revision of the anomodont family Cistecephalidae. *Geological Survey of South Africa*, 62, 1–71.

Keyser, A. W. (1975). A reevaluation of the cranial morphology and systematics of some tuskless Anomodontia. *Geological Survey of South Africa Memoir*, 67, 1–110.

Kitching, J. W. (1970). A short review of the Beaufort zoning in South Africa in *Second Gondwana Symposium- Proceedings and Papers*. Council for Scientific and Industrial Research, Pretoria, 309–312.

Kramer, D. L. & McLaughlin, R.L. (2001). The behavioral ecology of intermittent locomotion. *American Zoologist*, 41(2), 137-153.

Laaß, M., Hampe, O., Schudack, M., Hoff, C., Kardjilov, N., & Hilger, A. (2010). New insights into the respiration and metabolic physiology of *Lystrosaurus*. *Acta Zoologica*, 92, 363–371.

Laaß, M. (2015). Bone-conduction hearing and seismic sensitivity of the late Permian anomodont *Kawingasaurus fossilis*. *Journal of Morphology*, 276(2), 121–143.

Laaß, M. & Kaestner, A. (2023). Nasal turbinates of the dicynodont *Kawingasaurus fossilis* and the possible impact of the fossorial habitat on the evolution of endothermy. *Journal of Morphology*, 284(9), e21621.

Lyckegaard, A., Johnson, G., & Tafforeau, P. (2011). Correction of ring artifacts in X-ray tomographic images. *International Journal of Tomography and Statistics*, 18, 1-9.

Lindenlaub, T., Burda, H., & Nevo, E. (1995). Convergent evolution of the vestibular organ in the subterranean mole-rats *Cryptomys* and *Spalax*, as compared with the aboveground rat, *Rattus*. *Journal of Morphology*, 224, 303–311.

Liu, J., B. Rubudge, & J. Li. (2010). A new specimen of *Biseridens qilianicus* indicates its phylogenetic position as the most basal anomodont. *Proceedings of the Royal Society B*, 277, 285–292.

Liu, J. (2021). The tetrapod fauna of the upper Permian Naobaogou Formation of China: 6. *Turfanodon jiufengensis* sp. nov. (Dicynodontia). *PeerJ*, 9, e10854.

Liu, J. (2022). On kannemeyeriiform dicynodonts from the *Shaanbeikannemeyeria* Assemblage Zone of the Ordos Basin, China. *Vertebrata Palasiatica*, 60(3), 212-248.

Lungmus, J. K. & Angielczyk, K. D. (2021). Phylogeny, function and ecology in the deep evolutionary history of the mammalian forelimb. *Proceedings of the Royal Society B*, 288, 20210494.

Macungo, Z., Loide, I., Zunguza, S., Nhamutole, N., Maharaj, I. E. M., Mugabe, J., Angielczyk, K. D., & Araújo, R. (2020). *Endothiodon* (Therapsida, Anomodontia) specimens from the middle/late Permian of the Metangula Graben (Niassa Province, Mozambique) increase complexity to the taxonomy of the genus. *Journal of African Earth Sciences*, 163, 103647.

Macungo, Z., Benoit, J., Fernandez, V., & Araújo, R. (2022). X-ray microcomputed and synchrotron tomographic analysis of the basicranial axis of emydopoid dicynodonts: implications for fossoriality and phylogeny. *Zoological Journal of the Linnean Society*, 198(1), 1-46.

Maisch, M. W. (2001). Observations on Karoo and Gondwana vertebrates. Part 2: a new skull-reconstruction of *Stahleckeria potens* von Huene, 1935 (Dicynodontia, Middle Triassic) and a reconsideration of kannemeyeriiform phylogeny. *Neues Jahrbuch für Geologie und Paläontologie Abhandlungen*, 220, 127–152.

Maisch, M. W. & Gebauer, E. V. I. (2005). Reappraisal of *Geikia locusticeps* (Therapsida: Dicynodontia) from the Upper Permian of Tanzania. *Palaeontology*, 48, 309–324.

Martinez, Q., Clavel, J., Esselstyn, J. A., Achmadi, A. S., Grohé, C., Pirot, N., & Fabre, P. H. (2020). Convergent evolution of olfactory

and thermoregulatory capacities in small amphibious mammals. *Proceedings of the National Academy of Sciences*, 117(16), 8958-8965.

Martinez, Q., Okrouhlík, J., Šumbera, R., Wright, M., Araújo, R., Braude, S., Hildebrandt, T. B., Holtze, S., Ruf, I., & Fabre, P. H. (2023). Mammalian maxilloturbinal evolution does not reflect thermal biology. *Nature Communications*, 14(1), 4425.

Mayhew, W. W. (1965). Hibernation in the horned lizard, *Phrynosoma m'calli*. *Comparative Biochemistry and Physiology*, 16(1), 103-119.

McVean, A. (1999). Are the semicircular canals of the European mole, *Talpa europaea*, adapted to a subterranean habitat?. *Comparative Biochemistry and Physiology Part A: Molecular & Integrative Physiology*, 123(2), 173-178.

Mirone, A., Brun, E., Gouillart, E., Tafforeau, P., & Kieffer, J. (2014). The PyHST2 hybrid distributed code for high-speed tomographic reconstruction with iterative reconstruction and a priori knowledge capabilities. *Nuclear Instruments and Methods in Physics Research Section B: Beam Interactions with Materials and Atoms*, 324, 41-48.

Mozell, M. M. (1970). Evidence for a chromatographic model of olfaction. *Journal of General Physiology*, 56, 46–63.

Nasterlack, T., Canoville, A., & Chinsamy, A. (2012). New insights into the biology of the Permian genus *Cistecephalus* (therapsida, dicynodontia). *Journal of Vertebrate Paleontology*, 32(6), 1396–1410.

Olroyd, S. L., Sidor, C. A., & Angielczyk, K. D. (2018). New materials of the enigmatic dicynodonts *Abajudon kaayai* (Therapsida, Anomodontia) from the lower Madumabisa Mudstone Formation, middle Permian of Zambia. *Journal of Vertebrate Paleontology*, 37(6). DOI: 10.10180/02724634.2017.1403442.

Owerkowicz, T., Musinsky, C., Middleton, K. M., & Crompton, A. W. (2015). Respiratory turbinates and the evolution of endothermy in mammals and birds. In K. P. Dial, N. Shubin, & E. L. Brainerd (Eds.), *Great Transformations in Vertebrate Evolution* (pp. 143–165). University of Chicago Press.

Paganin, D., Mayo, S., Gureyev, T. E., Miller, P. R., & Wilkins, S. W. (2002). Simultaneous phase and amplitude extraction from a single defocused image of a homogeneous object. *Journal of Microscopy*, 206, 33-40.

Pianka, E. R. (1986). *Ecology and natural history of desert lizards: analyses of the ecological niche and community structure.* Princeton University Press.

Plessis, A., le Roux, S. G., & Guelpa, A. (2016). The CT Scanner Facility at Stellenbosch University: An open access X-ray computed tomography laboratory. *Nuclear Instruments & Methods in Physics Research. Section B, Beam Interactions with Materials and Atoms*, 384, 42–49. DOI: 10.1016/j.nimb.2016.08.005.

Rabbitt, R., Damiano, E., & Grant, J. (2003). Biomechanics of the vestibular semicircular canals and otolith organs. In: *The Vestibular System*, edited by Highstein SM, Popper A, Fay R. New York: Springer.

Ray, S. (2000). Endothiodont dicynodonts from the Late Permian Kundaram Formation, India. *Palaeontology*, 43, 375–404.

Rees, P. M. et al. (2002). Permian phytogeographic patterns and climate data/model comparisons. *Journal of Geology*, https://doi.org/10.1086/324203.

Rey, K. et al. (2016). Global climate perturbations during the Permo-Triassic mass extinctions recorded by continental tetrapods from South Africa. *Gondwana Research*, 37, 384–396.

Roscher, M., Stordal, F., & Svensen, H. (2011). The effect of global warming and global cooling on the distribution of the latest Permian climate zones. *Palaeogeography Palaeoclimatology Palaeoecology*, 309, 186–200.

Rowe, T. B., Macrini, T. E., & Luo, Z.-X. (2011). Fossil evidence on origin of the mammalian brain. *Science*, 332, 955–957.

Rubidge, B. S. & Hopson, J. A. (1996). A primitive anomodont therapsid from the base of the Beaufort Group (Upper Permian) of South Africa. *Zoological Journal of the Linnean Society*, 117, 115–139.

Rubidge, B. S., Erwin, D. H., Ramezani, J., Bowring, S. A., & de Klerk, W. J. (2013). High-precision temporal calibration of Late Permian vertebrate biostratigraphy: U-Pb zircon constraints from the Karoo Supergroup, South Africa. *Geology*, 41, 363-366.

Ruben, J. A., Hillenius, W. J., Kemp, T. S., & Quick, D. E. (2012). The evolution of mammalian endothermy. In A. Chinsamy (Ed.), *Forerunners of Mammals: Radiation, Histology, Biology* (pp. 273–286). Indiana University Press.

Rybczynski, N. (2000). Cranial anatomy and phylogenetic position of *Suminia getmanovi*, a basal anomodont (Amniota: Therapsida) from the Late Permian of Eastern Europe. *Zoological Journal of the Linnean Society*, 130, 329–373.

Schmidt-Nielsen, K., Hainsworth, F. R., & Murrish, D. E. (1970). Counter-current heat exchange in the respiratory passages: Effect on water and heat balance. *Respiratory Physiology*, 9, 263–276.

Schoenfeld, T. A. & Cleland, T. A. (2005). The anatomical logic of smell. *Trends in Neurosciences*, 28(11), 620-627.

Shi, Y. T. & Liu, J. (2023). The tetrapod fauna of the upper Permian Naobaogou Formation of China: 10. *Jimusaria monanensis* sp. nov. (Dicynodontia) shows a unique epipterygoid. *PeerJ*, 11, e15783.

Simão-Oliveira, D., Kerber, L., & Pinheiro, F. (2020). Endocranial morphology of the Brazilian Permian dicynodont *Rastodon procurvidens* (Therapsida: anomodontia). *Journal of Anatomy*, 236(3), 384-397.

Smith, R. M. H. & Keyser, A. W. (1995). Biostratigraphy of the Cistecephalus Zone. In B. S. Rubidge (Editor), *Biostratigraphy of the Beaufort Group (Karoo Supergroup)*, S.A.C.S. Biostratig. Series 1, 23-28.

Smith, R. M. H. (2020). Biostratigraphy of the *Cistecephalus* Assemblage Zone (Beaufort Group, Karoo Supergroup), South Africa. *South African Journal of Geology*, 123(2), 181-190.

Smith, R. M., Angielczyk, K. D., Benoit, J., & Fernandez, V. (2021). Neonate aggregation in the Permian dicynodont *Diictodon* (Therapsida, Anomodontia): evidence for a reproductive function for burrows?. *Palaeogeography, Palaeoclimatology, Palaeoecology*, 569, 110311.

Southwood, A. & Avens, L. (2010). Physiological, behavioral, and ecological aspects of migration in reptiles. *Journal of Comparative Physiology B*, 180, 1-23.

Szczygielski, T. & Sulej, T. (2023). *Woznikella triradiata* n. gen., n. sp. – a new kannemeyeriiform dicynodont from the Late Triassic of northern Pangea and the global distribution of Triassic dicynodonts. *Comptes Rendus Palevol*, 22(16), 279-406.

Yagi, K. T. & Litzgus, J. D. (2013). Thermoregulation of spotted turtles (*Clemmys guttata*) in a beaver-flooded bog in southern Ontario, Canada. *Journal of Thermal Biology*, 38*(5), 205-213.

Zhang, J., Cai, R., Liang, J., et al. (2021). Molecular mechanism of Chinese alligator (*Alligator sinensis*) adapting to hibernation. *Journal of Experimental Zoology (Molecular and Developmental Evolution)*, 336, 32–49.

SUPPLEMENTARY INFORMATION – COMPUTED TOMOGRAPHY-BASED RE-DESCRIPTION OF THE SKULL AND MANDIBLE OF THE MID-PERMIAN DICYNODONT *DIICTODON FELICEPS* SPECIMEN GPIT-PV-60758.

INTRODUCTION

Anomodontia was first described by Richard Owen (1859) and was one of the most speciose tetrapod clades during the Permian and Triassic (Fröbisch, 2008; Kammerer et al., 2011). Anomodonts were herbivorous non-mammalian therapsids that dominated terrestrial habitats, ranging from small burrowers (e.g., Castanhinha et al., 2013) to hippopotamus-sized grazers (e.g., Sulej and Niedzwiedzki, 2019). Most of anomodont diversity is represented by the largest anomodont sub-clade, Dicynodontia (Owen, 1859). Initially, many new specimens were allocated to the genus *Dicynodon*, which was originally described to group newly discovered reptiles with some mammal-like features (Owen, 1845). This practice persisted through most of the first half of the 20th century, making it a taxonomic wastebasket and resulting in the grouping of several species with unclear affinities (Broom, 1911).

The chaotic state of taxonomy within *Dicynodon* led to an extensive revision of the genus (Kammerer et al., 2011). *Dicynodon megalorhinus*, one of the 168 species ascribed to this genus (Kammerer et al., 2011), is a good representation of its contorted taxonomic history. It was first described based on a skull from the middle Permian, *Tapinocephalus* Assemblage Zone of South Africa (SAM-PK-640; Broom, 1904). SAM-PK-640 was ascribed to the genus *Oudenodon*, which was later synonymized with *Dicynodon* by the same author (Broom, 1913). The specimen was later assigned to the genus *Orophicephalus* (Van Hoepen, 1934) and subsequently re-erected as *D. megalorhinus* (Toerien, 1953; Haughton and Brink, 1954; King, 1988). *Dicynodon megalorhinus* was considered as a synonym of *Diictodon feliceps*, but the *D. megalorhinus* holotype lacks synapomorphies of all species to which it has been ascribed (Kammerer et al., 2011). The external anatomy of SAM-PK-640 is poorly preserved and its lack of preparation keeps several traits unrevealed (Kammerer et al., 2011). Nevertheless, Kammerer et al. (2011) identified this specimen as falling within *Emydops* based on the shape of the palatal rim, the occiput, the width of the intertemporal region, and the broad exposition of the parietals. Therefore, since the specimen described here, GPIT-PV-60758, was referred to *D. megalorhinus*, and SAM-PK-640 — the holotype of *D. megalorhinus* — is still identified as *Emydops* sp. to date (Kammerer et al. 2011), this specimen does not impact the nomenclatural status of the taxon. Indeed, Brink (1986) had already listed by GPIT-PV-60758 as *Diictodon feliceps*, and subsequent authors maintained this ascription (Kammerer et al. 2011, 2020).

GPIT-PV-60758 was a specimen found near Abrahamskraal (South Africa) originally described by von Huene (1931), consisting of a complete skull and mandible (Fig. 1). The abundance of *Diictodon* while being a key species among dicynodonts justify anatomical description using computed tomography. X-ray micro-computed tomography (µCT) has become an increasingly important tool to paleontologists (e.g., Castanhinha et al., 2013; Laaß, 2015). We describe the internal and external anatomy of GPIT-PV-60758, including the bony labyrinths and the braincase endocast. Our phylogenetic analysis recovers this specimen as a sister taxon to *Diictodon feliceps,* providing support to the current ascription (e.g., Brink 1986, Kammerer et al. 2020). *Diictodon feliceps* has a Pangean distribution, spanning from middle to late Permian (Angielczyk and Sullivan 2008). We analyze and discuss the differences between GPIT-PV-60758 and other *Di. feliceps* specimens. We discuss the range of variation within *Di. feliceps* and the relevance of ontogenetically variable traits in the occipital and cranial vault regions of dicynodonts.

MATERIALS AND METHODS

X-ray µ-CT scanning and segmentation

GPIT-PV-60758 (Figs. 1, 2) consists of a complete skull and partially preserved lower jaws collected near Blaauw Krantz, close to Abrahamskraal, in South Africa (von Huene, 1931). The specimen is housed at the Institut für Geowissenschaften der Universität Tübingen, Paläontologische Sammlung (Germany). Von Huene (1931) reported that GPIT-PV-60758 was collected in strata assigned to the *Tapinocephalus* Assemblage Zone

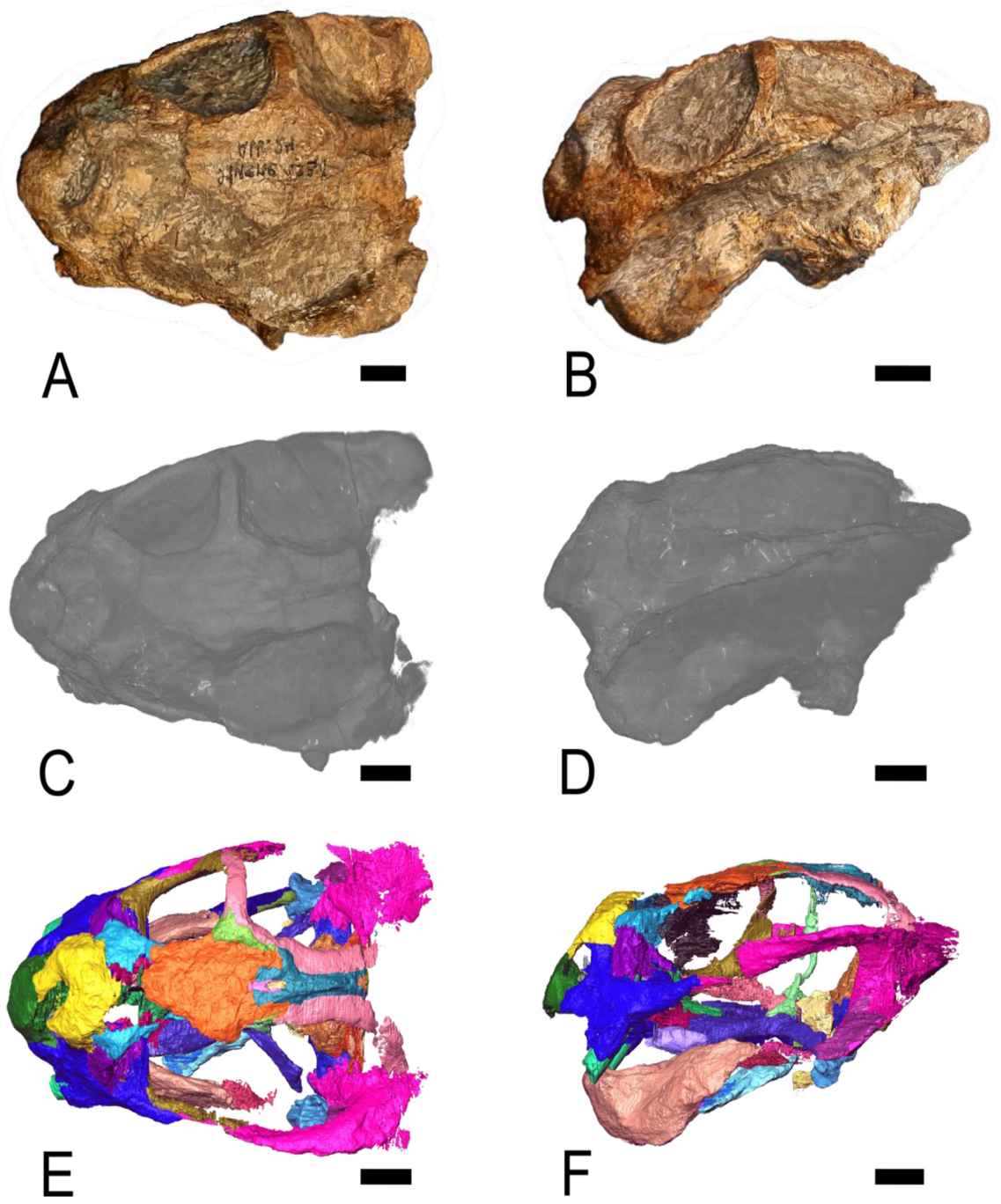

FIGURE 1. Dorsal (A, C, E) and lateral (B, D, F) views of GPIT-PV-60758. The specimen is on top (A, B), the volume rendering of the µ-CT scan is on the middle (C, D), and the 3D segmentation with colors representing different bones is on the bottom (E, F). Scale bar = 10 mm.

(van der Walt et al., 2010). These sediments date from the middle Permian, with more than 261Ma (Rubidge et al., 2013). Von Huene (1922) described the external anatomy of the relatively well-preserved and well-prepared GPIT-PV-60758 and ascribed it to *Dicynodon megalorhinus*. The most recent publication including this specimen grouped it with many other specimens in the species *Diictodon feliceps* (Kammerer et al. 2020).

We used Propagation Phase Contrast Synchrotron Radiation-based (PPC-SR) micro-Computed Tomography (µCT) to scan

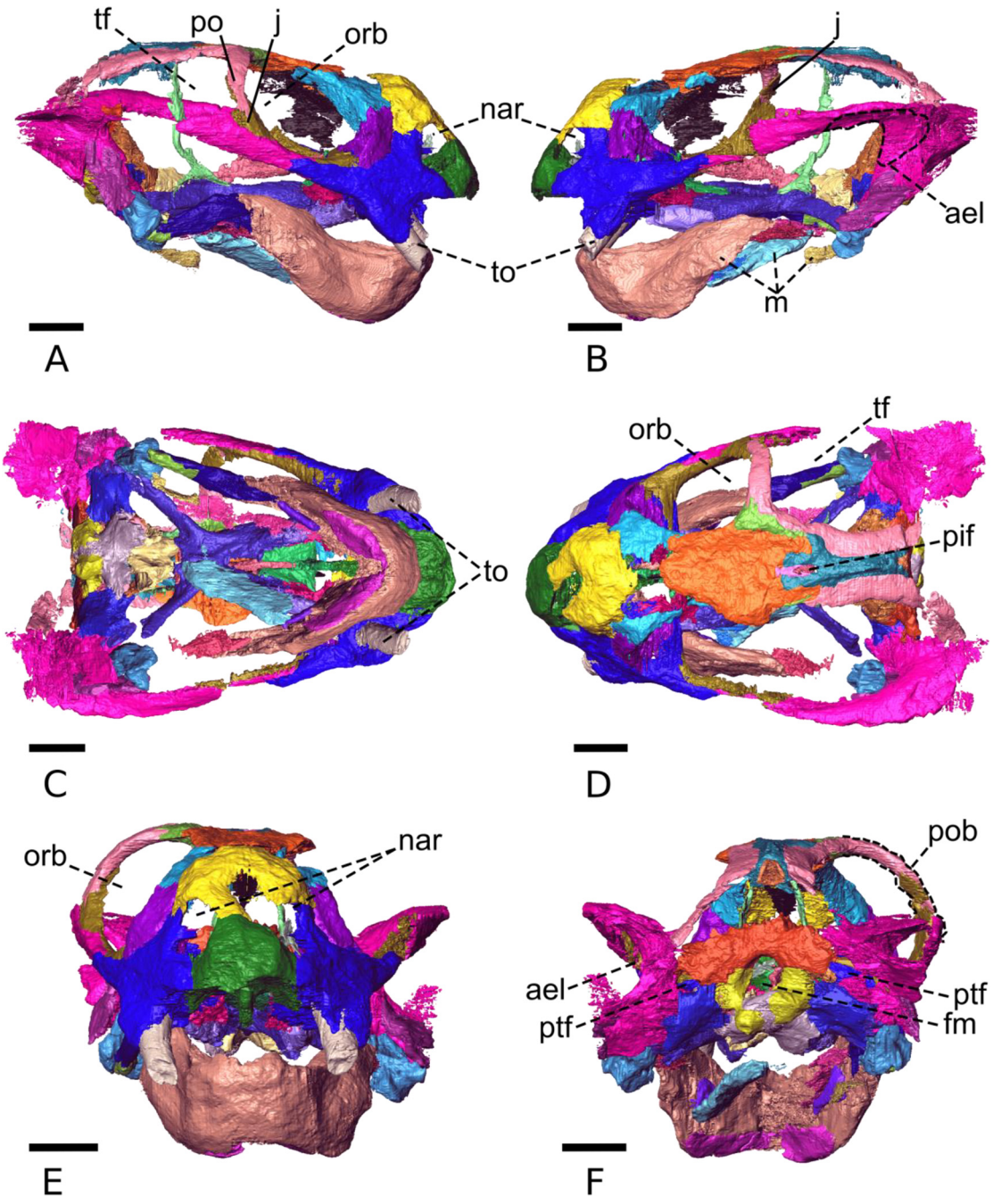

FIGURE 2. 3D segmentation of GPIT-PV-60758, with different colors corresponding to different bones. The skull is shown in right and left lateral views (A, B), ventral (C), dorsal (D), anterior (E) and posterior (F) views. ael - origin of the *adductor externus lateralis*; fm - foramen magnum; j - jugal; m - maxilla; nar - naris; orb - orbit; pif - pineal foramen; po - postorbital; pob - postorbital bar; ptf - posttemporal fenestra; t - tooth; tf - temporal fenestra. Dashed lines point anatomical structures. Scale bar = 10 mm.

GPIT-PV-60758 at the European Synchrotron Radiation Facility (ESRF, Grenoble, France). The setup was the same as that reported in Araújo et al. (2017). The resulting scan was composed of 1285 tomograms, with a voxel size of 46.57 µm. Projections were assembled and the scan reconstructed using PyHST2 software (Paganin et al., 2002; Mirone et al., 2014), with the same parameters as in Araújo et al. (2017).

The GPIT-PV-60758 scan was binned (resolution reduced

by half) in order to facilitate the manipulation of the file. Avizo 8.1 (FEI Vizualization Sciences Group, Mérignac, France) was used to perform the segmentation of the binned version of the scan. Because of the poor contrast between bone and sediment, most of the segmentation was done manually, with the "brush" tool (Fig. 2). Whenever a structure cross-section presented a regular shape, the area of interest was selected every five slices and the final volume was obtained using the "Interpolate" function. The olfactory bulbs, dorsal, and basicranial/occipital regions of the endocast were manually segmented. The cartilaginous lateral walls of the braincase are not preserved in GPIT-PV-60758, making the exact shape of the endocast is impossible to derive. Therefore, the median and ventral regions between the posterior limit of the olfactory bulbs and the epipterygoid bones were interpolated. The bony labyrinths were manually segmented. If semicircular canals were damaged, the segmentation was performed only if the shape was predictable from the preserved parts. All length measurements were performed with the "Measure" tool in the surface viewer menu of Avizo 8.1. Endocranial volumes were calculated with the "Material statistics" function.

ANATOMICAL DESCRIPTION

Palate

Premaxilla

The premaxilla is the most anterior element of the snout, forming the round apex of the keratinous beak (Figs. 2, 3). In GPIT-PV-60758, the premaxilla is a single bone with no visible suture separating the two paired elements found in some other specimens (Sullivan & Reisz, 2005). As in almost all other dicynodonts there are no premaxillary teeth. The premaxilla is bordered by the nasals dorsally, the maxillae posterolaterally and by the vomer posteriorly (Fig. 2). The premaxilla anterior surface slopes posterodorsally towards the nasals and its lateral expansions confer a triangular shape in anterior view (Fig. 2E). Ventrally, the bone is subrectangular (Fig. 3D), becoming more triangular as it narrows towards its contact with the vomer, finishing in an ascending process that projects dorsoventrally, forming a well-defined median ridge (Fig. 3D). The premaxilla has a considerable palatal contribution and it forms the anteroventral margin of the internal nares, along with the maxilla (Figs. 2A,B, 3A,B). The premaxilla-maxilla suture extends from the palate to the ventral margin of the naris. Ventrally, this suture extends to the the level of the posterior edge of the latter. The contact between premaxilla and vomer occurs along the sagittal skull midline, with the vomer projecting anteriorly to lie just dorsal to the ascending process of the premaxilla, reaching close the midpoint of the nasal cavity (Fig. 3C). The badly preserved dorsal process of the premaxilla in GPIT-PV-60758 does not allow identification of its forked insertion into the nasal boss or the precise shape of the dorsal margin of the external nares. In palatal view, the anterior ridges of the premaxilla are badly preserved, only allowing identification of the worn right anterior ridge (Fig. 3D). However, it is possible to identify the depression between both anterior ridges (Fig. 3D). The posterior projection of the left anterior ridge appears to converge towards the anterior part of the median posterior ridge, despite being severely worn (Fig. 3D). Two well-defined depressions (Sullivan & Reisz, 2005) flank the posterior ridge (Fig. 3D). The left depression is better preserved, displaying a small vascular groove just lateral to the posterior ridge (Fig. 3D). The lateral eminences that run along the suture with the maxillae, in palatal view, can be easily identified both in the 3D reconstruction (Fig. 3D).

Septomaxilla

Only the left bone is partially preserved in GPIT-PV-60758, and it is a small and delicate bone located in the nasal cavity, close to the posteroventral part of the naris (Fig. 3A-C). The septomaxilla can be divided in two flattened processes. The ventral process contacts the premaxilla and the dorsal process contacts the maxilla on the lateral margin of the nostril (Fig. 3C). The ventral process is mediolaterally elongated and its suture with the premaxilla extends from the posterior margin of the ascending process of the premaxilla (medially) to near the premaxilla-maxilla suture (laterally; Figs. 3A & S1). The dorsal process is dorsoventrally elongated, with its dorsal extremity contacting the maxilla close to the nasomaxillary suture whereas its ventral tip reaches just posteriorly to the most ventrolateral margin of the left nostril (Fig. S1). The cross-section of the septomaxilla is subtriangular due to the secondary contact between the distal tips of both processes (Fig. S1).

Maxilla

The anterior and anterodorsal portions of the paired maxillae are poorly preserved (Figs. 2, 3). The maxilla bears one caniniform tooth and comprises the anterolateral part of the face. The maxilla borders the premaxilla anteriorly and medially, the nasal anterodorsally, the lacrimal dorsolaterally, the jugal posterolaterally, both the jugal and the squamosal along the medial surface of the zygomatic process of the maxilla, the ectopterygoid posterolaterally and the palatine posteroventrally (Figs. 2, 3). The ventral aspect of the maxilla is subtriangular. Its medial margin contacts the premaxilla along an interdigitating subtriangular suture. At mid-length of its anteroposterior axis, the maxilla displays an anteroventrally projecting caniniform process. Dorsal to the caniniform teeth, the maxilla does not display a maxillary antrum. The caniniform tooth is ankylosed to the alveolar bone, i.e., there is no space filled with matrix between the caniniform tooth and the enveloping maxilla alveolar bone (Fig. S2). This space is typically filled by the periodontal ligament in life and its absence in GPIT/RE/'9275 is similar to the condition observed in other *Diictodon* specimens (LeBlanc et al. 2018; Whitney et al. 2021). More posteriorly, the ectopterygoid projects anteriorly to form an interdigitating suture with the maxillary posteromedial margin. The posterior portion of the medial margin of the maxilla contacts the palatine bone along a large interdigitating suture. The palatine prevents the contact of the medial part of the maxilla with the vomer (Fig. 3C). Anterodorsally, the maxilla forms the posterior margin of the nares and contacts the nasal dorsally to form its posterodorsal margin (Fig. 2A, B, E). The posterodorsal margin of the maxilla forms a fossa where the large lacrimal bone is embedded, preventing the maxilla from contacting the prefrontal (Figs. 2-4A, B). The lateral surface of the maxilla is flat anteriorly, but its posterior margin bulges to form the caniniform process (Figs. 2A, B, 3A, B). The caniniform process extends dorsally to the mid-height of the maxilla. The posteromedial surface of the maxilla is horizontally flat near the contacts with the jugal and the lacrimal (Figs. 2D, 3A, B, C). Posteriorly, the zygomatic process of the maxilla projects smoothly from the caniniform process and nearly reaches the postorbital process of the jugal (Fig. 2C). The zygomatic process of the maxilla sharpens posteriorly, and borders the lateral surface of the jugal anteriorly, and the anterior process of the squamosal posteriorly (Fig. 2C, D).

Vomer

The vomers are coossified at the midline of the nasal cavity to form the internarial septum (Fig. 3C, D). Although the vomers coossify anteriorly, the intervomeral suture is visible in cross-section, posterior to the internal nares (Fig. S3). The vomer contacts the premaxilla anteriorly, the palatine laterally, the cultriform process of the parabasisphenoid posteriorly, the pterygoids posteriorly, and the ethmoid posterodorsally (Fig. 3). The vomer is composed of two major anatomical subunits: the internarial septum and the mid-ventral plate. The internarial septum lays along the dorsal edge of the posterior ridge of the premaxilla (Fig. 3C). The vomer receives the anterior part of the cultriform process of the parabasisphenoid posterodorsally. These two bones form the insertion area of the ventral portion of the sphenethmoid (Fig. 3A, B). Ventral to its contact with the sphenethmoid, the vomer presents its maximum height, dividing the choanae posteriorly (Fig. 3D). The vomers project laterally to contact the palatines at the posteriormost part of the internarial septum (Fig. 3C). These vomerine lateral projections form a plate-like coronal section (mid-ventral plate) that constitute the roof of the choanae (Fig. 3D). Posteriorly, the mid-ventral plates of the vomer are two symmetric subtriangular processes that project along the suture with the palatines. The mid-ventral plates of the vomer frame the interpterygoid vacuity anteriorly and laterally. The mid-ventral plates contact with the pterygoid posteriorly, thus excluding the palatines from the margins of the interpterygoid vacuity.

Ethmoid

The sphenethmoid is a median ossification that consists of a sheet-like septum, the mesethmoid, ventrally and anteriorly (lateral wall *sensu* Araújo et al., 2017) and a semi-tubular region, the orbitosphenoid, posterodorsally which descends into to form the presphenoid (Fig. 3). The lateral wall of the ethmoid contacts the vomer and the cultriform process of the parabasisphenoid ventrally, the frontal dorsally, and it might have contacted the nasal, but the latter is badly preserved in GPIT-PV-60758 (Fig. S3). In lateral view, the ethmoid is narrow ventrally and widens towards the top (Fig. 3A, B). Its dorsalmost part contacts the descending process of the frontal and contributes to the ventral part of the sagittal septum that divides the olfactory bulbs (Fig. 2A, B). This anterodorsal part of the ethmoid appears to be homologous to the *crista*

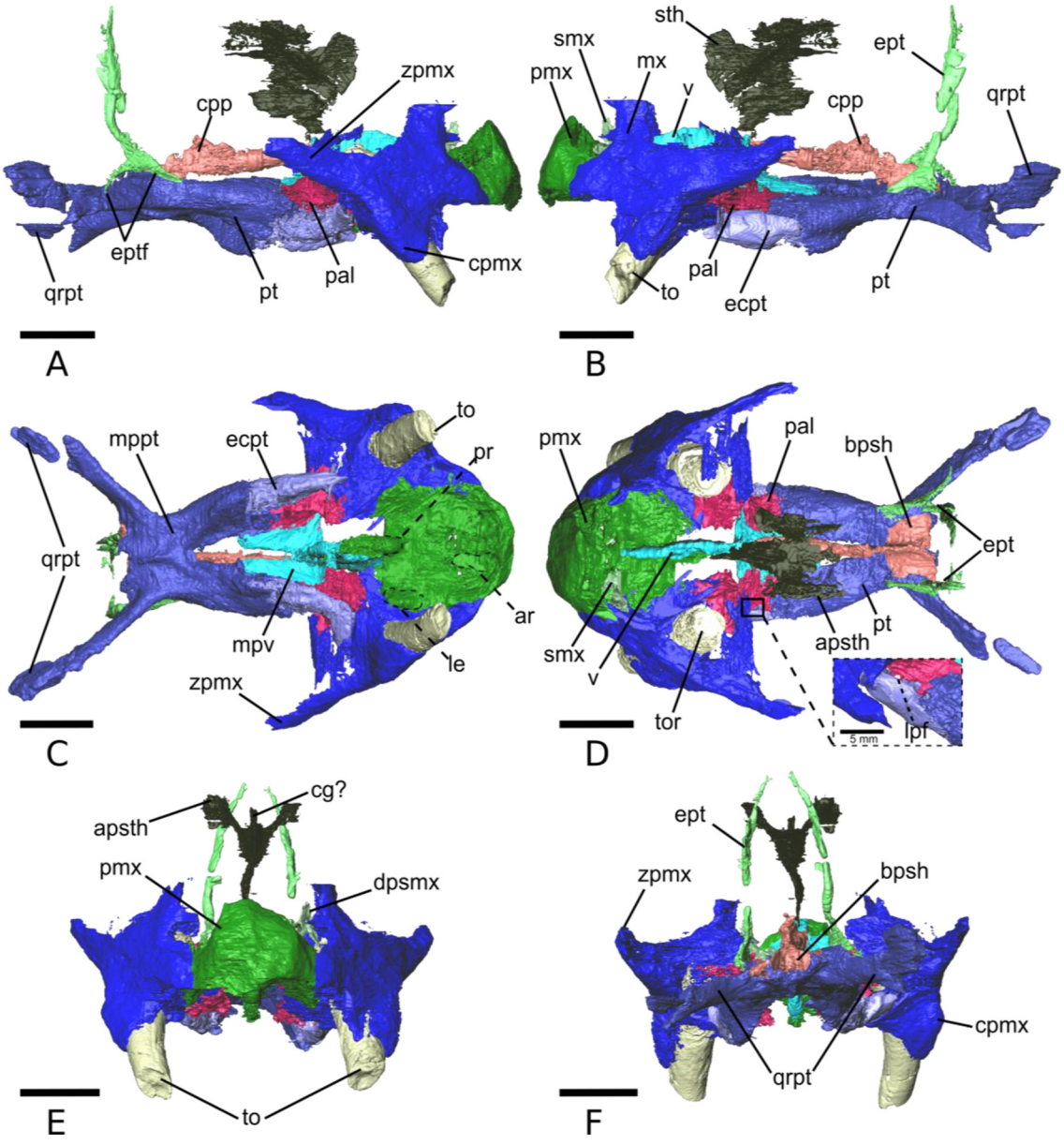

FIGURE 3. Palate and lateral wall. Lateral right and left (A, B), dorsal (C), and ventral (D) views. apsth - ascending process of the sphenethmoid; bsph - basipresphenoid; cpmx - caniniform process of the maxilla; cg - mesethmoid, or "*crista galli*?"; cpp - cultriform process of the parasphenoid; ecpt - ectopterygoid; ept - epipterygoid; eptf - epipterygoid foot; mppt - median plate of the pterygoid; mvp - mid-ventral plate of the vomer; mx - maxilla; pal - palatine; pmx - premaxilla; qrpt - quadrate process of the pterygoid; smx - septomaxilla; sth - sphenethmoid; to - tooth; tor - tooth root; v - vomer. Dashed lines point anatomical structures. Scale bar = 10 mm.

galli of the mammalian ethmoid (Bird et al., 2014). The semi-tubular region of the ethmoid forms a vacuity that housed the olfactory tract (Figs. 3 and 7). It consists of two ascending processes that project laterally to contact the frontal (Figs. 2A, B, and 3). In contrast with the ascending processes in *Niassodon mfumukasi* (Castanhinha et al., 2013), those in GPIT-PV-60758 are not inflected dorsomedially.

Palatine

The palatine can be divided in two anatomical subunits (Fig. 3C): the anterior section (maxillary flanges) and the posterior section (palatine pad *sensu* Castanhinha et al., 2013). The palatines do not contact in the midline due to the presence of the vomer (Fig. 3C, D). They contact the maxilla anteriorly, the ectopterygoid and pterygoid laterally and

posteriorly, and the vomer medially. The maxillary flanges are wider dorsally than ventrally and present a medial concavity that forms the lateral walls of the choanae (Figs. 3C, D and S4C). They are comparatively wider than the palatine pad. Laterally, the palatine presents a subtriangular dorsolateral projection (Figs. 3C and S4A, B). The anterior margin of the maxillary flange of the palatine receives the medial processes of the maxilla (Fig. 3D). The anterior contact between the palatine and the premaxillae is prevented by these medial processes. In lateral view, the posterior portion of the maxillary flange transitions to the palatine pad. The palatine pad contacts the ectopterygoid laterally. It displays a dorsolaterally projecting shelf that is limited anteriorly by the maxilla, and medially by the vomer. The lateral palatal foramen (lpf) is present between the palatal pad and the ectopterygoid suture, just posterior the triple junction between the maxilla, the palatine and the ectopterygoid (Fig 3F). In dorsal view, the pterygoid invaginates the margin of the palatine, forming a hemicircular suture. A posterior projection of the palatine borders the anteromedial margin of the pterygoid (Fig. 3C, D). Medially, the palatines contact the vomer along a scarf joint.

Ectopterygoid

The ectopterygoids are relatively small elements that connect the palatal processes of the pterygoid to the maxilla (Fig. 3). They also contact the palatine dorsolaterally and anterodorsally. The ectopterygoids are ellipsoidal in cross-section, being broadest posteriorly at the contact with the pterygoid. In ventral view, the ectopterygoids are thinnest anteriorly, having a similar shape to the pterygoid at the its suture. The right ectopterygoid presents a small keel along the posterior half of its ventral margin that is contiguous with a similar structure on the ventral surface of the pterygoid (Fig. 3D). In other dicynodonts (e.g., Castanhinha et al., 2013; Sullivan and Reisz, 2005), an elongated lateral palatal foramen is present between the ectopterygoid and the palatine. However, this perforation is not preserved in GPIT-PV-60758.

Pterygoid

The pterygoid is composed of three distinct parts: the anteriorly projecting palatal rami, the median plate, and the posteriorly projecting quadrate rami (Fig. 3). The pterygoid contacts the ectopterygoids anteriorly, the palatine anterodorsally, and the vomer anteromedially, the parabasisphenoid posteriorly and dorsally at the median plate of the parabasisphenoid cultriform process, the epipterygoids dorsally at nearly midpoint of the anteroposterior extension of the bone, and the quadrate, the squamosal, and the opisthotic posteriorly (Figs. 2 and 3). The palatal rami of the pterygoid are robust and increase slightly in height and width anteriorly. They project anterolaterally, making an angle of ~26º with the median plate, giving a V-shape to the anterior part of the pterygoid (Fig. 3D). The palatal processes of the pterygoid contacts the palatines anterodorsally, whereas the ventral part of its anterior portion interdigitates with the ectopterygoid. The ventral edge of the palatal processes bears the pterygoid keel that is continuous with the ectopterygoid (Fig. 3D). Two ventral ridges extend posteriorly from the pterygoid keels, converging at the anterior margin of the median plate to form the *crista oesophagea* (Fig. 3D). The palatal ramus of the pterygoid contacts the vomer dorsomedially, along the anterior half of the interpterygoid vacuity. The palatal processes and the median plate of the pterygoid frame the remaining posterior half of the interpterygoid vacuity. This vacuity narrows posteriorly, as the palatal rami converge towards the median plate, forming a somewhat elliptical posterior half. The median plate is relatively short, representing about one third of the total length of the pterygoid. Posteriorly, most of the median plate dorsal surface is covered by the anterior flange of the parabasisphenoid . The epipterygoids rest along the dorsolateral edge of the median plate and the dorsal margin of the anteriormost part of the quadrate rami of the pterygoid. Posteriorly, the quadrate rami are mediolaterally compressed and project posterolaterally, making an angle of approximately 40º with the median plate. They reach the posteriormost region of the skull, wedging between the medial surface of the quadrates, the ventrolateral margin of the opisthotics, and the ventromedial edges of the ventral processes of the squamosal.

Epipterygoid

The epipterygoids are paired elements consisting of a rod (ascending ramus) and a footplate that connects the pterygoid to the descending flange of the parietal (Figs. 2 and 3). Ventrally, the epipterygoid consists of a footplate that originates at the level of the most anterior point of the pterygoid-basipresphenoid suture and extends posteriorly, resting on the posterior quadrate rami of the pterygoid (Fig. 3A, B). In lateral view, the footplate is C-shaped, presenting a flattened

portion anteriorly (Fig. 3A, B). The rod-like ascending ramus of the right epipterygoid has a posterior inclination (~53°) near its junction with the footplate, but then becomes more vertical. The left epipterygoid is closer to vertical for its entire length.

Cultriform process of the parasphenoid and basipresphenoid

The cultriform process is elongated and mediolaterally compressed, and it contacts the vomer anteriorly, the ethmoid anterodorsally, and the basipresphenoid posteriorly (Fig. 3). The cultriform process is tall as it projects from its insertion on the basipresphenoid, but becomes progressively lower anteriorly. The dorsal groove of the vomer receives the anterior projection of the cultriform process. A groove opens on the dorsal surface of the cultriform process near its midlength and continues to the contact with the vomer, corresponding to the vidian canal. In our specimen, the anteriormost part of this groove receives the sphenethmoid. The remaining space is probably for the insertion of the anterior braincase wall (e.g., possibly the unpreserved orbitosphenoid). Posteriorly, the cultriform process (parasphenoid) coossifies with the broad basispres-phenoid (Fig. 3C, F; Fig. S5). The basipresphenoid is rectangular in dorsal view, being housed on a deep concavity on the dorsal surface of the median plate of the pterygoid (Fig. 3C). The basipresphenoid is anterodorsally thick and presents a spongious internal structure (Fig. S5). Posteriorly, it contacts the parabasisphenoid (parasphenoid + basipres-phenoid) and contributes to the anterior margin of the internal carotid canal.

Skull roof

Nasal

The nasals are located anterodorsally in the skull (Figs. 2, 4), but are poorly preserved in GPIT-PV-60758. The nasal is a dome-shaped bone that contacts its counterpart in the sagittal midline, the premaxilla and the maxilla ventrally, and the prefrontal posterolaterally. The ventral part of the left nasal is not preserved. The posterodorsal portion and most of the midline of both nasals are also not preserved. The most posterior part of the internasal suture presents an interdigitating pattern (Fig. S6). In lateral view, the anterior margin is flat, with a small boss anterodorsally (Fig. 4A).

Prefrontal

The prefrontals form the anterodorsal part of the orbital margin and part of the orbital wall between the lacrimal and the frontal (Fig. 4). The left prefrontal is poorly preserved in this specimen, consisting only of the anteriormost part of the lacrimal and nasal contacts and a small fragment of its posterior contact with the frontal (Fig. 4C). The right prefrontal is more complete and contacts the nasal anteriorly, the lacrimal anteroventrally, the frontal posteriorly and the anterior tip of the dorsolateral wing of the sphenethmoid just ventral to the anterior margin of the frontal (Fig. 2B). The prefrontal is a small element that is widest near the contact with the lacrimal and tapers posterodorsally. A small dorsomedial projection of the bone is present, but it is worn, as is most of the dorsal surface between the frontal and the nasal. In cross-section, the prefrontal is thin medially and ventrally, thickening dorsolaterally at its contribution to the orbital margin (Fig. S7). This section reveals a concavity on the medial surface, with the dorsomedial projection forming an angle of about 90° with the lateral part of the bone. (Fig. S7).

Lacrimal

Both lacrimals are present in this specimen, but only the right element presents a well-preserved external surface (Fig. 4). The lacrimal abuts on the anterodorsal part of the maxilla, slightly dorsal to the caniniform process (Fig. 2A, B). The lacrimal also contacts the jugal posteroventrally along a mediolaterally-oriented suture, the prefrontal dorsally, and the nasal anterodorsally. The lacrimal is the anteriormost element of the orbital wall and orbital margin. In lateral view, it presents a subtriangular shape, with a slightly concave and anteriorly-inclined posterior margin (Fig. 2A, B). The lateral surface of the lacrimal presents a small posterior ridge, oriented dorsoventrally, that corresponds to the orbital rim (Fig. 2A, B). Anteriorly, the lacrimal makes a small contribution to the lateral surface of the snout. The posterior surface of the lacrimal extends from the lateral edge of the orbit to its medialmost extension. It displays a relatively large lacrimal foramen (1.3 mm diameter) just medial to its lateral margin (Fig. 4C). The dorsomedial surface of the lacrimal is the roof of a large maxillary sinus. This sinus is connected to the orbit by the lacrimal duct that opens into the lacrimal foramen.

Frontals

The frontal is a flat bone that is elongated anteroposteriorly, and represents 40% of the condylobasal length and about 50% of the skull width (Fig. 4). It contacts the prefrontals anteriorly, the sphenethmoid anteroventrally, the postfrontal posterolaterally, and the postorbital, the prearietal, and the parietal posteriorly (Figs. 2, 4). The anterior part of the frontal is not preserved in this specimen and, therefore, the contact with the nasal is not present. In dorsal view, the frontal is roughly rectangular, being slightly expanded at its midlength. The dorsal surface presents no ornamentation, although this might be due to preservation. The frontal anterolateral margins form the dorsal part of the orbital edge, being limited anteriorly by the prefrontal. The posterior portion of the frontal is split in two halves that receive the prearietal and partially overlap its anterior end. The posterior margin of the two portions of the frontal that encircle the prearietal are bordered by the anterior margin of the parietal (Fig. 4C). Anteriorly, the ventral surface of the frontal presents a shallow excavation limited anteriorly by a median descending process that delimits the dorsal part of the olfactory tract (dpf, Fig. 4B). The descending process of the frontal contacts with the most dorsal projection of the sphenethmoid (Fig. 2).

Postfrontals

The postfrontal is well preserved on the right side of the skull roof (Fig. 4). This bone is triangular in dorsal view (Fig. 4C). The postfrontal contacts the frontal medially, the postorbital laterally, and presents a narrow contact with the parietal posteriorly (Fig. 4C). Its wider anterior margin contributes to the dorsal part of the orbital margin, filling the small gap between the frontal and the postorbital bar (Fig. 4B, C). The postfrontal narrows from the orbit to the frontal-postorbital contact, posteriorly.

Prearietal

The prearietal is a narrow, anteroposteriorly elongated bone bordered by the frontal anteriorly and laterally, and by the parietal posteriorly (Fig. 4). In dorsal view, the prearietal is subrectangular and its surface is flush with the dorsal surface of the frontal and the parietal. Its anterior margin is roughly rectangular and is covered by the frontal. In dorsal view, the exposed anterior margin of the prearietal is ellipsoidal whereas the posterior margin bifurcates (Fig. 4C). It surrounds the anterior and lateral margins of an ellipsoidal pineal foramen. The prearietal bifurcations fused with the parietal, hindering the observation of the simple butt joint with the parietal. In lateral view, the prearietal thickens anteroposteriorly. The dorsal surface of the prearietal is flat and does not form a pineal boss (Fig. 4C). In ventral view, the prearietal develops considerably under the frontal (Fig. 4B).

Parietal

The parietal is a subrectangular bone with concave edges that forms a narrow and crest-like temporal bar (Fig. 4). It is bordered anteriorly by the frontal and the prearietal, laterally by the postorbital and postfrontal, ventrally by the epipterygoids, and posteriorly by the squamosal and the postparietal (Fig. 2). It likely would have contacted the tabulars as well (Sullivan and Reisz, 2005), but they are not preserved . The narrow dorsal exposure of the parietals presents two temporal lines forming a small crest along the interparietal suture (Fig. 4C). This crest is wide anteriorly and sharpens posteriorly, flattening anteriorly to the contact with the postparietal bone (Fig. 4C). The ventral surface of the parietals presents two median ridges that originate from posterior margins of the pineal foramen (Fig. 4B). These ridges project ventrolaterally in a more posterior position, forming the descending flanges of the parietals (Fig. 4A). The lateral surface of the descending flange corresponds to the attachment area of the temporal musculature. The two median ridges converge into a single median structure posterior to the contact with the epipterygoids (Fig. 2A, B). Posteriorly, the ridge bifurcates and projects laterally as the descending processes of the parietal, bordering the ventrolateral surface of the postparietal (Fig. 4B, C). Internally, the parietals bear thin laterally-projecting shelves that are overlain by the temporal portions of the postorbital. Two slender posteroventrally-projecting processes probably contacted the squamosal posteromedially, although the processes are badly preserved. Medially, the postparietal lies on the posterior portion of the parietal (Fig. 4B, C). The cross section of the parietals presents a flat dorsal surface anteriorly, and the descending flanges are close to perpendicular to the shelves that underlie the postorbitals. At the level of the epipterygoid contact, the cross section of the parietal presents a broad ridge dorsally and the descending flanges describe an angle of approximately 53^{o} with the skull roof (Fig. S6B, C). At the posterior end of the parietal, the skull roof component thickens and the attachment area for the temporal

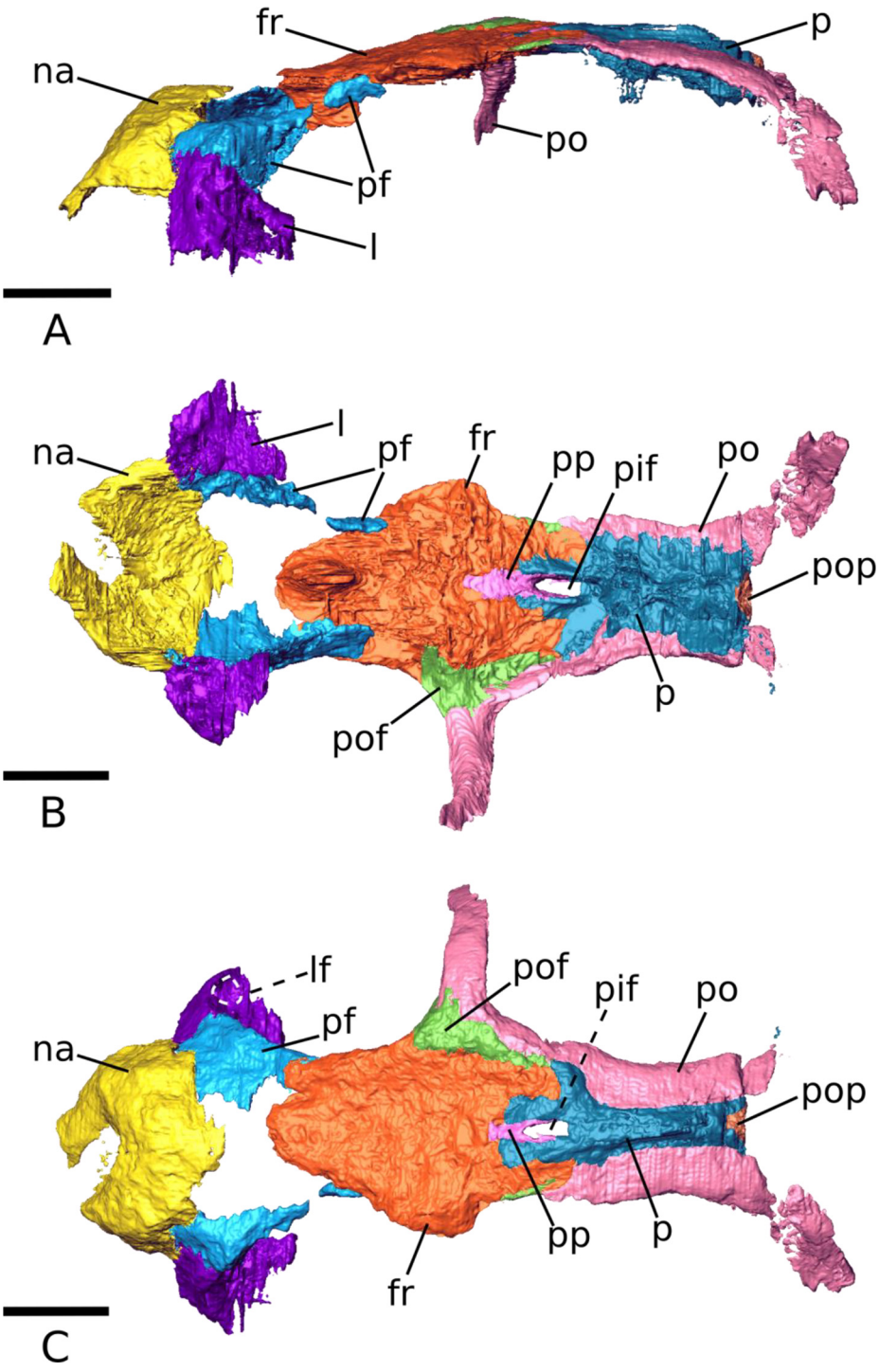

FIGURE 4. Skull roof. Lateral left (A), ventral (B), and dorsal (C) views. fr - frontal; l - lacrimal; lf - lacrimal foramen; na - nasal; p - parietal; pf - prefrontal; pif - pineal foramen; po - postorbital; pof; postfrontal; pop - postparietal; pp - preparietal. Dashed lines point anatomical structures. The lacrimal foramen is outlined in dashed white. Scale bar = 10 mm.

musclulature becomes rounder, with the descending flanges describing an angle of approximately 58°. The cross sections show the interdigitating suture between the left and right parietal along its anteroposterior length.

Postparietal

The postparietal is a small wedge-like element on the posterior part of the skull roof (Fig. 4). It is harboured by a concavity formed on the posterior margin of the paired parietals, just posterior to the interparietal suture (Fig. 4B, C). The postparietal likely contacted most of the supraoccipital ventrally, and the dorsal tips of the tabulars (e.g., Sullivan & Reisz, 2005). The preserved bone is subtriangular in dorsal view (Fig. 4C). It is anteroposteriorly short and its height is similar to that of the parietals.

Postorbitals

The right postborbital is almost completely preserved in GPIT-PV-60758 (Fig. 4). The anterior postorbital process of the left side bone is not preserved, although its most posterior tip is better preserved than on its right side. The postorbital consists of two parts, the thin postorbital process and a posterior sheet that overlays on the lateral shelf of the parietal, reaching the squamosal posteriorly. The postorbital process is curved and concave medially (Fig. 4C). The postorbital contacts the dorsal process of the jugal ventrally, overlapping its lateral surface (Fig. 2A, B). The postorbital also contacts the postfrontal dorsally, thus connecting the skull roof with the subtemporal bar. The dorsal part of the postorbital presents a long sheet-like posterior projection that borders the lateral edge of the postfrontal. A contact between the postorbital and the frontal is prevented by the narrow posterior extension of the prefrontal and the anterolateral projection of the parietal (Fig. 4B, C). The temporal portion of the postorbital rests on the lateral shelves of the parietal and borders the dorsal exposure of the parietal medially (Fig. 4B, C). The temporal portion of the postorbital is thin medially and increases in thickness laterally. Posteriorly, the temporal portion of the postorbital reaches the dorsal process of the squamosal, and it also likely contacted the tabular (Sulivan and Reisz, 2005).

Occipital and zygomatic regions

Jugal

The jugal can be divided into a broad anterior part and a narrower posterior process that contributes to the zygomatic arch (Fig. 2). Here, we focus on the right jugal due to its better-preserved anatomy (Fig. 2D). The bone contributes to the lateral border of the orbital wall anteriorly, where it broadly contacts the lacrimal dorsally and the maxilla medially and laterally (Fig. 2D). A small ventral contact with the ectopterygoid is also present, and the jugal contacts the postorbital dorsomedially. The posterior process of the jugal forms much of the medial surface of the zygomatic arch and contacts the anterior process of the squamosal along a scarf joint (Fig. 2D). The anterior portion of the jugal presents a medial projection, overlapping the dorsal contribution of the maxilla to the orbital wall (Fig. 2D). On the right side, the CT scan sections show the jugal contribution to the posterolateral wall of the caniniform alveolus. Anterior to this region, the jugal is hollow until it forms the medial surface of the compact suborbital bar. The suborbital bar is subcylindrical in section posteriorly, becoming elliptical as it approaches the postorbital bar, where the major axis is almost aligned with the sagittal plane. Here the bone becomes broader, with a transversely compressed dorsal process contributing to the ventromedial part of the postorbital bar that is complemented, dorsolaterally, by the descending process of the postorbital (Fig. 2D). A badly preserved posterior process extends posteriorly from the medially concave posterior ramus of the jugal to join the anterior process of the squamosal, forming the subtemporal bar (Sullivan & Reisz, 2005).

Squamosal

The squamosal has a complex shape consisting of dorsal, zygomatic, and ventral processes (Fig. 5). It contacts the parietal and the postorbital dorsally, the jugal anterodorsally, the maxilla anteriorly, the supraoccipital and the opisthotic medially, and the quadrate-quadratojugal complex ventrally (Fig. 2, 5). The zygomatic process of the squamosal consists of an anteriorly projecting zygomatic/anterior branch that articulates with the lateral surface of the jugal and is overlain laterally by the zygomatic process of the maxilla just anterior to the postorbital bar (Figs. 2 and 5A-D). Dorsally, the anterior process contacts the descending flange of the postorbital. The zygomatic process widens posteriorly, forming the flat and wide dorsal surface of the ventral process. Ventrally, the strongly concave lateral surface of the ventral process of the squamosal represents the origin of the lateral external adductor musculature (Fig. 2A, B, 5A, B, King, 1989). The medialmost part of the dorsal process probably contacted the tabular (Sullivan & Reisz 2005), although the latter element is not preserved in our specimen. The dorsal process of the

squamosal contacts the supraoccipital ventromedial to the parietal flange (Fig. 5F). The squamosal narrows ventrally and acquires a more columnar shape in the transition between the dorsal and the ventral process of the bone (Fig. 5E). At mid-height, the squamosal contributes to the lateral margin of the posttemporal fenestra, with the supraoccipital limiting the fenestra dorsomedially and the opisthotic forming its ventromedial corner (Fig. 5E, F). The squamosal widens to form the ventral process that contacts the opisthotic medially and presents a concavity anterolaterally that receives the quadrate-quadratojugal complex (Fig. 5E). Ventrally, the squamosal narrows in medial view, presenting a flattened posterior surface. Anteriorly, the ventral margin of the ventral process projects slightly anteriorly and presents a fossa that receives the dorsal process of the quadrate. The lateral surfaces of both right and left squamosals are badly weathered (Fig. 5C, D). The dorsal process of the squamosal contacts a thin posteroventral projection of the parietal and the overlying posterior process of the postorbital.

Quadratojugal

The quadratojugal is a sheet-like bone that covers the lateral surface of the ventral process of the squamosal (Fig. 5 A, B). Ventrally, this element contacts the lateral margin of the dorsal process of the quadrate, which is best preserved on the right side of GPIT-PV-60758. The medial surface of the ventral portion of the quadratojugal, which is preserved on the left side only, forms the lateral margin of the quadrate foramen. In lateral view, the quadratojugal is subrectangular, being wider dorsally.

Quadrate

The quadrate is characterized by a large dorsal process and two ventral articular condyles, one projecting medially and the other projecting laterally (Fig. 5). The quadrate contacts the squamosal dorsally and dorsomedially, the quadratojugal dorsolaterally, and the quadrate ramus of the pterygoid dorsomedially. The quadrate receives the posterior portion of the articular process on an anteroposteriorly-oriented articular facet. In lateral view, the quadrate is subrectangular, with its anterodorsal surface being posteriorly inclined in relation to the coronal plane. The posterior part of the quadrate is characterized by an oval-shaped dorsal process presenting a flat posterior surface (Fig. 5E). In dorsal view, the dorsal process of the quadrate slants laterally, with its medial and posterior surfaces articulating with the squamosal. The lateral surface of the dorsal process of the quadrate is overlain by the ventral portion of the quadratojugal (Fig. 5E). The anterior aspect of the dorsal process of the quadrate presents an anterolaterally-facing concavity (Fig. 5E). The lateral edge of this concavity and the dorsal edge of the lateral articular condyle contribute to the medial margin of the quadrate foramen (Fig. 5E). The medial articular condyle is antero-posteriorly longer than the lateral one. The latter presents a slightly grooved posterior surface that forms the lower ventral surface of the quadrate foramen.

Parabasisphenoid (parasphenoid+basipostsphenoid)

The parabasisphenoid comprises the floor of the braincase between the pterygoid and the basioccipital, as well as the anterodorsally projecting cultriform process (Figs. 3 and 5). As in other dicynodonts (Castanhinha et al., 2013), the posterior portion of the parasphenoid and the basipost-sphenoid are fused (Araújo et al. 2017). Here these two structures are referred to as a single coossified element, the parabasisphenoid (Fig. 3 and 5). We make an anatomical distinction with the more anterior cultriform process and basipresphenoid, despite resulting developmentally from the fusion of the basipresphenoid to the parasphenoid (Araújo et al. 2017). The parabasisphenoid contacts the pterygoid and the basipresphenoid anteriorly, the basioccipital posteriorly, and the prootics posteroventrally. In ventral view, the para-basiphenoid is subtriangular, having a wide posterior margin and tapering anteriorly (Fig. 5C). Its ventral margin is characterized by the presence of two lateral buttresses that form the anterior part of the ventrolaterally projecting tubera, together with the ventrolateral projections of the basioccipital. The tubera present laterally exposed stapedial facets. The tubera flank a medial flat surface and their anterior edges form anterodorsally-sloping ridges, creating a medial excavation that continues anteriorly to the base of the cultriform process (Fig. 5C). The ventral surface of the parabasisphenoid slopes anteriorly, from a highpoint on the tubera to the median pterygoid plate (Fig. 5C). The parabasisphenoid dorsal surface bears two depressions adjacent to the suture with the basioccipital (Fig. 5D). These depressions are anteromedial to the foramen ovale and are separated by a small crest that extends from the contact with the basioccipital to near the midpoint of the parabasisphenoid (Fig. 5D). Laterally, the parabasisphenoid presents two anteromedially converging

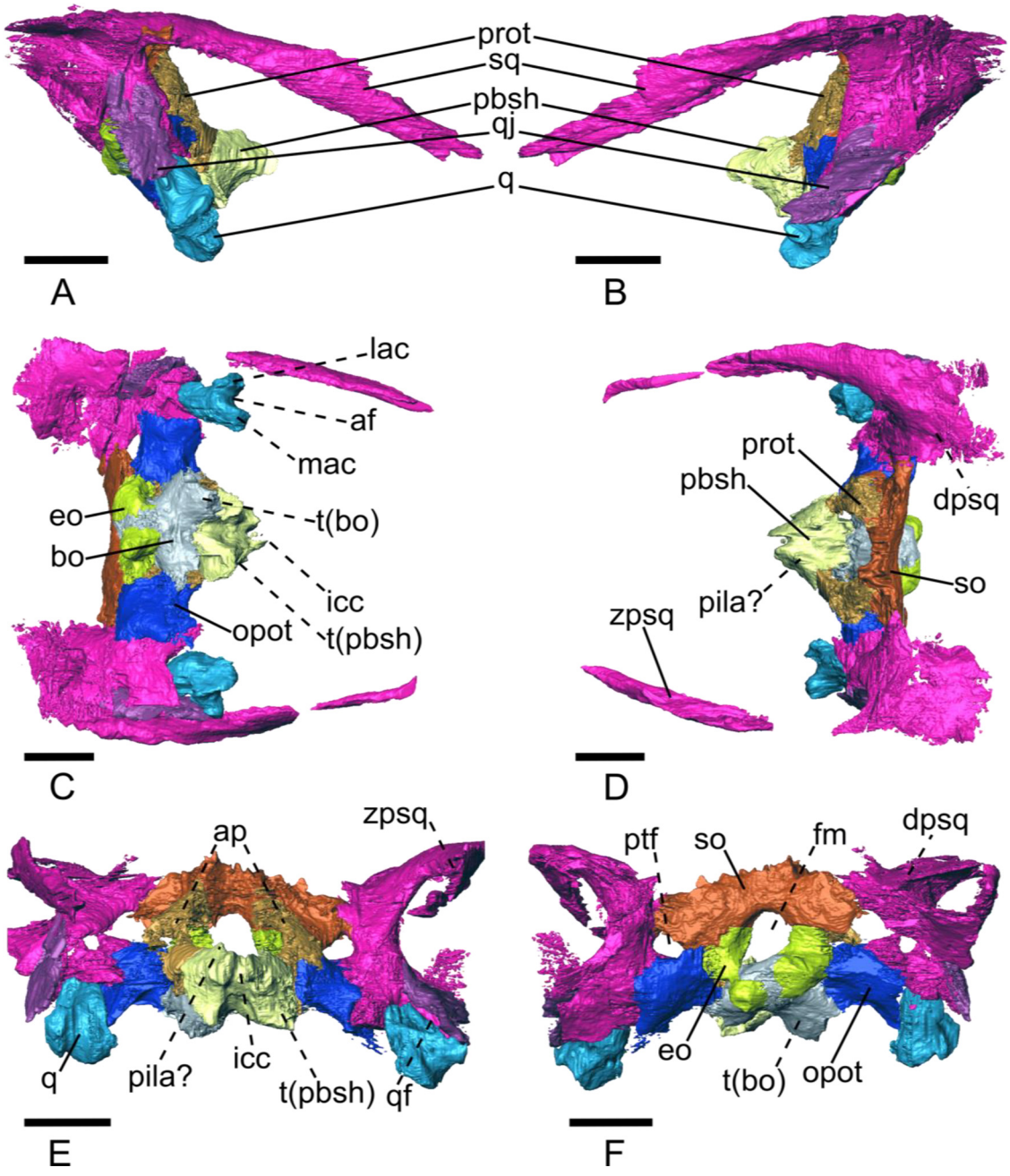

FIGURE 5. Occipital and zygomatic regions.The skull is shown in right and left lateral views (A, B), ventral (C), dorsal (D), anterior (E) and posterior (F) views. Af - articular facet; ap - ascending process of the prootic; bo - basioccipital; dpsq - dorsal process of the squamosal; eo - exoccipital; fm - foramen magnum; icc - internal carotid canal; lac - lateral articular condyle; mac - medial articular condyle; opot - opisthotic; pila - *pila antotica*; prot - prootic; pbsh - parabasisphenoid; ptf - posttemporal fenestra; q - quadrate; qf - quadrate foramen; qj - quadratojugal; sq - squamosal; t - tuber; zpsq - zygomatic process of the squamosal. Dashed lines point anatomical structures. Scale bar = 10 mm.

crests that appear to correspond to the parabolic crests (Araújo et al., 2017). The parabolic crests are continuous with the anterior projections of the prootics, and the ossification of the *pila antotica* might have rested on their anterior portions (Fig. 5D). The parabolic crests flatten out just posterior to the suture with the pterygoid, where they abut the basipresphenoid. The internal carotid foramen opens on the median part of the parabasisphenoid-basipresphenoid

suture (Fig. 5C, D). Ventrally, the internal carotid canal bifurcates (see "Brain Endocast").

Basioccipital

The basioccipital is the ventral element composing the posteriormost part of the braincase floor (Fig. 5). The basioccipital contacts the exoccipitals dorsolaterally, the opisthotics laterally and the parabasisphenoid anteriorly. This bone makes up the ventral part of the foramen magnum and presents a posteriorly-projected protuberance, part of the occipital condyle. The occipital condyle is typically composed of a median knob, located ventrally and formed by the basioccipital, and paired lateral knobs that flank it dorsally (Sullivan and Reisz 2005). The condyle in GPIT-PV-60758 is damaged: only the central portion of the basioccipital knob is preserved, the right exoccipital knob is mostly present, and only a fragment of the left exoccipital knob remains. Anteriorly, the ventral surface of the basioccipital presents two ventral tuberosities that fuse with the posterior part of the parabasisphenoid tubera. These tuberosities project ventrolaterally and partially enclose the *fenestra ovalis*. We follow Sullivan and Reisz (2005) and call these prominences the "ventrolateral tubera". The basioccipital contacts the opisthotics along the dorsal margins of the tubera ventrolateral to the jugular foramen. Medial to the ventrolateral tubera, the basioccipital presents a flat region that continues anteriorly to the parabasisphenoid. The basioccipital contributes to the posterior margin of the *fenestra ovalis*, with the anterior margin being composed by the parabasisphenoid, to which both bones contribute in equal proportions, with the opisthotic contributing to a small portion of the margin dorsolaterally (Fig 5C, F). The basioccipital also contributes to the lateral and dorsal margin of the jugular foramen.

Interparietal + tabular

The occipital region of GPIT-PV-60758 is damaged, as indicated by the absence of the dorsalmost part of the supraoccipital and the posterior part of the right postorbital (Fig. 2). Because of this damage, the interparietal and the tabulars are not preserved in this specimen.

Supraoccipital

The supraoccipital is badly preserved in GPIT-PV-60758, with most of its dorsal and anterodorsal parts broken off (Fig. 5C-F). The supraoccipital delimits the foramen magnum dorsally, and it is bordered by the squamosals laterally. It also contacts the prootics anteroventrally, and the exoccipitals posteroventrally. Dorsally, a gap between the supraoccipital and the parietals represents the space for the interparietal and the tabulars, with the supraoccipital originally contacting these dorsally (Sullivan and Reisz, 2005). Anterodorsally, the supraoccipital preserves a small flange on the right side that appears to contribute to the lateral wall of the braincase, and it encloses the bony labyrinth dorsally. The external surface of the supraoccipital is better preserved on the left side of the skull, where it contacts the ventralmost portion of the squamosal dorsal process laterally and the exoccipital ventrally. The supraoccipital lateral extensions contribute to the dorsomedial margins of the posttemporal fenestra (Fig. 5F).

Exoccipital

The exoccipitals are two small elements that contribute to the lateral margins of the foramen magnum (Fig. 5C, F). They are bordered by the supraoccipital dorsally, the prootics anteriorly, the opisthotic ventrolaterally and the basioccipital ventromedially. In GPIT-PV-60758, the left exoccipital is better preserved than the right. Our segmentation shows that the exoccipitals contribute to the dorsolateral swelling of the occipital condyle, which is visible only on the left side of the specimen because the right side of the occipital condyle is not preserved. The exoccipital contributes to the dorsal margin of the jugular foramen, which is located between the exoccipital, the basioccipital ventromedially and the opisthotic ventrolaterally. The anterodorsal surface of the exoccipital contributes to the wall of the floccular fossa.

Opisthotic

The opisthotics form the ventrolateral part of the braincase and are subrectangular in posterior view (Fig 5). The left opisthotic is better preserved in GPIT-PV-60758, and it will be the focus of this description. The opisthotic forms the paroccipital process between the occipital complex and the squamosal, and it also bears an anterior projection that reaches the posterolateral portion of the parabasispenoid and contacts the ventral margin of the prootic (Fig. 5C, D). The opisthotic and the prootic are strongly coossified and their suture is hard to trace (Fig. 5E). The opisthotic also contacts the supraoccipital dorsally (Fig. 5F). The opisthotic contributes to the lateral margin of the *fenestra ovalis* ventromedially, and it makes up the lateral margin of the jugular foramen

medially. Our description matches that of Sullivan & Reisz (2005), which defines the jugular foramen as being located between the opisthotic, the exoccipital and the lateral knob of the occipital condyle. The opisthotic also contributes to the ventral margin of the posttemporal fenestra (Fig. 5E, F). The contact between the opisthotic and the squamosal is large, covering the entire medial surface of the squamosal ventral to the posttemporal foramen. Medially, the opisthotic forms the lateral wall of the otic capsule, enclosing the lagena of the inner ear.

Prootic

The prootics are paired elements located anterolateral to the foramen magnum (Fig. 5A, B, D, E). They enclose the semicircular canals and compose the anterior, dorsal and lateral walls of the recesses that house the lobes of the floccular complex of the cerebellum (fcl; fcl fossae). The prootic contacts the parabasisphenoid anteroventrally, the opisthotic ventrolaterally, the supraoccipital posteriorly, and the exoccipital posteroventrally. The sutures with the opisthotic and the supraoccipital are particularly well-resolved, and correspond to most of the sutural area of these bones. The prootic is subtriangular in lateral view. The anterior margin of the prootic is slightly curved, reflecting the shape of the anterior semicircular canal that it encloses. The ascending process of the prootic likely fuses with the epiotic, a bone that usually coossifies with the prootic at the level of the suture with the supraoccipital (Jollie, 1960). The epiotic could not be discriminated as a distinct element. The prootic (+epiotic) and the opisthotic are part of the periotic complex, a group of structures homologous to the petrosal of modern mammals. In dicynodonts, including other specimens of *Diictodon*, the prootics normally present a pila antotica anteriorly, an element that projects dorsally and that is part of the braincase wall. However, this element is not preserved in GPIT-PV-60758. The medial surface of the left prootic presents a large fossa that housed the floccular complex lobe, posteriorly. This structure is not preserved on the right element.

Mandible

Dentary

The dentary is the largest and best-preserved element of the mandible, although the anteriormost tip is relatively worn compared to the rest of the bone (Fig. 6). In lateral aspect, the dentary presents a rounded upturned beak at the level of the symphysis (Fig. 6A, B, C). The bone increases in height as the anterior margin descends steeply (53^{o} with the occlusal plane). The dentary reaches its maximum height at approximately one third of its total length. It then gradually becomes slender posteriorly. The ventral margin of the dentary is convex anteriorly, just posterior to the symphysis, but becomes slightly concave anterior to the ascending ramus (Fig. 6A, B). The dentary does not present a strong lateral dentary shelf, but a shallow trough running posterodorsally-anteroventrally (oblique line) marks the anterior border of a blunt dentary swelling (dsw, Fig. 6A, B). In dorsal view, the hemimandibles diverge at an angle of 47^{o}, measured from the anteriormost part of the beak to the posteriormost part of the rami. The anterior part of the dentary is characterized by the up-turned symphysis (Fig. 6C). The anterior edge of the dentaries presents two small swellings that form dorsal bony protrusions (bp, Fig 6C), each of which continue posteriorly as a ridge (dentary blades) that borders the dentary table medially. The dentary blades (dbl, Fig. 6C) are antero-posteriorly oriented, parallel to the dentary tables (dta, Fig. 6C). The latter are transversely excavated and present foramina that appear to connect to the mandibular canal (Fig. S8). These structures appear to resemble the *dorsal canaliculi* described in mammals (Ferreira-Cardoso et al., 2019). In GPIT-PV-60758, the dentary table is continuous posteriorly with the small shallow posterior dentary sulcus (pds, Fig. 6C). The posterior part of the dentary blades preoject medially forming small round medial dentary shelves (mds; Fig. 6C). These shelves limit the longitudinal extent of the horizontal ramus, dorsally. The ascending rami project posterolaterally, forming a 40^{o} angle with the anteroposterior axis of the dentary tables (Fig. 6C, D). They narrow posteriorly and their medial surface presents a furrow that houses the anterior part of the surangular (Fig. 6B, D).

Splenial

The splenial is a flattened and elongated bone that covers the ventral part of the dentary medial surface along its entire length (Fig. 6D). Anteriorly, it consists of a medial projection that contacts its bilaterally symmetric counterpart. The intersplenial suture is small but visible (Fig. S9A) on a small ventral concavity on the lingual surface of the dentary symphysis (Fig. 6D). The splenial broadens and thickens

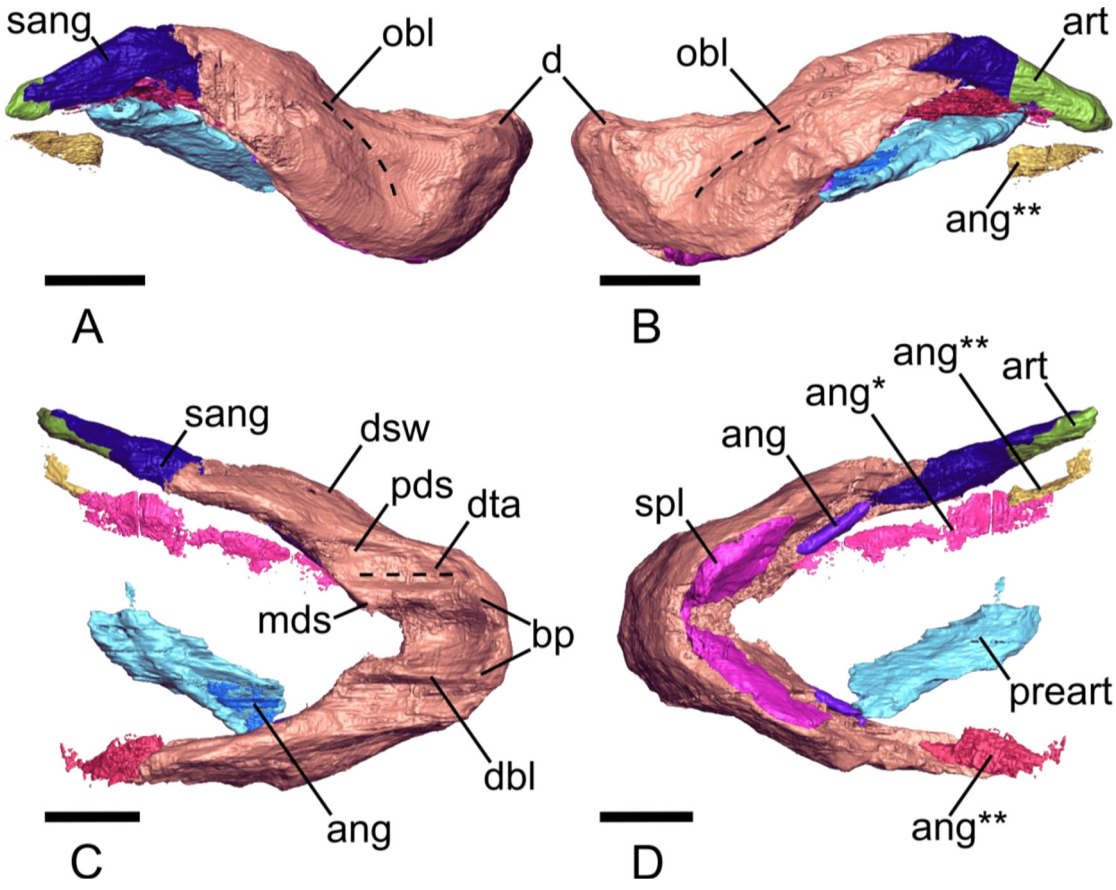

FIGURE 6. Mandible. Lateral right (A), lateral left (B), dorsal (C), and ventral (D) views. * - putative fragments of the angular; ang - angular; art - articular; bp - bony protrusions; d - dentary; dbl - dentary blade; dsw - dentary swelling; dta - dentary table; mds - medial dentary shelf; obl - oblique line; preart - prearticular; sang - surangular; spl - splenial. Dashed lines point anatomical structures. Scale bar = 10 mm.

posteriorly for a short length. Apart from its anterior symphyseal part, the spenial has an elliptical shape in medial/lateral view. The bone is housed by a broad medial dentary recess. At its round posterior margin, the splenial likely contacted the anterior parts of both the angular and prearticular, but they are not well-preserved in our specimen.

Angular

Both angulars are extremely damaged in GPIT-PV-60758 (Fig. 6B-D). The anterior part of the left and right angulars are still attached to the ascending ramus of the dentary, posterodorsal to the splenial (ang, Fig. 6D). In addition to the dentary, the angular probably contacted the splenial, the surangular, and the prearticular. Our reconstruction shows a badly weathered part of the right angular bone attached to the anterolateral surface of the disarticulated prearticular (ang*; Fig. 6D). Several unidentifiable elements putatively belonged to the angular bones (ang**, ang***, ang****; Fig. 6D).

Surangular

The surangular contacts the dentary anteriorly, the articular posteriorly, and in other *Diictodon* specimens, it contacts the angular ventrally (Sullivan & Reisz, 2005). This element forms the dorsal edge of the posterior portion of the mandible (Fig. 6). The right surangular is better preserved whereas the left is a badly preserved fragment located near its articulation with the dentary. The right surangular has a wide V-shape with a ventrally-opening angle. The anterior portion of the surangular rests in a relatively deep descending furrow on the medial surface of the dentary. The anterior half of the surangular is three times longer than high and has a subrectangular anterior tip. The posterior half of the surangular appears to be damaged, as well as the articular-prearticular complex to which it attaches.

Articular-prearticular complex

The articular-prearticular complex is highly damaged in GPIT-PV-60758 (Fig. 6B, D). The articular surface of the left articular bone is preserved. It contacts the medial surface of the posterior part of the surangular. Posteriorly, the articular forms a knob that articulates with the intercondylar groove of the quadrate. The prearticular of GPIT-PV-60758 is represented by the right element only (Fig. 6). It is disarticulated from all the remaining elements of the mandible, except for a badly preserved part of the angular on its medial surface (Fig 6D). The prearticular is a broad, flattened, and anteroposteriorly elongated bone. The poor preservation of the posterior elements of the mandible prevents an accurate description of these bones.

Braincase endocast and bony labyrinth

Brain endocast

The brain endocast is subtriangular in lateral view, with a narrower forebrain anteriorly and a broader hindbrain posteriorly (Fig. 7). The endocast is limited anteriorly by the sphenethmoid and the frontal, with both bones contributing to the olfactory dorsal and ventral walls, respectively. The olfactory bulbs (*sensu* Mammalia) are relatively small, practically nonexistent, and consist of two large-diamter nerves at the most anterior part of the endocast. Posteriorly, these nerves are fused in a mass that corresponds to the olfactory tract (Fig. 7). The olfactory tract and posterior part of the bulbs are wrapped by the ascending processes of the sphenethmoid ventrally and laterally (broadly analogous to the cribriform plate in mammals; Bird, 2014, 2018; Martinez et al., 2020). Posterior to this region, the dorsal surface of the endocast projects dorsally as an elongated and mediolaterally narrow protuberance that corresponds to the pineal foramen (Fig. 7A, B). The ventral part of the endocast between the sphenethmoid and the posterior margin of the pineal foramen is interpolated, as there is no preserved osseous element delimiting the brain in this region. The lateral wall was probably composed of cartilage associated with the *pila metotica* anteriorly and the *pila antotica* posteriorly (Novacek, 1993; Rieppel, 1993; Paluh & Sheil, 2013). Ventrally, the midbrain presents a large hypophysis, which is anteriorly limited by the cultriform process of the parasphenoid (Fig. 7A, C). The ventral margin of the hypophysis presents a projecting cylindrical structure that corresponds to the internal carotid canal (icc, Fig. 7A, C). The internal carotid canal is wide dorsally but splits in two smaller structures on its most ventral part (Fig. 7C). Posterior to the level of the pineal foramen, the dorsal margin of the hindbrain is inclined ventrally, mirroring the orientation of the parietal. Laterally, the width of the endocast is limited by the epipterygoids and the descending flanges of the anterior part of the parietal. Ventrally, the hindbrain is delimited by the basisphenoid anteriorly and the basioccipital posteriorly. The posterior part of the endocast consists of a badly preserved cerebellum, delimited posteriorly by the supraoccipital and the exoccipitals at the posterior portion of the floccular fossae. Laterally, the cerebellum is delimited by the prootics, which form almost the entirety of the walls of the floccular complex lobe (fcl) fossae (e.g., Ferreira-Cardoso et al., 2017). Only the right floccular fossa is well preserved. Cranial nerve V (and the *vena capitis medialis*) can be identified anteroventrally to the floccular complex lobe (e.g., Laaß, 2015). The most posterior portion of the endocast consists of the medulla oblongata and is delimited by the foramen magnum, framed by the supraoccipital dorsally and the basioccipital ventrally. The cast of the cranial nerves IX-XI is present on the ventral part of the hindbrain.

Bony labyrinth

The bony labyrinth houses the vestibular organ dorsally and the vestibule ventrally (Fig. 7). In GPIT-PV-60758, the left bony labyrinth is better preserved, with all three semicircular canals represented. Both vertical semicircular canals are elliptical and equally thick. In dorsal view, the circumference of the anterior semicircular canal (ascc) faces anteromedially, with the canal projecting laterally from the *crus communis* to form an angle of about 38° with the sagittal plane of the skull (Fig 7). The ascc encloses the largest area, with the floccular complex of the cerebellum protruding through it. The ascc presents an ampula anteriorly. This semicircular canal is enclosed by the prootic. The posterior semicircular canal (pscc) projects posterolaterally from the *crus communis* with an anteriorly opening angle of approximately 113° relative to the sagittal plane of the skull. The pscc is enclosed by the exoccipital medially and by the supraoccipital on its most lateral part. The *crus communis* is filled with dense sediment, making it hard to reconstruct. Only the most dorsal and most ventral parts of this structure are preserved. The horizontal semicircular canal (hscc) is subcircular, and its

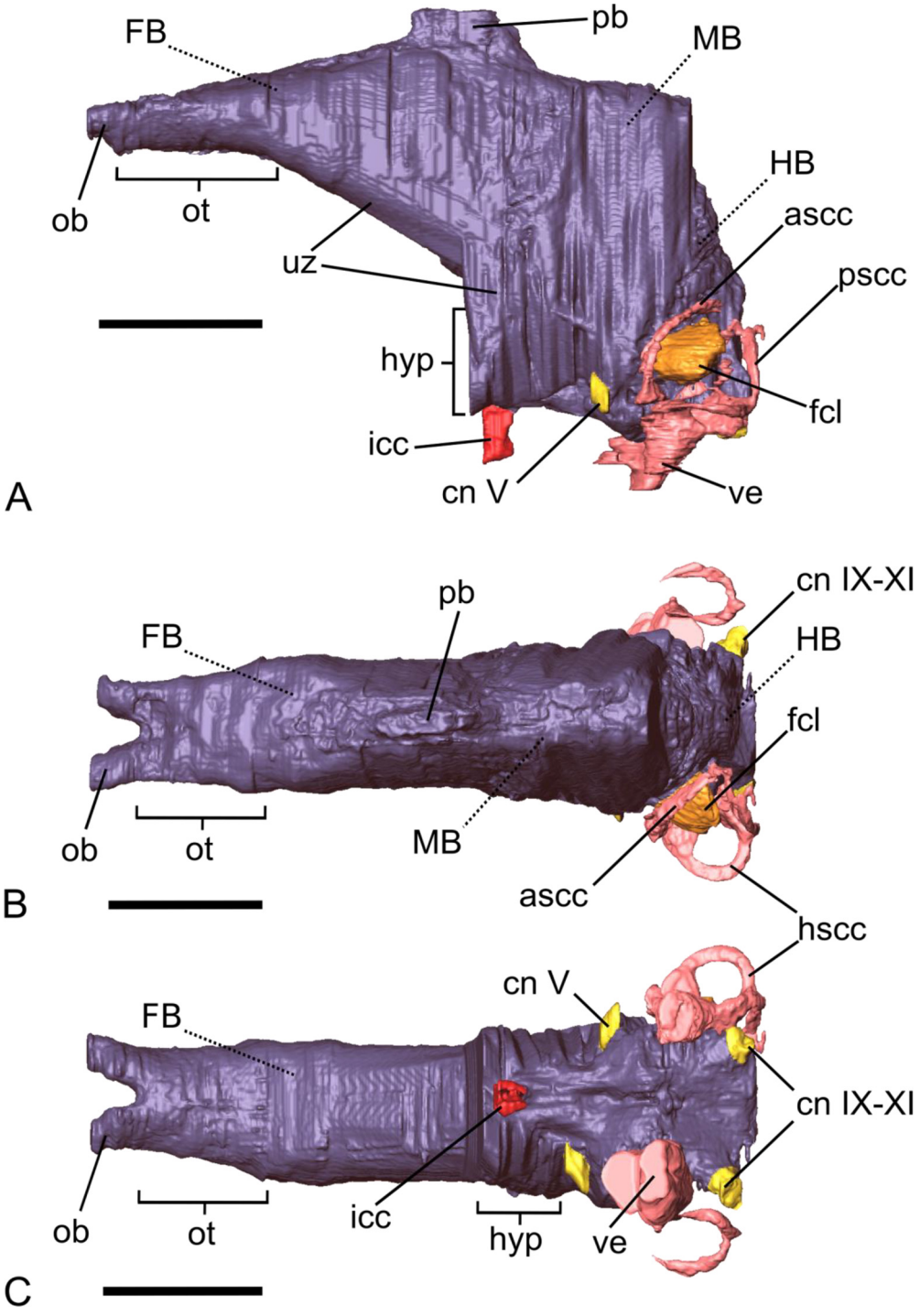

FIGURE 7. Braincase endocast and bony labyrinth. Lateral left (A), dorsal (B), and ventral (C) views. ascc - anterior semicircular canal; cn - cranial nerve(s); fcl - floccular complex lobe; hyp - hypophysis; horizontal semicircular canal; icc - internal carotid canal; ob - olfactory bulb; ot - olfactory tract; pb - pineal body; pscc - posterior semicircular canal; uz - unossified zone; ve - vestibule; FB - forebrain; HB - hindbrain; MB - midbrain. Scale bar = 10 mm.

posterior ampulla merges with the ampulla of the pscc, forming a ventral projection and concave internal surface between the latter and the vestibule. The anterior ampulla of the hscc is large and merges with the ampulla of the ascc,

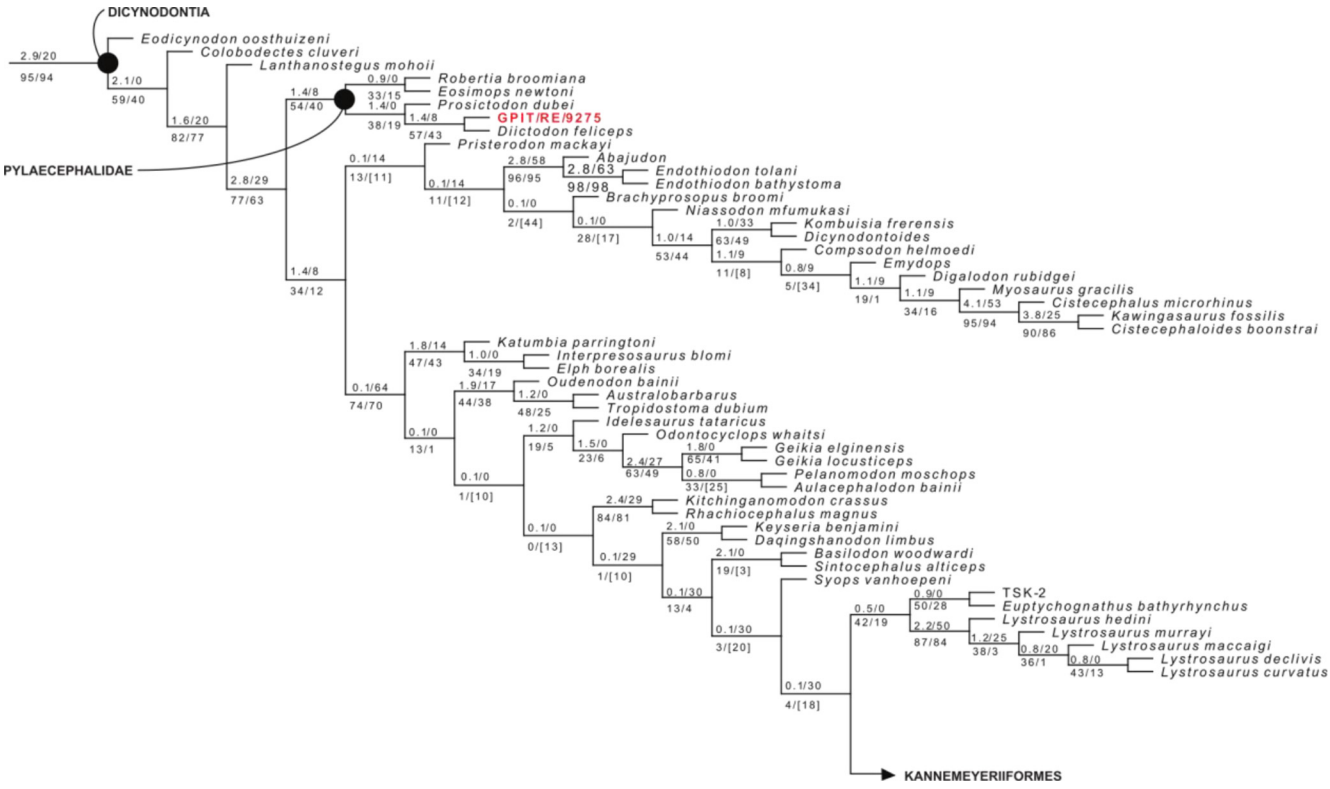

FIGURE 8. Region of interest of the most parsimonious cladogram from the phylogenetic analysis. Scores: 1135.549 steps, consistency index = 0.240, retention index = 0.718. Numbers at nodes represent Bremer supports (left/top), relative Bremer supports (right/top), symmetric resampling (left/bottom), and the percentage of suboptimal trees in which the node is resolved. GPIT-PV-60758 in red.

forming a wide surface in dorsal view (Fig. 7). The hscc is enclosed anteriorly by the prootic and posteriorly by the opisthotic. The sacculus and utriculus are not distinguishable in the vestibule. The vestibule projects ventrally with a slight anterior inclination. This structure has an elliptical cross-section with a mediolaterally oriented major axis. The lagena forms the ventral part of the cast of the bony labyrinth and is limited by the aperture of the fenestra ovalis on the tubera formed by the basioccipital and the parabasisphenoid.

Phylogenetic analysis

The phylogenetic analysis retained a single most parsimonious tree with a tree length of 1135.549 steps (Fig. 8; CI = 0.240; RI = 0.718), resulting from 5,892,799,471 rearrangements. GPIT-PV-60758 was recovered as the sister taxon of *Diictodon feliceps,* a moderately supported node (Bremer support = 1.379). The symmetric resampling value for the GPIT-PV-60758-*Di. Feliceps* node was 43. This relationship is supported by four discrete-state unambiguous synapomorphies: presence of a posterior median ridge on the palatal surface of the premaxilla without a flattened, expanded anterior area (5[2]); posterior process of the premaxilla with a non-bifurcated posterior tip (10[0]); presence of a distinct lateral caniniform buttress (29[1]); ventral edge of the caniniform process anterior to the anterior orbital margin (32[0]). The analysis places GPIT-PV-60758 and *D. feliceps* within the Pylaecephalidae, grouped with *Eosimops newtoni*, *Robertia broomiana*, and *Prosictodon dubei*. The symmetric resampling value corresponding to this node is 40. The Pylaecephalidae node is supported by the following diagnostic traits: presence of lateral anterior palatal ridges (3[1]); posterior process of the premaxilla with a bifurcated posterior tip (10[1]); caniniform depression with the form of a notch in the palatal rim anterior to caniniform process (28[2]); ventral edge of the caniniform process at the same level or slightly posterior to the anterior orbital margin (32[1]); presence of a tall, dorsally-convex cutting blade on medial edge of dorsal surface of dentary (126[1]); presence of a cleithrum (144[1]); procoracoid foramen or notch formed by the contributions of the procoracoid and scapula in lateral view (148[1]); presence

of an ectepicondylar foramen on the humerus (154[0]). GPIT-PV-60758 presents two character state reversals (10[1->0] and 32[1->0]) compared to the plesiomorphic condition in the Pylaecephalidae.

DISCUSSION

Phylogeny

The phylogenetic analysis allowed us to show that GPIT-PV-60758 falls within the Pylaecephalidae (Figs. 8 and S10). The specimen was retrieved as a sister taxon to *Di. feliceps*, which lends support to the referral of this specimen proposed by various authors including Brink (1986) or Kammerer et al. (2011, 2020). Our specimen showed four unambiguous synapomorphies, including two reversals that contrast with the emended diagnosis proposed here for the genus *Diictodon*. In addition, *Di. feliceps* presents an unambiguous synapomorphy (102[2]) that is not shared by GPIT-PV-60758. Nevertheless, we maintain the previous hypothesis that GPIT-PV-60758 should be considered as a *Di. feliceps*, and that the results from our phylogenetic analyses (including a relatively low resampling value) reflect intraspecific variation within *Di. feliceps*, previously studied by Sullivan & Reisz (2005). Perhaps, these results justify a more in depth revision of the genus *Diictodon*. Phylogenetic affinities within the Pylaecephalidae are the same as those in the trees recently published by Olroyd et al. (2017) and Kammerer et al. (2019).

Internal anatomy of the skull in GPIT-PV-60758

Our description provides the first digital reconstructions of the endocast and inner ear of *Diictodon*. Only a few dicynodonts have had their brain endocast anatomy reconstructed based on µ-CT scanning, including the endothiodontid *Niassodon mfumukasi* (Castanhinha et al., 2013), the eumantellid *Pristerodon mackayi* (Laaß, 2015), the cistecephalid *Kawingasaurus fossilis* (Laaß, 2014), and the basal bidentalian *Rastodon procurvidens* (Simão-Oliveira et al. 2019). GPIT-PV-60758 endocast presents the typical general shape known from other early therapsids, with a distinctive thin tubular forebrain and a more dorsoventrally and mediolaterally expanded mid- and hindbrain (see 'Anatomical description'). The olfactory tract in GPIT-PV-60758 is relatively shorter when compared to those in *N. mfumukasi*, *P. mackayi*, and *R. procurvidens*. It resembles the condition in *Dicynodon* (Lehman, 1961), which presents a short olfactory tract and dorsoventrally high mid- and hindbrains. As other dicynodonts, the GPIT-PV-60758 endocast falls in the description of the first stage of mammalian brain evolution and is comparable to that of nonmammalian cynodonts (Kemp, 2009). Kemp (2009) associates the development of the mid- and hindbrains to a development of movement coordination and proprioception. The large hindbrain presents a small lateral projection (flocculus) that protrudes through the anterior semicircular canal (Fig. 7). Although the flocculus is prominent in *N. mfumukasi* (Castanhinha et al., 2013) and *P. mackayi* (Laaß, 2015), this structure is much less pronounced in *R. procurvidens* (Simão-Oliveira et al., 2019), which is likely a result of the architecture of the braincase and a well-developed hindbrain in the former species (Walsh *et al.*, 2013; Ferreira-Cardoso et al., 2017). Similar to the remaining dicynodonts, the relatively small forebrain presents weakly developed olfactory bulbs, suggesting that olfaction was not as well-developed as seen in more recent cynodonts and modern mammals (Rowe et al., 2011). The short forebrain is directly related to the antero-posteriorly short ethmoid in GPIT-PV-60758 (Fig. 3).

Boonstra (1968) described the braincase of *Dicynodon* (considered as *Diictodon* by Simão-Oliveira et al., 2019). Our description matches the observations in Boonstra (1968), including the presence of a relatively shallow sella turcica that housed an equally small hypophysis (pituitary gland). Similar to other dicynodonts (Boonstra, 1968; Castanhinha et al., 2013; Laaß, 2015; Simão-Oliveira, 2019), the sella turcica structure was not delimited by a bony dorsum sella, given that the prootics do not meet at the midline to form the posterior wall of the hypophyseal fossa, such as in *Dimetrodon* (Romer & Price, 1940), dinocephalians (Boonstra, 1968), and gorgonopsians (Araújo et al., 2017). Instead, a blunt "dorsum sella" is present on the basioccipital, just posterior to the parabasisphenoid-basioccipital suture (Fig. 5D). Although the GPIT-PV-60758 "dorsum sella" is structurally analogous to that of other synapsids (limiting the hypophyseal fossa posteriorly), it has a distinct developmental origin, the basioccipital ossification center. This condition contrasts with that described in *Dicynodon*/*Diictodon* (Boonstra, 1968), in which the ventral part of the dorsum sella is formed by the parabasisphenoid.

The lack of long and prominent *pilae antoticae* delimiting the anterolateral part of the hypophysis in GPIT-PV-60758 contrasts with the condition usually found in other dicynodonts (Castanhinha et al., 2013; Laaß, 2015, Simão-Oliveira et al.,

2019). While Boonstra (1968) makes no reference to the pila antotica in *Dicynodon*/*Diictodon*, this structure only ossifies as a small anterior process of the prootic in *D. feliceps*, making its contribution to the lateral wall of the braincase extremely reduced (Sullivan & Reisz, 2005). In our specimen, a small triangular anterior process (putative part of the prootic) is indistinctly fused to the parabasisphenoid (Fig. 5). Such ossification on the parabasisphanoid is found, for instance, on the braincase of the cynodont *Diarthrognathus* (Olson, 1944; Presley & Steel, 1976).

The reconstruction of the internal anatomy of the GPIT-PV-60758 did not allow the identification of many relevant details concerning vascularization with the exception of the internal carotid canal (icc; Figs. 7). Similar to previous descriptions of *Diictodon* (Boonstra, 1968; Sullivan & Reisz, 2005) the internal carotid canal bifurcates ventrally. This condition resembles that in other dicynodonts such as *N. mfumukasi* (Castanhinha et al., 2013) and *P. mackayi* (Laaß, 2015). However, for most of its length, the internal dorsal canal in GPIT-PV-60758 consists of a single and relatively large cavity, similar to that in *R. procurvidens* (Simão-Oliveira et al., 2019). While Boonstra (1968) and Sullivan & Reisz (2005) described the internal carotid canals as enclosed by the parabasisphenoid, in GPIT/RE9275 their anterior part of margins consist of the pterygoid and the cultriform process (parasphenoid).

Internal anatomy of the mandible in GPIT-PV-60758

Most of the posterior elements of the mandible were badly preserved in GPIT-PV-60758 (see 'Anatomical description'). Nevertheless, the dentary was generally well preserved, including the dentary tables (Fig. 6). In *Diictodon*, these structures present a perforated surface (Sullivan & Reisz, 2005; Fig. 11E, Angielczyk & Rubidge, 2013). Vascular foramina are typically associated with the presence of a keratinous covering, not only in dicynodonts (e.g., Jasinoski & Chinsamy-Turan, 2012; Castanhinha et al., 2013), but also across a wide range of vertebrates such as ceratopsian dinosaurs (e.g., Bell et al., 2012), birds (Stidham, 1998), or mammals (Csorba et al., 2004). However, the perforations on the dentary table of *Diictodon* are relatively large in diameter. Despite the numerous scan artifacts and bad contrast in GPIT-PV-60758 internal mandibular structures, a close examination of the coronal slices of the specimen allowed us to identify these structures, as well as the corresponding canals (Fig. S8). Ferreira-Cardoso et al. (2019) associated similar structures (dorsal canaliculi) with vestigial tooth loci in some placental mammals such as anteaters, armadillos, or aardvarks. They discussed that the presence of dorsal canaliculi might be related to an exaptation of tooth nerve and vessel networks to innervate and vascularize keratinous structures (Ferreira-Cardoso et al., 2019). The presence of dorsal canaliculi in *Diictodon* and GPIT-PV-60758 suggest that vestigial tooth development might have occured in early ontogenetic stages (Ferreira-Cardoso et al., 2019 and reference therein). Further assessment of the internal mandibular anatomy of dicynodonts (including a three-dimensional reconstruction of a well preserved *Diictodon* specimen) is necessary to confirm this hypothesis.

CONCLUSION

Here we have used µ-CT scanning technology to re-describe a historical specimen from the South African Karoo (GPIT-PV-60758). In addition to a detailed description of its external morphology, we described for the first time the internal anatomy of GPIT-PV-60758, including the brain endocast and the left bony labyrinth. We also showed previously undescribed details such as the presence of dorsal canaliculi in the mandible, and the ossification of the anterior part of the braincase floor. Our phylogenetic analysis showed that GPIT-PV-60758 is, as noted by other authors, a *Diictodon feliceps* specimen. We hypothesize that autapomorphies recovered for GPIT-PV-60758 can be attributed to either ontogeny or to a stratigraphic variation within the genus *Diictodon*.

BIBLIOGRAPHY

Araújo, R., Fernandez, V., Polcyn, M. J., Fröbisch, J., & Martins, R. M. (2017). Aspects of gorgonopsian paleobiology and evolution: insights from the basicranium, occiput, osseous labyrinth, vasculature, and neuroanatomy. *PeerJ*, 5, e3119.

Araújo, R., Fernandez, V., Rabbitt, R. D., Ekdale, E. G., Antunes, M. T., Castanhinha, R., & Martins, R. M. (2018). *Endothiodon* cf. *Bathystoma* (Synapsida: Dicynodontia) bony labyrinth anatomy, variation and body mass estimates. *PLoS One*, 13(3), e0189883.

Angielczyk, K. D. & Rubidge, B. S. (2013). Skeletal morphology, phylogenetic relationships and stratigraphic range of Eosimops newtoni Broom, 1921, a pylaecephalid dicynodont (Therapsida, Anomodontia) from the Middle Permian of South Africa. *Journal of Systematic Palaeontology*, 11(2), 191–231.

Bell, P. R., Fanti, F., Currie, P. J., & Arbour, V. M. (2014). A mummified duck-billed dinosaur with a soft-tissue cock's comb. *Current Biology*, 24(1), 70-75.

Brink, A. S. (1986). Illustrated bibliographic catalogue of the Synapsida. Parts 1 and 2. Department of Mineral and Energy Affairs, Pretoria, Handbook 10, 540 pp.

Broom, R. (1911). On some new South African Permian reptiles. *Proceedings of the Zoological Society of London*, 1911: 1073–1082.

Broom, R. (1904). On a new species of *Oudenodon (O. megalorhinus)* from the Gough, S. Africa. *Records of the Albany Museum*, 1: 180–181.

Broom, R. (1913). On four new fossil reptiles from the Beaufort Series, South Africa. *Records of the Albany Museum*, 2, 397–401.

Csorba, G., Buzás, B., & Farkas, B. (2004). A previously undescribed skull of Steller's sea cow, *Hydrodamalis gigas* (Mammalia: Sirenia: Dugongidae) in the Hungarian Natural History Museum. In Annales historico-naturales Musei nationalis hungarici (Vol. 96, pp. 317–320). Hungarian Natural History Museum, Budapest.

Ferreira-Cardoso, S., Delsuc, F., & Hautier, L. (2019). Evolutionary tinkering of the mandibular canal linked to convergent regression of teeth in placental mammals. *Current Biology*, 29(3), 468–475.

Fröbisch, J. (2008). Global taxonomic diversity of anomodonts (Tetrapoda, Therapsida) and the terrestrial rock record across the Permian-Triassic boundary. *PLoS One*, 3(11), e3733.

Haughton, S. H. & Brink, A. S. (1954). A bibliographical list of Reptilia from the Karroo beds of Africa. *Palaeontologia Africana*, 2: 1–187.

Hoepen, E. C. N. van (1934). Oor die indeling van die Dicynodontidae na aanleiding van nuew vorme. *Paleontologiese Navorsing van die Nasionale Museum*, 2: 67–101.

Goloboff, P. A., Farris, J. S., & Nixon, K. C. (2008) TNT, a free program for phylogenetic analysis. *Cladistics*, 24: 774–786.

Jasinoski, S. C. & Chinsamy-Turan, A. (2012). Biological inferences of the cranial microstructure of the dicynodonts *Oudenodon* and *Lystrosaurus*. Forerunners of Mammals. *Radiation, Histology, Biology*, 148–176.

Jollie, M. T. (1960). The head skeleton of the lizard. *Acta Zoologica*, 41(1-2), 1-64.

Kammerer, C. F., Angielczyk, K. D., & Fröbisch, J. (2011). A comprehensive taxonomic revision of *Dicynodon* (Therapsida, Anomodontia) and its implications for dicynodont phylogeny, biogeography, and biostratigraphy. *Journal of Vertebrate Paleontology*, 31(sup1), 1-158.

Kammerer, C. F., Deutsch, M., Lungmus, J. K., & Angielczyk, K. D., (2020). Effects of taphonomic deformation on geometric morphometric analysis of fossils: a study using the dicynodont *Diictodon feliceps* (Therapsida, Anomodontia). *PeerJ*, 8, p.e9925.

King, G. M. (1988). Anomodontia. In P. Wellnhofer (Ed.), Handbuch der Paläoherpetologie, 17 C. Gustav Fischer Verlag, Stuttgart, 174 pp.

Novacek, M. J. (1993). Patterns of diversity in the mammalian skull. In J. Hanken & B. K. Hall (Eds.), The skull vol. 2 (pp. 438–545). University of Chicago Press.

Laaß, M. (2015). Virtual reconstruction and description of the cranial endocast of *Pristerodon mackayi* (Therapsida, Anomodontia). *Journal of morphology*, 276(9), 1089-1099.

LeBlanc, A. R., Brink, K. S., Whitney, M. R., Abdala, F., & Reisz, R. R. (2018). Dental ontogeny in extinct synapsids reveals a complex evolutionary history of the mammalian tooth attachment system. *Proceedings of the Royal Society B*, 285, 20181792.

Owen, R. (1845). Report on the Reptilian Fossils of South Africa. Part I. — Description of certain fossil crania, discovered by A. G. Bain, Esq., in sandstone rocks at the south-eastern extremity of Africa, referable to different species of an extinct genus of Reptilia (Dicynodon), and indicative of a new Tribe or Sub-order of Sauria. *Transactions of the Geological Society of London*, 2nd Series, 7, 59–84.

Paluh, D. J. & Sheil, C. A. (2013). Anatomy of the fully formed chondrocranium of *Emydura subglobosa* (Chelidae): a pleurodiran turtle. *Journal of Morphology*, 274(1), 1-10.

Presely, R. & Steel, F. L. (1976). On the homology of the alisphenoid. *Journal of Anatomy*, 121(Pt 3), 441.

Rieppel, O. (1993). Patterns of diversity in the reptilian skull. In *The Skull*, 2, 344-390.

Sidor, C. A., Hopson, J. A., & Keyser, A. W. (2004). A new burnetiamorph therapsid from the Teekloof Formation, Permian, of South Africa. *Journal of Vertebrate Paleontology*, 24(4), 938-950.

Stidham, T. A. (1998). A lower jaw from a Cretaceous parrot. *Nature*, 396(6706), 29–30.

Sulej, T. & Niedźwiedzki, G. (2019). An elephant-sized Late Triassic synapsid with erect limbs. *Science*, 363(6422), 78-80.

Toerien, M. J. (1953). The evolution of the palate in South African Anomodontia and its classificatory significance. *Palaeontologia Africana*, 1, 49–117.

Tschopp, E., Mateus, O., & Benson, R. B. (2015). A specimen-level phylogenetic analysis and taxonomic revision of Diplodocidae (Dinosauria, Sauropoda). *PeerJ*, 3, e857.

Whitney, M. R., Angielczyk, K. D., Peecook, B. R., & Sidor, C. A. (2021). The evolution of the synapsid tusk: insights from dicynodont therapsid tusk histology. *Proceedings of the Royal Society B*, 288(1961), 20211670.

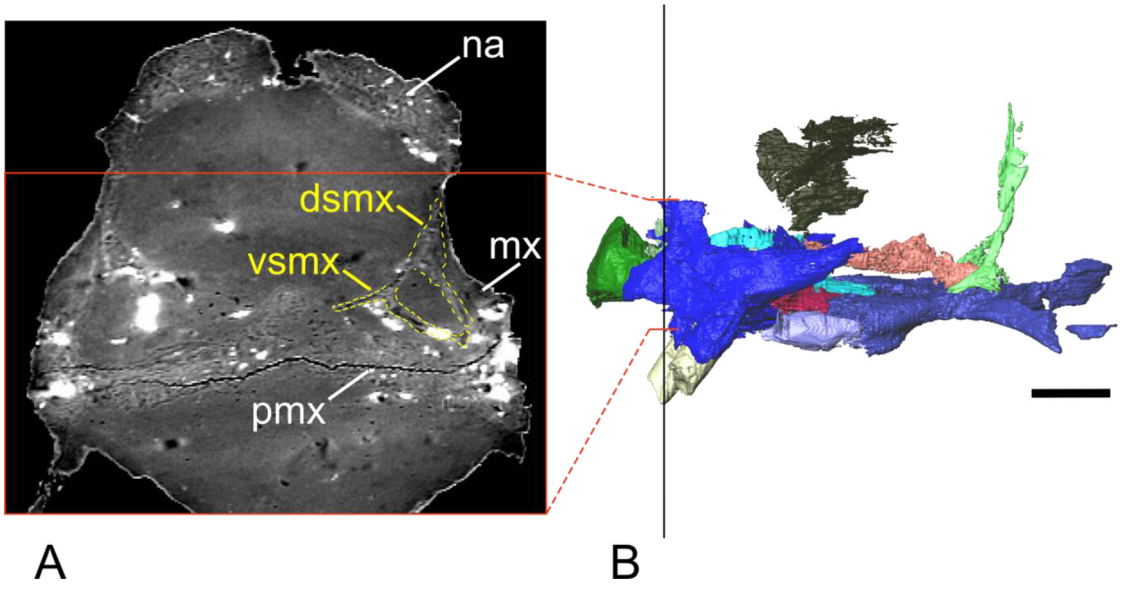

FIGURE S1. Cross-section of the septomaxilla. µCT scan coronal slice (A) and correspondent location (black line) shown on a lateral view of a 3D reconstruction (B). The orange rectangle and lines mark the region of interest. The septomaxilla is shown with a dashed yellow outline. dsmx - dorsal process of the septomaxilla; mx - maxilla; na - nasal; pmx - premaxilla. The cross-section is not to scale. Scale bar = 10 mm.

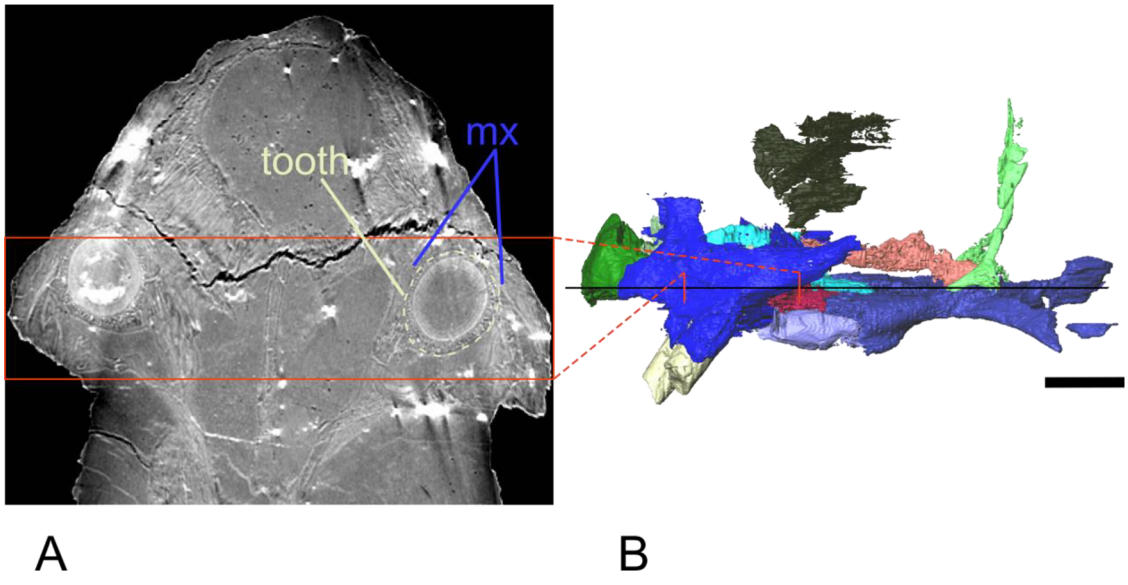

FIGURE S2. Transverse section of the tooth region. µCT scan transverse slice (A) and correspondent location (black line) shown on a lateral view of a 3D reconstruction (B). The orange rectangle and lines mark the region of interest. The tooth is shown with a dashed outline. mx - maxilla. The transverse section is not to scale. Scale bar = 10 mm.

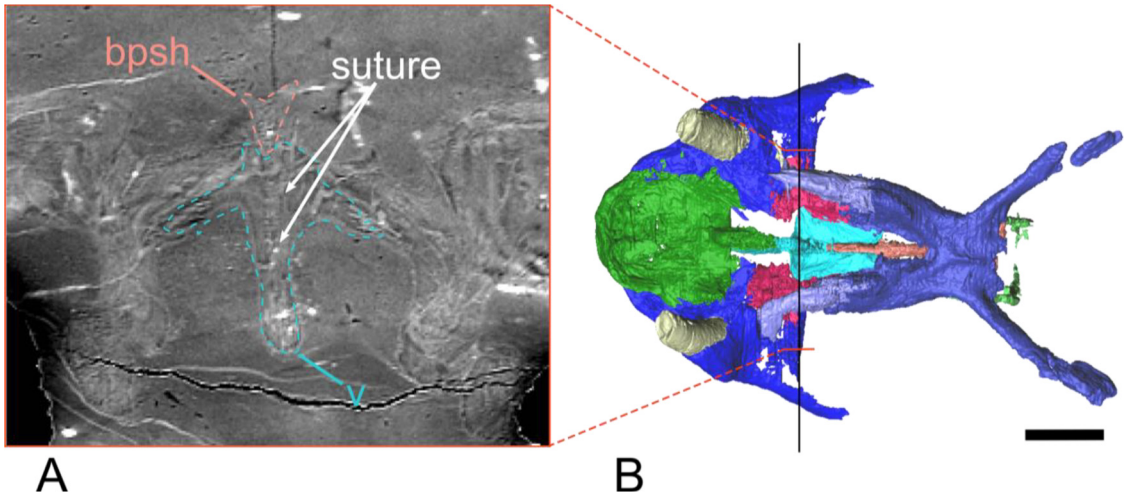

FIGURE S3. Cross-section of the vomer. µCT scan coronal slice (A) and correspondent location (black line) shown on a lateral view of a 3D reconstruction (B). The orange rectangle and lines mark the region of interest. The vomer and the cultriform process of the basiparasphenoid are shown with dashed cyan and coral outlines, respectively. The arrows point to the intervomerine suture. psh - cultriform process of the parabasisphenoid; v - vomer. The cross-section is not to scale. Scale bar = 10 mm.

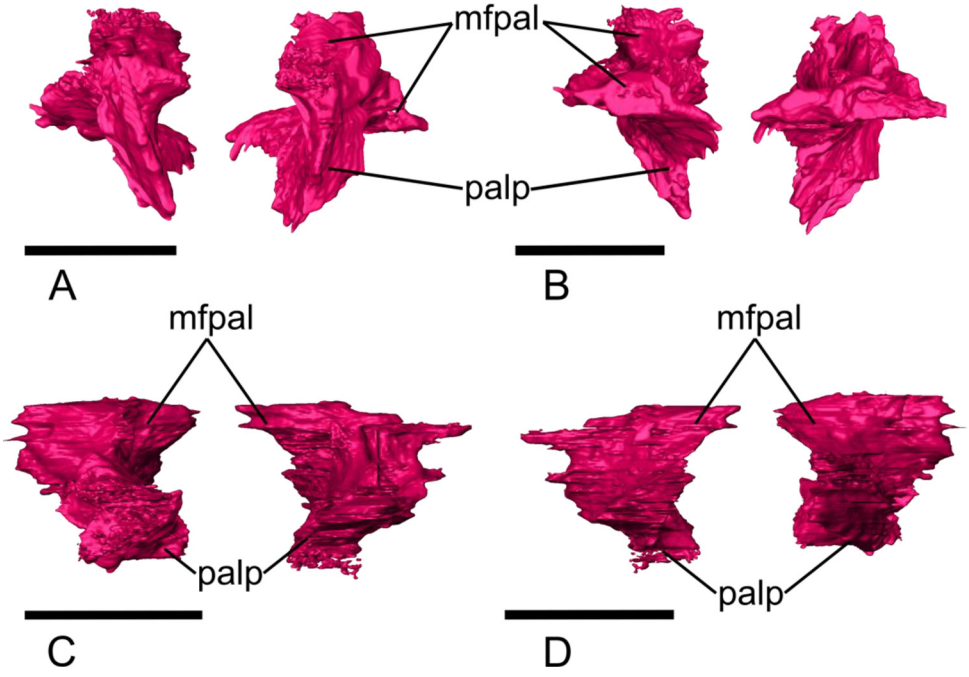

FIGURE S4. Palatine. Ventral (A), dorsal (B), anterior (C), and posterior (D) views. Mfpal - maxillary flanges of the palatine; palp - palatine pads. Scale bar = 10 mm.

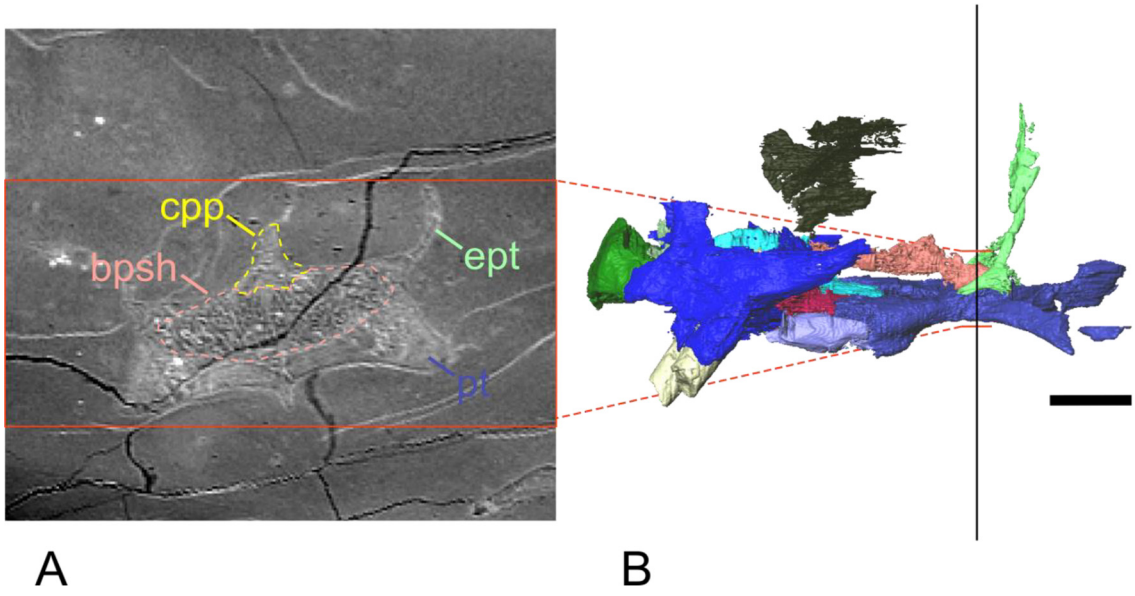

FIGURE S5. Cross-section of the basipresphenoid. µCT scan coronal slice (A) and correspondent location (black line) shown on a lateral view of a 3D reconstruction (B). The orange rectangle and lines mark the region of interest. The basipresphenoid and the cultriform process of the parasphenoid are shown with dashed coral and yellow outlines, respectively. bpsh - basipresphenoid; cpp - cultriform process of the parasphenoid; ept - epipterygoid; pt - pterygoid. The cross-section is not to scale. Scale bar = 10 mm.

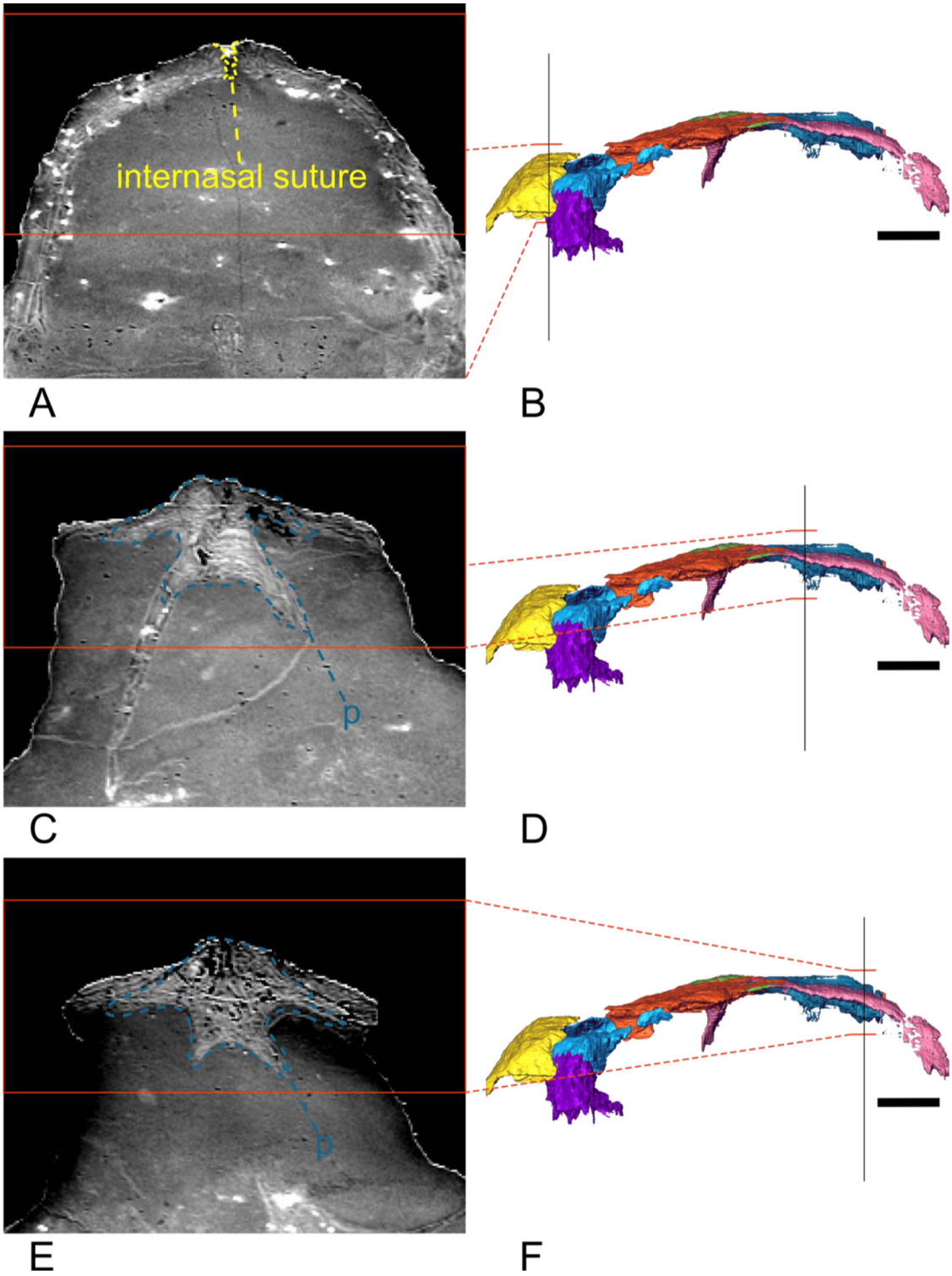

FIGURE S6. Cross-sections of the nasal and parietal. µCT scan coronal slice (A, C, E) and correspondent location (black line) shown on a lateral view of a 3D reconstruction (B, D, F). The orange rectangle and lines mark the region of interest. The internasal suture and the parietal are shown with dashed yellow and dark green outlines. p - parietal. The cross-sections are not to scale. Scale bar = 10 mm.

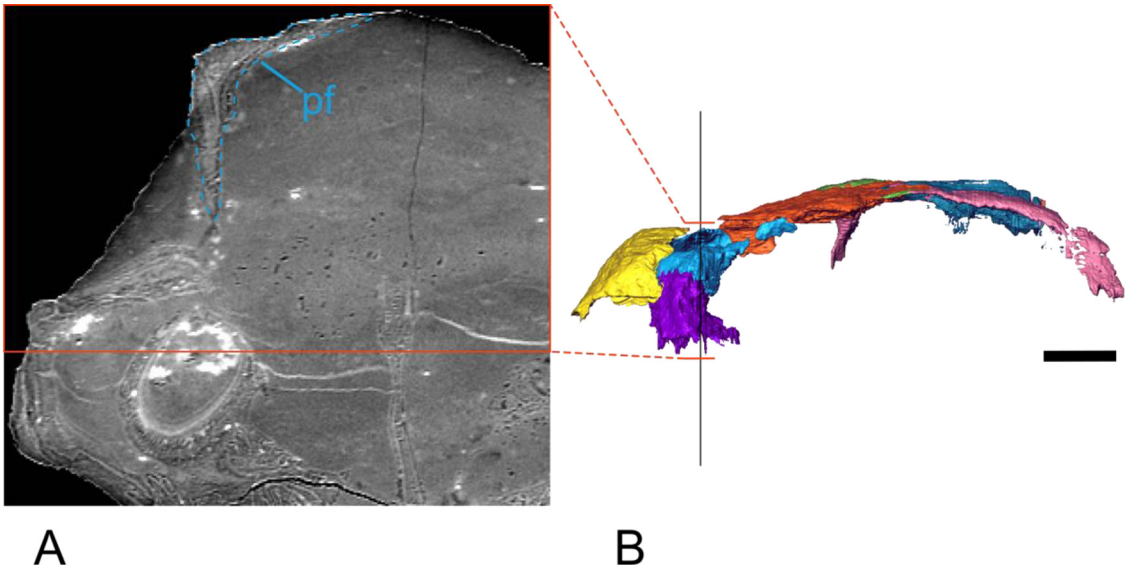

FIGURE S7. Cross-section of the prefrontal. µCT scan coronal slice (A) and correspondent location (black line) shown on a lateral view of a 3D reconstruction (B). The orange rectangle and lines mark the region of interest. The prefrontal is shown with a dashed blue outline. pf - prefrontal. The cross-section is not to scale. Scale bar = 10 mm.

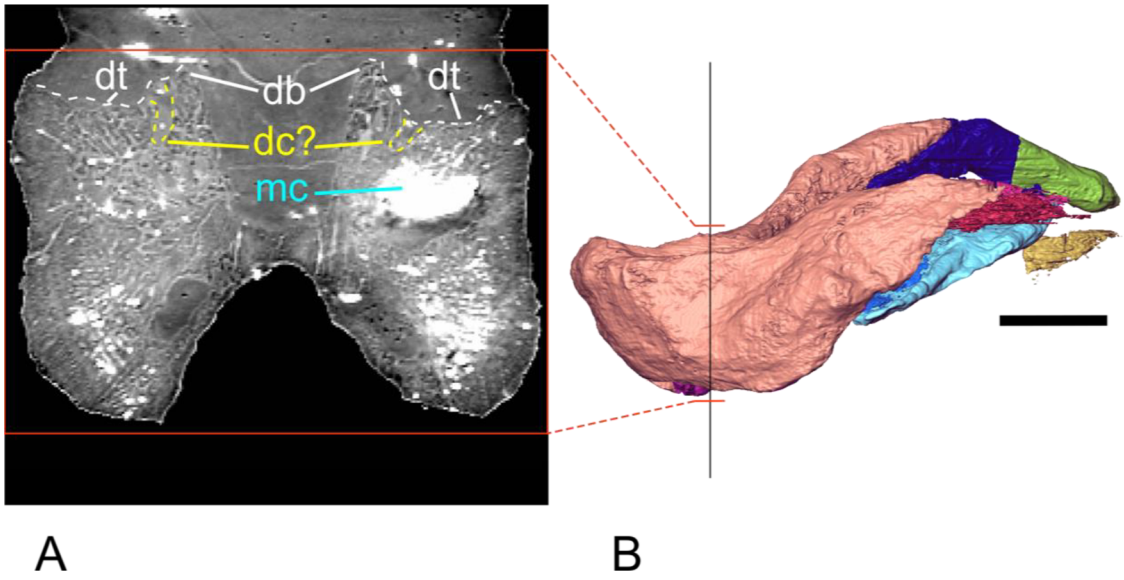

FIGURE S8. Cross-section of the dentary. µCT scan coronal slice (A) and correspondent location (black line) shown on a lateral view of a 3D reconstruction (B). The orange rectangle and lines mark the region of interest. Putative dorsal canaliculi and the dentary table are shown with dashed yellow and white outlines, respectively. db - dentary blade; dc - dorsal canaliculi; dt - dentary table; mc - mandibular canal. The cross-section is not to scale. Scale bar = 10 mm.

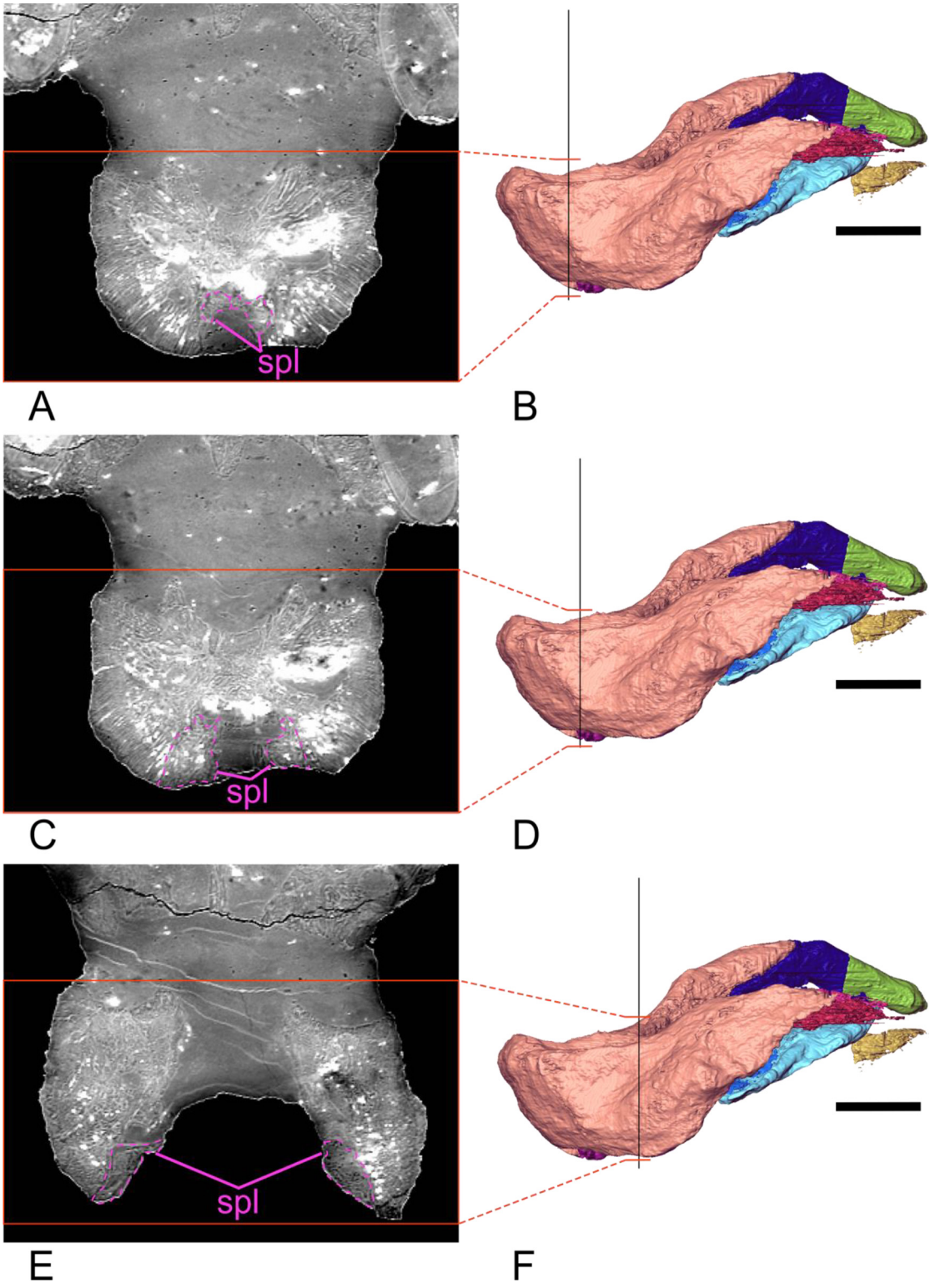

FIGURE S9. Cross-sections of the splenial. µCT scan coronal slice (A, C, E) and correspondent location (black line) shown on a lateral view of a 3D reconstruction (B, D, F). The orange rectangle and lines mark the region of interest. The splenial is shown with a dashed pink outline. spl - splenial. The cross-section is not to scale. Scale bar = 10 mm.